Quantitative Magnetic Particle Imaging

vorgelegt von
M. Sc.
Hendrik PAYSEN

an der Fakultät II – Mathematik und Naturwissenschaften
der Technischen Universität Berlin
zur Erlangung des akademischen Grades

Doktor der Naturwissenschaften
– Dr. rer. nat. –

genehmigte Dissertation

Promotionsausschuss:

Vorsitzender: Prof. Dr. Mario Dähne (TU Berlin)
Gutachter: Prof. Dr. Thomas Möller (TU Berlin)
Gutachter: Jun.-Prof. Dr. Silvio Dutz (TU Ilmenau)

Tag der wissenschaftlichen Aussprache: 30.06.2020

Berlin, 2020

Eidesstattliche Erklärung

Hiermit versichere ich, dass ich die vorliegende Arbeit selbstständig verfasst und keine anderen als die angegebenen Quellen und Hilfsmittel benutzt habe. Alle Ausführungen, die anderen veröffentlichten oder nicht veröffentlichten Schriften wörtlich oder sinngemäß entnommen wurden, habe ich kenntlich gemacht.

Die Arbeit hat in gleicher oder ähnlicher Fassung noch keiner anderen Prüfungsbehörde vorgelegen.

Signed:

_____

Date:

_____

Abstract

Magnetic particle imaging (MPI) is a noninvasive medical imaging technique introduced in 2005. MPI utilizes the unique properties of magnetic nanoparticles (MNP), which are of high interest for biomedical applications. One major advantage compared to other imaging modalities is that MPI images contain quantitative information about the MNP distribution. This information is beneficial for many applications for instance magnetic hyperthermia, drug delivery and cell tracking studies. But a detailed characterization of quantitative MPI, a comparison to other imaging techniques and the opportunities that it offers have not yet been reported.

In this thesis a comprehensive characterization of quantitative MPI was performed, employing the first commercial MPI scanner available. Imaging and quantification of MNP samples were achieved for iron masses above 16 ng with an accuracy of 8.8 %. The three strongest factors influencing the limit of detection and accuracy have been identified by investigating the MPI hardware, the data processing and the influence of the MNP environment. The first factor, affecting mainly the limit of detection, is the detection of systematic background signals generated by the MPI excitation fields. These background signals are partly attenuated and removed by using a gradiometric receive coil and by subtracting empty scanner measurements, but temporal variations of the background signals hamper a complete removal. Second, the quantification accuracy of MPI is strongly affected by large deviations of the reconstructed iron masses from the nominal values up to 1000 % caused by the variation of reconstruction parameters. A method was proposed and verified in phantom measurements, which eliminates these variations by calibrating the MPI intensities utilizing a reference measurement. The third dominant factor with strong influence on the quantification accuracy and the limit of detection is the MNP environment. Typical biomedical environments, for instance MNPs interacting with monocytic cells, show deviations from the nominal iron amount of more than 100 %. Correction of these deviations were achieved using a technique, called multi-color MPI, resulting in an improved quantification accuracy of 12 %.

The MPI results were compared to measurements performed with magnetic resonance imaging (MRI) and showed a lower limit of detection (factor of 5) and a higher accuracy (factor of 2) for MNP samples in realistic biological environments. However, MRI provides a larger field of view, a higher spatial resolution and the simultaneous acquisition of anatomical information in the images.

The strength of quantitative MPI was utilized in an in-vitro experiment, demonstrating that MPI can image and quantify the cellular uptake of MNPs into living cells by analyzing changes of their dynamic magnetic behavior with a temporal resolution of seconds. This technique provides information about the uptake dynamics, which is especially interesting since the uptake behavior is correlated with pathological changes and might open the opportunity for an early diagnostics of inflammatory diseases.

The achievements of this thesis form a foundation for further developments of MPI technology and the translation into clinical applications.

Zusammenfassung

Magnetic particle imaging (MPI) ist eine nicht-invasive, medizinische Bildgebungsmodalität, die im Jahr 2005 erstmals vorgestellt wurde. Diese Technik basiert auf den physikalischen Eigenschaften magnetischer Nanopartikel (MNP), welche für zahlreiche biomedizinische Anwendungen interessant sind. Ein großer Vorteil von MPI verglichen mit anderen Bildgebungsmethoden ist, dass quantitative Informationen über die Partikelverteilung in den Bildern enthalten sind. Diese Informationen werden in mehreren Bereichen wie zum Beispiel in der magnetischen Hyperthermie oder in der Verfolgung von Medikamenten und Zellen benötigt. Aber eine detaillierte Charakterisierung der quantitativen MPI Parameter, ein Vergleich mit anderen Bildgebungsmethoden und eine Untersuchung, welche Anwendungsmöglichkeiten quantitatives MPI bietet, wurden bisher noch nicht durchgeführt.

Diese Dissertation beinhaltet eine detaillierte Charakterisierung von quantitativem MPI. Die präsentierten Messungen wurden unter Verwendung des ersten kommerziell erwerbbaren MPI Systems durchgeführt. Die Bildgebung und Quantifizierung von MNP Proben mittels MPI wurde erfolgreich nachgewiesen für Eisenmassen größer als 16 ng mit einer Quantifizierungsgenauigkeit von 8.8 %. Die drei Faktoren mit dem stärkstem Einfluss auf das Detektionslimit und die Quantifizierungsgenauigkeit wurden identifiziert, indem die MPI Hardware, die Datenverarbeitung und der Einfluss der Umgebung der MNP untersucht wurden. Der erste Faktor, der hauptsächlich das Detektionslimit beeinflusst, sind detektierte Hintergrundsignale, verursacht durch die MPI Anregungsfelder. Diese Signale können teilweise durch die Verwendung einer speziellen Empfangsspule in Gradiometer-Anordnung und durch die Subtraktion von Leermessungen entfernt werden. Zeitliche Variationen der Hintergrundsignale verhindern allerdings eine komplette Korrektur. Der zweite Faktor ist bedingt durch die MPI Bildrekonstruktion und betrifft vor allem die Quantifizierungsgenauigkeit. Eine Modifikation der Rekonstruktionsparameter führt zu rekonstruierten Eisenmassen mit Abweichungen von bis zu 1000 % verglichen mit den nominellen Werten. Eine Methode, die diese Abweichungen basierend auf einer Kalibrations-Messung eliminiert, wurde vorgestellt und in Phantommessungen verifiziert. Der dritte Faktor, mit starkem Einfluss auf das Detektionslimit und die Quantifizierungsgenauigkeit, ist der Einfluss der MNP Umgebung. Typische biomedizinische Umgebungen, z.B. MNP in Kontakt mit lebendigen Zellen, führen zu Änderungen der quantifizierten Werte von mehr als 100 %. Eine Korrektur dieser Abweichungen wurde mithilfe der Technik namens „multi-color MPI“ erreicht und verbesserte die Quantifizierungsgenauigkeit auf 12 %.

Die MPI Ergebnisse wurden verglichen mit Magnetresonanztomographie-Messungen und zeigten ein geringeres Detektionslimit (Faktor 5) und eine höhere Quantifizierungsgenauigkeit (Faktor 2) für MNP Proben in Medien mit realistischen Relaxationszeiten. Allerdings bietet MRI auch Vorteile gegenüber MPI, wie z.B. ein größeres Sichtfeld, eine höhere Ortsauflösung und die zeitgleiche Aufnahme von anatomischen Informationen in den Bildern.

Die Stärken vom quantitativen MPI wurden in einem in-vitro Experiment genutzt, um die Aufnahme von MNP in Zellen mit hoher zeitlicher Auflösung abzubilden und zu quantifizieren. Dafür

wurden die Änderungen der dynamisch magnetischen Eigenschaften der Partikel während der zellulären Aufnahme verwendet. Diese Technik ermöglicht es Informationen über die dynamische Zellaufnahme zu erhalten, welche von großem Interesse sind, da das Aufnahmeverhalten mit pathologischen Veränderungen auf zellulärer Ebene korreliert ist. Daher bietet diese Technik die Chance für eine frühzeitige Diagnose von Entzündungs-Krankheiten.

Die Ergebnisse dieser Arbeit bilden die Basis für weitergehende Entwicklungen der MPI Technologie und mögliche klinische Anwendungen.

Danksagung

An dieser Stelle möchte ich mich bei allen Personen bedanken, die mich im Zuge dieser Arbeit auf unterschiedliche Weise unterstützt haben.
Zuerst gebührt mein Dank Herrn Prof. Dr. Thomas Möller für die Betreuung, das entgegengebrachte Vertrauen und die hilfreichen Kommentare im Zuge der Fertigstellung dieser Dissertation. Mein Dank gilt ebenfalls Prof. Dr. Tobias Schäffter, Prof. Dr. Silvio Dutz und Prof. Dr. Mario Dähne, für die Ermöglichung und die konstruktive Kritik bei der Erstellung dieser Arbeit.
Ein besonderer Dank gilt Dr. Frank Wiekhorst für die fachliche Betreuung und die uneingeschränkte Hilfe in allen Bereichen mit Bezug auf die Arbeit und darüber hinaus. Dr. Olaf Kosch danke ich für die Einarbeitung ins Themenfeld MPI sowie für die volle Unterstützung bei all meinen Fragen. Ferner möchte ich mich bei Patricia Radon für zahlreiche angenehme Gespräche und ein stets offenes Ohr für all meine Probleme bedanken. Dr. James Wells, Dr. Maik Liebl, Dr. Norbert Löwa, Dr. Uwe Steinhoff, Dr. Dietmar Eberbeck und dem Rest der Arbeitsgruppe 8.23 der PTB danke ich für die schöne Mischung aus lockerer Arbeitsatmosphäre und spannenden wissenschaftlichen Diskussionen. Die Mitarbeit in dieser Arbeitsgruppe ermöglichte mir das Kennenlernen vieler internationaler Gruppen, wobei ich insbesondere der Gruppe von Dr. Antje Ludwig aus der Charité Berlin und der Gruppe von Jochen Franke bei Bruker Biospin für die Zusammenarbeit danken möchte.
Zum Schluss möchte ich mich bei meiner gesamten Familie und vor allem meiner Freundin bedanken, die mich während der kompletten Arbeit begleitet und bedingungslos unterstützt haben.

Contents

Eidesstattliche Erklärung iii

Abstract v

Zusammenfassung vii

Danksagung ix

Contents xi

List of Figures xv

List of Abbreviations xvii

List of Symbols xix

1 Introduction 1

2 Theoretical basics 5

2.1 Magnetic Nanoparticles . . . 5

2.2 Magnetic Particle Imaging . . . 6

2.2.1 Signal Generation . . . 7

2.2.2 Spatial Encoding . . . 8

2.2.3 Image reconstruction . . . 10

2.3 Magnetic Resonance Imaging . . . 12

2.3.1 Nuclear magnetic resonance . . . 12

2.3.2 Spatial encoding and image reconstruction . . . 14

2.3.3 Influence of MNPs . . . 14

2.4 Characterization of a quantitative measurement technique . . . 15

2.4.1 Linearity . . . 15

2.4.2 Limit of detection . . . 16

2.4.3 Accuracy . . . 16

3 Experimental setup **17**
3.1 Magnetic particle imaging system . . . 17
3.1.1 Basic experimental setup . . . 17
3.1.2 System specifications . . . 18
3.1.3 MPI receive hardware . . . 19
3.2 Magnetic particle spectrometer (MPS) . . . 21
3.3 Nuclear magnetic resonance (NMR) system . . . 22
3.4 Magnetic resonance imaging (MRI) system . . . 23
3.5 Magnetic nanoparticle (MNP) types . . . 23
3.5.1 Ferucarbotran . . . 24
3.5.2 Synomag . . . 24

4 MPI hardware and noise characterization **25**
4.1 Hardware characterization . . . 25
4.1.1 Transmit hardware . . . 26
4.1.2 Receive hardware . . . 28
4.2 MPI noise characterization . . . 31
4.2.1 Random noise . . . 32
4.2.2 Background signals . . . 34
4.2.3 Signal stability analysis . . . 36
4.2.4 Transient signals . . . 42
4.3 MPI hardware and noise: Summary and discussion . . . 44

5 MPI raw signal characterization **47**
5.1 MPI raw signal calibration . . . 47
5.2 1D-MPI quantification . . . 48
5.3 System function analysis . . . 50
5.4 MPI raw signal characterization: Summary and discussion . . . 53

6 Quantitative imaging **55**
6.1 Influence of reconstruction parameters . . . 55
6.1.1 Frequency component selection . . . 56
6.1.2 Regularization . . . 58
6.1.3 Number of Iterations . . . 60
6.1.4 Reconstruction parameter choice . . . 61
6.2 Characteristics of MPI quantification . . . 62
6.2.1 Total iron mass . . . 63
6.2.2 Iron concentration . . . 65
6.3 MNP quantification using magnetic resonance imaging . . . 67
6.3.1 MNPs in pure water . . . 68

6.3.2 MNPs in copper sulfate solution . . . 71
6.4 Quantitative Imaging: Summary and discussion . . . 73

7 MPI quantification in a biological environment **77**
7.1 Cellular MPI . . . 77
7.2 In-vitro quantification of cellular uptake . . . 81
7.2.1 Light microscopy . . . 81
7.2.2 Colorimetric iron determination . . . 82
7.2.3 In-vitro MPS . . . 84
7.2.4 In-vitro MPI . . . 86
7.3 Multi-color MPI: Summary and discussion . . . 88

8 Summary and Conclusions **91**

A MPI parameter **94**

Bibliography **98**

List of Figures

1.1 Factors influencing quantitative imaging 2

2.1 Illustration of a single MNP and Langevin magnetization of a MNP ensemble 6
2.2 Basic principle of MPI signal generation 7
2.3 Selection field used for spatial encoding in MPI and Lissajous trajectory of the field-free point 8
2.4 Basic principle of spatial encoding in MPI 9
2.5 Visualization of an ensemble of magnetic moments of hydrogen nuclei 13
2.6 Visualization of longitudinal and transverse relaxation of the magnetization in MRI . 14
2.7 Visualization of Trueness and precision 16

3.1 Schematic sequence of operation during a conventional MPI measurement 17
3.2 Basic setup of the used MPI system 18
3.3 Photographs of the MPI scanner 19
3.4 Schematic transmit-receive chains and model of the separated receive coil designed for MPI 20
3.5 Visualization of the transmit-receive and separate-receive MPI coils 21
3.6 Photographs MPS, NMR and MRI systems 23

4.1 Relative deviation of drive field amplitudes as a function of time 26
4.2 Characterization of gradient fields 27
4.3 Frequency-dependent transfer functions of each MPI receive coil 28
4.4 Spatial sensitivity profiles of the x-TxRx and x-Rx-coil 30
4.5 Comparison of measurements and simulations of the spatial sensitivity profiles of the x-TxRx and x-Rx-coil 31
4.6 Empty MPI raw signal amplitude spectrum 33
4.7 Influence of averaging on random MPI noise 34
4.8 Qualitative influence of hardware components on the MPI raw signal 35
4.9 Quantitative influence of hardware components on the MPI raw signal 36
4.10 Background signal variations as a function of time (minutes) 37
4.11 Background signal variations as a function of time (hours) 38
4.12 Background signal variations as a function of time (months) 40

4.13 Background corrected spectra of the empty scanner . . . 41
4.14 Distortions in MPI raw signals . . . 42
4.15 MPI raw signal distortions: probability distribution . . . 43

5.1 Comparison of MPS and 1D MPI . . . 48
5.2 3D-MPI amplitude spectrum . . . 50
5.3 Spatial dependence of the MPI raw signal for a single frequency component . . . 51
5.4 Spatial dependence of the MPI raw signal for multiple frequency components . . . 52
5.5 Signal to noise ratio determined from a SF acquisition . . . 53

6.1 PCR sample filled with 1 µL Ferucarbotran diluted in water . . . 56
6.2 Reconstructions with varying number of frequency components . . . 57
6.3 Quantitative influence of the number of frequency components on the quantified iron mass . . . 58
6.4 Reconstructions with varying regularization parameter . . . 59
6.5 Quantitative influence of the regularization parameter on the quantified iron mass . . . 59
6.6 Reconstructions with varying number of iterations . . . 60
6.7 Quantitative influence of the number of iterations on the quantified iron mass . . . 61
6.8 Reconstructed MPI images of dot-phantoms with varying iron content . . . 64
6.9 Quantified iron masses extracted from reconstructed MPI images . . . 65
6.10 PCR sample filled with 160 µL Ferucarbotran diluted in water . . . 66
6.11 Reconstructed MPI images for the determination of the limit of detection . . . 66
6.12 Quantified iron masses extracted from reconstructed MPI images . . . 67
6.13 MRI amplitude images of MNP samples diluted with pure water . . . 69
6.14 Iron concentration of MNP samples quantified using MRI and NMR . . . 70
6.15 MPI and MRI images of MNP samples diluted with copper sulfate solution . . . 72
6.16 Quantification of MNP samples diluted with copper sulfate using MPI, MRI and NMR 73

7.1 MPI reconstructions of free and cell samples using different SFs . . . 79
7.2 Deviation of MPI quantification to nominal iron content using different SFs . . . 80
7.3 Light microscopy THP-1 cells with Synomag . . . 82
7.4 Quantification of cellular uptake determined by the phenanthroline-based iron assay method . . . 83
7.5 Schematic diagram of the in-vitro MPS and MPI measurements . . . 84
7.6 In-vitro MPS results measuring the cellular uptake of Synomag in THP-1 cells . . . 85
7.7 MPI images of free and cell bound MNPs during cellular uptake . . . 87
7.8 MPI quantification of cellular uptake over time . . . 88

List of Abbreviations

A/D	Analogue-to-digital converter
BG	Background
BPF	Band-pass-filter
BSF	Band-stop-filter
CPMG	Carr-Purcell-Meiboom-Gill (MRI pulse sequence)
CT	Computed Tomography
D/A	Digital-to-analogue converter
FOV	Field of view
LNA	Low-noise amplifier
MNP	Magnetic nanoparticles
MPI	Magnetic particle imaging
MPS	Magnetic particle spectroscopy
MRI	Magnetic resonance imaging
NMR	Nuclear magnetic resonance
PA	Power amplifier
PBS	Phosphate-buffered saline
ROI	Region of interest
Rx	Receive-only
SF	System function
SNR	Signal to noise ratio
Std	Standard deviation
TxRx	Transmit-receive

List of Symbols

Symbol	Name
$\mathbf{B}$	Magnetic flux density
c_{Fe}	Iron concentration
d_{c}	Core diameter
d_{h}	Hydrodynamic diameter
f	Frequency
ϕ	MPI raw signal calibration factor
φ	Phase of the complex Fourier transformed MPI raw signal
$\mathbf{G}$	Magnetic gradient vector
$\mathbf{H}$	Magnetic field strength
I	MPI image signal intensity
γ	Gyromagnetic ratio
λ	Regularization parameter
m_{Fe}	Iron mass
M	M-parameter for transient signal detection
$\mathbf{M}$	Magnetization vector
M_0	Saturation magnetization
MAD	Median absolute deviation
MED	Median
n_{mo}	Mixing order
N_{FC}	Number of frequency components used in MPI reconstruction
N_{it}	Number of iterations used in MPI reconstruction
p_{d}	Probability for the detection of a transient signal
$\mathbf{r}$	Spatial position
r	Linearity response index
r_1	Longitudinal relaxivity
r_2	Transverse relaxivity
R	Coil radius
R_1	Longitudinal relaxation rate
R_2	Transverse relaxation rate
ρ	Transfer function

s	Standard deviation
$\mathbf{S}$	MPI system function
T_1	Longitudinal relaxation time
T_2	Transverse relaxation time
TE	Echo time (MRI pulse sequence parameter)
TR	Repetition time (MRI pulse sequence parameter)
τ	Time gap between two MPI measurements
u	MPI raw signal
u_{bias}	Bias of a measurement
u_{c}	Combined standard uncertainty
$\hat{u}$	Fourier-transformed MPI raw signal
$\overline{u}_{\text{MPI}}$	Mean MPI signal amplitude
ω_{L}	Larmor frequency

Chapter 1

Introduction

Accurate and reliable medical imaging is of utmost importance in modern clinical routine. The development and improvement of existing and novel imaging modalities is a central aspect of biomedical research with the goal for a more reliable and accurate disease diagnostics, staging and therapy. State of the art radiology is firmly based on a qualitative image analysis. Although the information gained from this concept is very valuable, it is strongly influenced by the imaging hardware and human perception [1–3]. Recent years have shown a constantly growing interest in extracting quantifiable parameters from medical images. These quantitative parameters can be correlated with certain disease states, allowing a more reliable, accurate and objective diagnosis [4]. Additionally, quantitative data simplify intra- and inter-site comparisons, long-term studies and automated image analyzes [5, 6]. Multiple modalities are capable of determining quantitative features from imaging data including magnetic resonance imaging (MRI) [7, 8], x-ray imaging [9], computed tomography (CT) [10], ultrasound imaging [11], positron-emission tomography [12] and single-photon emission computed tomography [13].

In 2005, a new imaging technique called magnetic particle imaging (MPI) has been presented [14]. This technique relies on the unique properties of magnetic nanoparticles (MNPs). MNPs have attracted great attention in modern nanomedicine and so far have been proposed to be used for vascular mapping [15], perfusion imaging [16], hyperthermia treatments [17, 18], drug delivery [19] and cell tracking [20]. Many of these applications require or highly benefit from the quantitative knowledge of the spatial distribution of MNPs within the patient. For instance, this information allows more reliable, faster and safer planning of hyperthermia treatments, minimizing possible damage to healthy tissue [21]. Drug delivery studies require the quantitative information to monitor and improve the specificity of new drugs [22, 23]. The same applies to cell-tracking experiments, in which MNP-labeled cells are measured over several weeks or months [24, 25].

MPI determines the spatial distribution of MNPs non-invasively without using ionizing radiation. Since the first publication about MPI, multiple working groups started research to improve MPI technology worldwide. Nowadays, two companies (Bruker BioSpin and Magnetic Insight) sell preclinical MPI systems and the advantages of MPI compared to other imaging techniques have been demonstrated in several published preclinical studies and phantom experiments [26–31]. Even the first human-sized scanner concepts have been presented in the last years [32, 33]. Despite big improvements

over the last decades, remaining issues, for instance peripheral nerve stimulation, approval of clinical use of MNPs and sensitivity, need to be resolved before MPI can be translated in clinical routine, which requires a detailed understanding of the underlying physical details of MPI technology [34].

MPI utilizes the nonlinear magnetic susceptibility of MNPs in combination with magnetic excitation fields to obtain a spatially encoded signal, from which the MNP distribution is reconstructed. Three-dimensional images are generated with a high temporal resolution of up to 21 ms and spatial resolutions up to the sub-millimeter range [15, 35, 36]. MPI allows to detect tiny MNP amounts in the nanogram regime and the sensitivity is constantly improved by advanced hardware components, software developments and MNP properties [31, 37–39]. A major advantage compared to other imaging techniques is that the signal is only generated by MNPs and no signal attenuation is caused by surrounding tissue, allowing imaging with high contrast and specificity [40]. MPI enables imaging of MNPs interacting with substances on a cellular or sub-cellular level, which can be utilized to gain new insights about fundamental biological processes [25]. Since the MPI imaging signal is directly correlated to the amount of MNPs, it is commonly described as a quantitative imaging modality. However, little detailed investigations have been made on either quantitative MPI or the opportunities which it offers.

The term "quantitative MPI" is used in this thesis to describe the possibility of extracting quantitative information about the MNP amount from MPI measurement data. For a detailed quantitative analysis of MPI images, multiple factors need to be taken into account. Figure 1.1 displays an overview of some factors, grouped in the categories concerning hardware, data processing and the MNP environment.

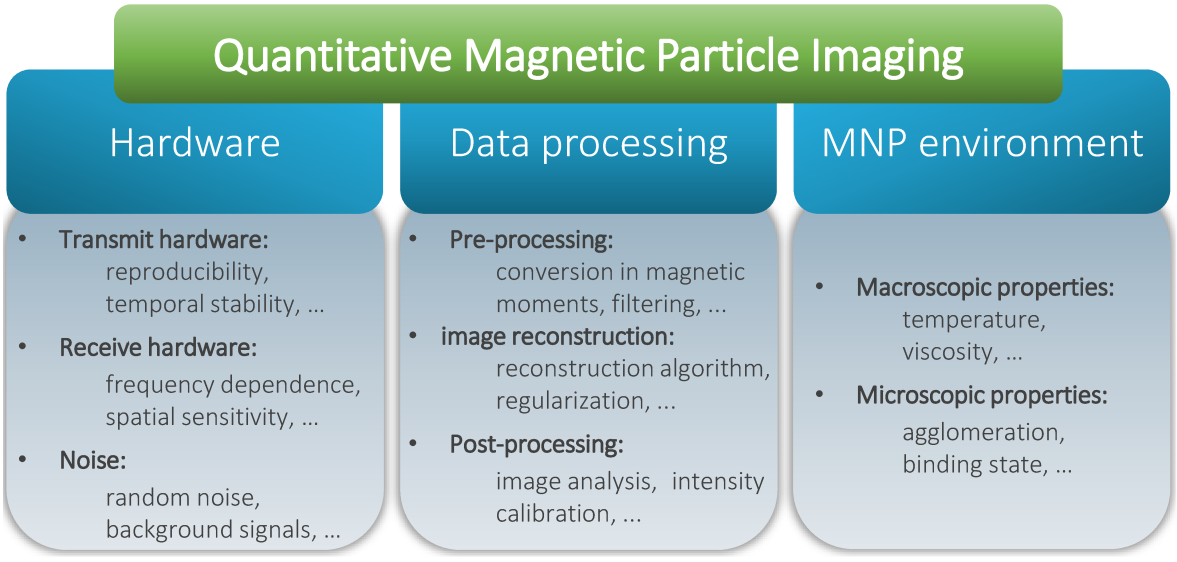

FIGURE 1.1: Factors influencing quantitative MPI grouped in the categories hardware, data processing and MNP environment, which are analyzed separately in this thesis.

The MPI-relevant hardware elements are categorized in transmit hardware, used to generate the magnetic fields needed to excite the MPI raw signals, and receive hardware, used to acquire the MPI raw signals. These acquired signals are disturbed by random noise and systematic background signals particularly caused by the excitation fields itself [41]. MPI hardware components have been constantly advanced over the last decades to offer improved temporal stability, background signal attenuation and sensitivity with the aim for enhanced image quality [38, 42, 43]. The qualitative influence of noise and background signals on MPI images has often been described in published literature, but the influence of these factors on quantitative MPI has not been reported so far.

Once the MPI raw signals are acquired, they are processed to obtain the MPI image. This can include pre-processing steps, before image reconstruction, like filtering of distorted signal components or correction of the frequency-dependent influence of receive hardware components [44]. Since no exact mathematical formulation for the image reconstruction has been presented so far, MPI images are mostly reconstructed by solving an inverse problem [45, 46]. The solutions acquired from this procedure represent an approximation of the true values and vary depending on the chosen reconstruction parameters. The algorithms used for the MPI image reconstruction are still topic of ongoing research [47–57]. So far, the main focus of this research is to improve the image quality and not much information about the quantitative influence of varying reconstruction parameters has been presented.

MPI aims for clinical applications, in which MNPs are introduced into the human body. As a consequence, the environmental conditions, including macroscopic parameters (temperature, viscosity, etc.) and microscopic parameters (binding state, agglomeration, etc.), around the MNPs change, which affects their dynamic magnetic behavior and hence the MPI signal generation. The effects of the MNP environment on the magnetic behavior of MNPs have been intensively examined [58–64]. The qualitative impact of the MNP environment on MPI images was investigated in some studies but little information has been presented about the quantitative influence [26, 65].

A detailed understanding of these factors is the first step towards quantitative MPI. Once the underlying and most dominant factors influencing quantitative MPI are known, further improvements in terms of hardware and software developments can be achieved.

Aim of this thesis

This thesis presents a comprehensive characterization of quantitative MPI. The main aim is to investigate the ability of MPI to provide quantitative information about the MNP amount in a measured sample/patient. This includes the questions: Is it possible to extract quantitative information about the MNP amount from MPI measurement data? How accurate are these values? How sensitive is quantitative MPI? What are the factors with the strongest impact on quantitative MPI? Since quantitative MPI is affected by several factors (see figure 1.1), the characterization is divided into three objectives.

The first objective is to investigate the influence of the MPI hardware on quantitative MPI. This includes a detailed study of noise and systematic background signals in the MPI raw signals. The

second objective is to analyze the effects of the data processing steps on the quantitative results with particular focus on the adjustable image reconstruction parameters. The third objective is to investigate the impact of the MNP environment, concentrating on parameters relevant for biomedical applications.

The second aim of this thesis is to demonstrate and assess the potential of quantitative MPI for biomedical applications. This requires that MPI has advantages over the established imaging modalities for MNPs. The advantages and disadvantages of MPI are compared to magnetic resonance imaging, as the most commonly used technique for imaging and quantification of MNPs in biomedical applications. Additionally, special interest is given to imaging of MNPs interacting with living cells, as one of the most promising examples for future applications of quantitative MPI.

Structure of this work

Chapter 2 presents the theoretical basics of magnetic nanoparticles (MNP), magnetic particle spectroscopy (MPS), magnetic particle imaging (MPI), nuclear magnetic resonance (NMR) and magnetic resonance imaging (MRI) and introduces parameters used for the characterization of quantitative measurement techniques. **Chapter** 3 gives an overview of the experimental setup of the measurement systems, with particular focus on the MPI receive hardware components and the implementation of a new gradiometric separate receive coil, designed for improved MPI sensitivity.
The main results of my investigations are presented in the **chapters** 4 to 7. **Chapter** 4 focuses on objective one (MPI hardware), analyzing the influence of the MPI hardware components and the contributions of noise and background signals in the MPI raw signal. **Chapter** 5 concentrates on objective two (Data processing, before image reconstruction) and demonstrates how the MPI raw signals are used for quantification of the MNP amount without the need of an image reconstruction. **Chapter** 6 also focuses on objective two (Data processing, image reconstruction) evaluating the influence of the image reconstruction on the quantitative MPI results. In addition, the limit of detection and accuracy of quantitative MPI are determined and compared with MRI and the impact of the MNP environment is investigated (objective three). **Chapter** 7 deals with objective three (MNP environment) and presents results, demonstrating the potential of quantitative MPI for imaging of cellular processes. A conclusion, outlook and final remarks are given in **chapter** 8.

Chapter 2

Theoretical basics

Sections 2.1, 2.2 and 2.3 provide a brief summary of the theoretical basics of magnetic nanoparticles (MNPs), magnetic particle imaging (MPI) and magnetic resonance imaging (MRI). The aim is to give a fundamental understanding of the underlying physical principles of each technique. Each section cites appropriate references for further reading. Section 2.4 defines parameters used for the characterization of quantitative measurement techniques.

2.1 Magnetic Nanoparticles

Magnetic nanoparticles (MNPs) consist of a magnetic core and a non-magnetic coating (see figure 2.1 a). These materials have unique characteristics, making them attractive for several biomedical applications. The magnetic properties of MNPs allow contactless interaction and detection using non-ionizing magnetic fields. By applying static magnetic fields and field gradients, the MNPs can be moved to certain locations inside the body and used to extract biological substances attached to the MNPs. Dynamic magnetic fields are used for heat generation around the MNPs for hyperthermia treatments to damage diseased tissue or to generate a MNP-specific signal, from which their spatial position can be reconstructed (see section 2.2). The non-magnetic coating serves for improved bio-compatibility and stabilization (preventing MNP aggregation in liquid suspension). Additionally, the MNPs can be functionalized by attaching antibodies or drugs to their surface, which are customized for various applications. The following section presents a basic theoretical model of the magnetic properties of MNPs, which is utilized in section 2.2 to describe the principle of MPI.

Magnetic Properties

The magnetic properties of MNPs are mainly determined by their cores. The size of spherical MNPs is commonly described by the diameter of the core d_c ranging mostly between $5-100\,\text{nm}$ and the diameter of the whole MNP including the non-magnetic coating d_h (also called hydrodynamic diameter) ranging between about $10-200\,\text{nm}$ [66]. The core usually consists of a ferromagnetic material. In biomedical applications, mainly iron-oxide based substances (e.g. magnetite) are used due to their high bio-compatibility. The atomic magnetic moments of a single MNP are coupled by exchange

interaction and can be described by a single magnetic moment. The interaction of this magnetic moment with external magnetic fields is described by the magnetic susceptibility. For biomedical applications mainly the macroscopic effects of an ensemble of several ($> 10^{10}$) MNPs are analyzed and therefore the magnetization $\mathbf{M}$ is of particular interest. A model for the magnetization of an ensemble of MNPs is described by the Langevin equation, visualized in figure 2.1 b) [67]. The magnetization of the MNP ensemble behaves like a classical paramagnet. In the absence of an external magnetic field, no magnetization is formed, since the thermal fluctuations prevent magnetic ordering. Increasing the external magnetic field strength results in an increasing magnetization until saturation (M_0) is reached.

The Langevin theory is capable for a basic description of the magnetic properties of MNPs and to explain the physical principles utilized for MPI. However, there are multiple aspects that are neglected in the Langevin theory, which need to be considered for accurate modeling of the magnetic behavior of MNPs. These aspects include magnetic relaxation (Néel and Borwnian relaxation) [68, 69], magnetic anisotropy [70] and interaction between MNPs e.g. by dipolar interactions [71].

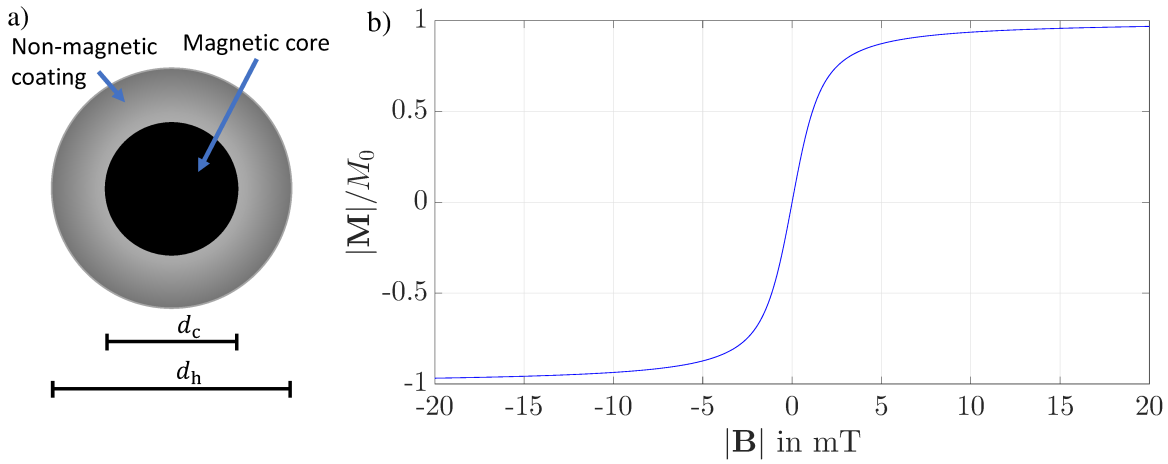

FIGURE 2.1: a) Illustration of a single MNP with the core diameter d_c and the full particle diameter d_h (also called hydrodynamic diameter). b) Absolute of the magnetization $|\mathbf{M}|$ of a MNP ensemble modeled by the Langevin theory as a function of the external magnetic flux density $|\mathbf{B}|$ normalized to the saturation magnetization M_0.

2.2 Magnetic Particle Imaging

This section provides a brief summary about the basic principles used in MPI. A description of the physical processes concerning signal generation and spatial encoding is presented in section 2.2.1 and 2.2.2 respectively. In section 2.2.3 the image reconstruction is derived for system function-based MPI. Further information and mathematical proofs of the presented principles are given in [72].

2.2.1 Signal Generation

Figure 2.2 presents the basic concept of MPI signal generation, which is also utilized in magnetic particle spectroscopy (MPS). A spatially homogenous, sinusoidal magnetic field, called excitation or drive field (figure 2.2 c), with a frequency f_0 and amplitude $|\mathbf{H}_d|$ is used to generate a magnetic response from MNPs. For simplicity it is assumed that the magnetization of the MNP ensemble is described by the Langevin-model, presented in section 2.1 (figure 2.2 a). Inductive receive coils are used to detect the time derivative of the magnetization generated by the MNP ensemble (figure 2.2 b), which represents the MPI raw signal u in the time-domain. The signal is Fourier-transformed $\mathrm{FFT}(u) = \hat{u}$, to distinguish signals generated by MNPs from background signals generated by the excitation fields (figure 2.2 d). The Fourier-transformed signal components $\hat{u}$ are complex numbers and are defined as the MPI raw signal. Due to the non-linear magnetization of MNPs, the amplitude signal spectrum includes higher harmonics of the excitation frequency. Since the Langevin model is point-symmetric, only odd harmonics are generated. The amplitudes of the higher harmonics decrease with increasing frequency. The rate of this decrease towards higher harmonics, also called the "shape" of the spectrum, is mainly determined by the dynamic magnetic behavior of the MNPs. The amplitude of each frequency component is directly proportional to the amount of MNPs, setting the basis for quantitative MPI.

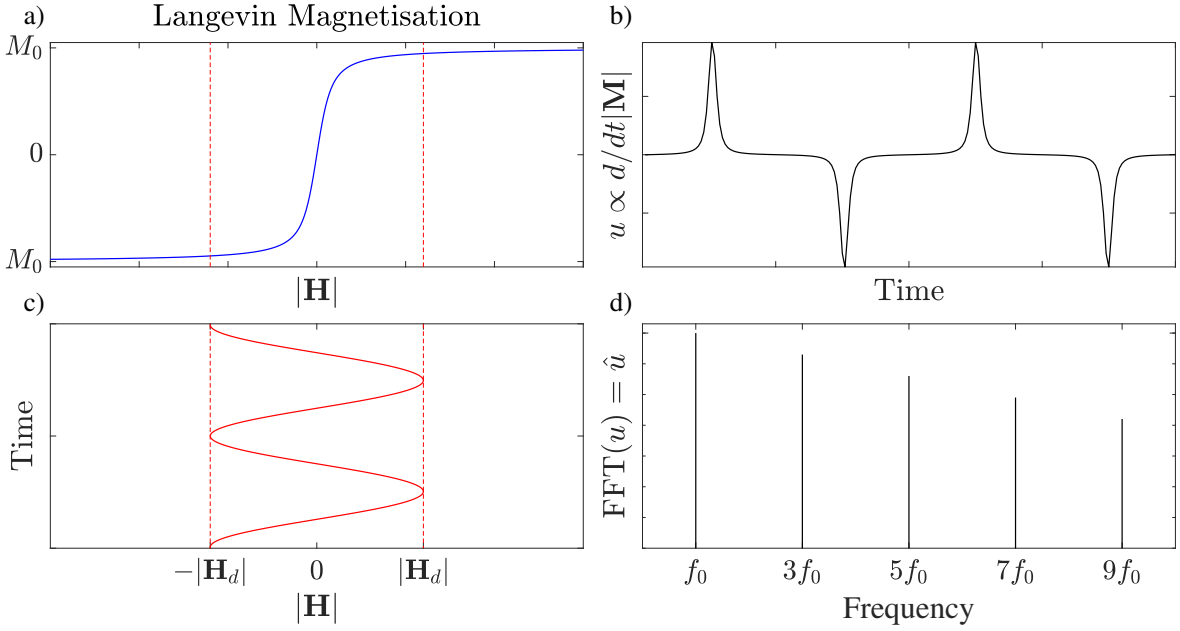

FIGURE 2.2: Basic principle of the MPI signal generation: The magnetization of a MNP ensemble (a) is used to generate a signal based on the excitation with a sinusoidal magnetic field (c). The time derivative of the magnetization is detected by inductive coils (b) and further processed after Fourier-transformation (d). The amplitudes of higher harmonics are defined as the MPI raw signal and are proportional to the MNP quantity.

2.2.2 Spatial Encoding

An imaging technique requires a way of assigning a signal to a certain spatial position. In MPI, this is achieved by superimposing the magnetic fields used for signal generation by an additional static magnetic gradient field. This so called selection field $\mathbf{H}_\mathrm{g}$ is designed to provide a field-free point, from which the magnetic flux density increases linearly in each spatial dimension. A simple and the most common method to generate such a field is by using a coil pair in Maxwell configuration (also called anti-Helmholtz configuration), which generates a magnetic field with a gradient strength G described by the following equation, which is displayed in figure 2.3 a):

$$\mathbf{H}_\mathrm{g} = \mathbf{G} \cdot \mathbf{r} = \begin{pmatrix} G \\ G \\ -2G \end{pmatrix} \cdot \begin{pmatrix} x \\ y \\ z \end{pmatrix} \tag{2.1}$$

The magnetic field experienced by the MNPs is dependent on the spatial position $\mathbf{r}$. For MNPs in the proximity of the field-free point, the selection field is almost zero and has no or minor effects on the signal generation accordingly. Figure 2.4 displays the signal generation for MNPs located further away from the field-free point. Since the magnetization of the MNP ensemble is almost in saturation, the time derivative of the magnetization and thus the MPI raw signal is much lower compared to the case without an offset field. Higher harmonics are generated for even harmonics as well, since the point-symmetry is broken based on the offset field. If the gradient strength G is increased, the volume from which signal is generated decreases. Thus the spatial resolution of MPI is directly linked to the gradient strength.

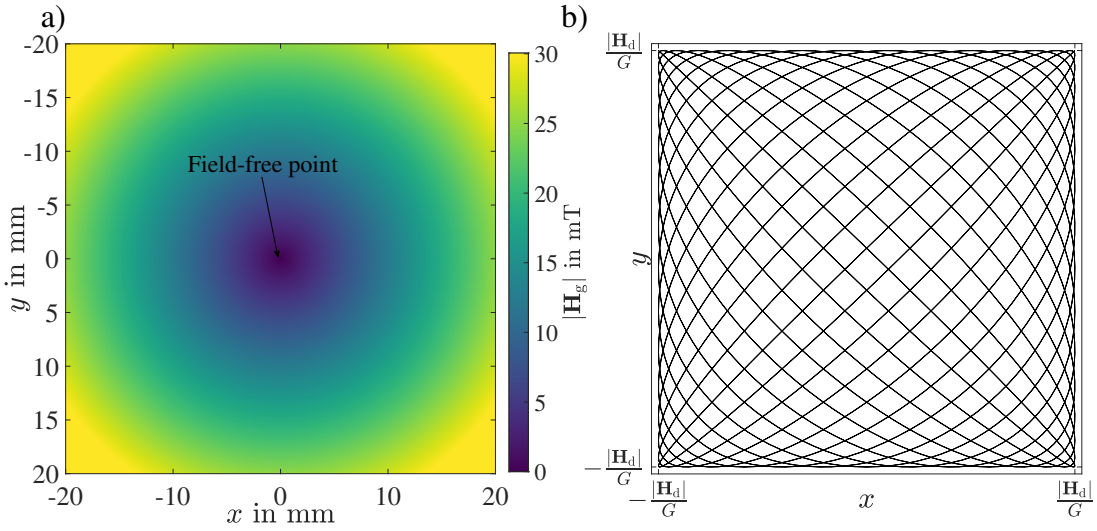

FIGURE 2.3: a) Visualization of the selection field used in MPI for spatial encoding. A field-free point is generated at the center and the magnetic field strength increases linearly from this point in each spatial dimension. b) 2D-Lissajous trajectory, which is used to move the field-free point through the region of interest.

Summing up, signal is mainly generated by MNPs in the proximity of the field-free point when the excitation field is superimposed by the selection field and the generation of higher harmonics is dependent on the MNP position. For imaging of a spatial distribution of MNPs, the field-free point is moved through a defined field of view (FOV), to acquire data and reconstruct the MNP distribution. This is realized either by mechanical movement of the coils (or the object/patient) or by moving the field-free point using magnetic fields. Here, the focus will be set on the field-free point movement based on magnetic fields, as this principle is utilized in the MPI scanner used in this work. The 1D-drive field, used to generate the MPI raw signals, is already moving the field-free point on a straight line. Assuming that $\mathbf{H}_\mathrm{d}$ is parallel to the x-direction, the field-free point is moved between $x = -\frac{|\mathbf{H}_\mathrm{d}|}{G}$ and $x = \frac{|\mathbf{H}_\mathrm{d}|}{G}$. Therefore, the size of the FOV is mainly limited by the drive field amplitude and the gradient strength. If additional drive fields are added for y- and z-direction, the field-free point is moved through a 3D volume. This is achieved by using three sinusoidal magnetic fields with slightly different excitation frequencies for x-, y- and z-direction, which move the field-free point on a Lissajous-trajectory. Figure 2.3 b) displays an exemplary field-free point trajectory for 2D imaging.

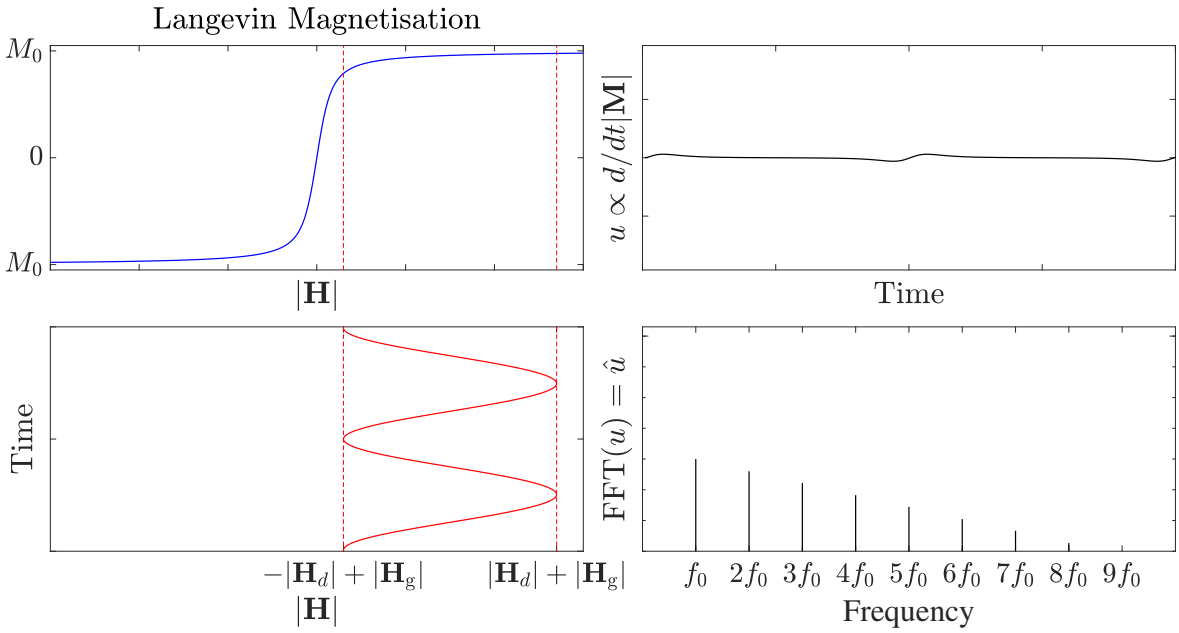

FIGURE 2.4: MPI signal generation principle as presented in figure 2.2 with an additional offset field. This offset field results in saturation of the magnetization leading to a much smaller signal generation, which is utilized for spatial encoding in MPI.

The use of three different excitation frequencies for 3D imaging influences the MPI raw signal generation. Signals are not only generated at higher harmonics of the excitation frequencies but also at mixed frequencies:

$$f = n_x f_x + n_y f_y + n_z f_z \qquad n_x, n_y, n_z \in \mathbb{Z} \tag{2.2}$$

The sum $n_{\mathrm{mo}} = |n_x| + |n_y| + |n_z|$ is defined as the mixing order of the frequency component. The amplitudes of frequency components generated by different mixing orders are dependent on the spatial position and in general decrease with increasing n_{mo} [45, 46]. The spatial dependence of different frequency components is further investigated in section 5.3.

2.2.3 Image reconstruction

Based on the acquired spatially encoded MPI raw signals, the MNP distribution is calculated. Depending on the MPI system and the implemented spatial encoding scheme, multiple approaches have been proposed to reconstruct the MNP distribution [14, 73–75]. Each technique has unique features and advantages in terms of sensitivity, imaging speed, spatial resolution and FOV size. However, the underlying physical and mathematical basics were proven to be the same for each technique [76]. Therefore, only the so called "system function (SF)-based reconstruction" is discussed, which was used for the MPI measurements in this work. From a mathematical point of view, the image reconstruction of the MNP distribution is equivalent to solving an inverse problem. To fully understand this process, it is easier to start with the formulation of the forward problem.

Forward problem

A MNP distribution is given, described in a discrete grid of N equally sized voxels. The MNP concentration of each voxel is defined as one element of the N-dimensional vector $\mathbf{c}$. The MPI raw signal is described as an M-dimensional complex vector $\hat{\mathbf{u}}$, in which each element represents the complex raw signal of one frequency component. The process of applying the excitation and gradient fields, the signal generation and the signal detection is mathematically described by an $M \times N$-matrix $\mathbf{S}$. This matrix includes the influence of several factors (dynamic magnetic behavior of MNPs, spatial position, environmental conditions, hardware components, etc.) on the received signals, and is often referred to as system matrix or system function (SF). The forward problem is then formulated as follows:

$$\hat{\mathbf{u}} = \mathbf{S} \cdot \mathbf{c} \tag{2.3}$$

Since no theoretical model is sufficient to accurately determine the SF including each influencing factor, it is usually acquired experimentally. This is performed by preparing a small sample of MNPs in a defined volume, which is then moved on a discrete grid to N spatial positions to acquire the MPI raw signals representing the columns of $\mathbf{S}$. The process of acquiring the SF for the whole imaging FOV is very time demanding and takes hours up to days.

Inverse problem

The inverse problem describes the process of reconstructing the MNP distribution $\mathbf{c}$. This requires the knowledge of the measured MPI raw signal $\hat{\mathbf{u}}$ and the SF $\mathbf{S}$. A major problem for the image reconstruction is that the measured $\hat{\mathbf{u}}$ and $\mathbf{S}$ are disturbed by noise. This means that the existence,

uniqueness and stability of a solution is not guaranteed, making this a so called ill-posed problem [77]. To overcome this problem, an approximate solution is searched, which is achieved by using least-square minimization of the residual vector:

$$\left|\left|\mathbf{S}\cdot\mathbf{c}-\hat{\mathbf{u}}\right|\right|_2^2 \xrightarrow{\mathbf{c}} \min \tag{2.4}$$

To further deal with random noise of the measurement data, regularization techniques are employed. The most common technique is the Tikhonov regularization, which adds a term to equation 2.4:

$$\left|\left|\mathbf{S}\cdot\mathbf{c}-\hat{\mathbf{u}}\right|\right|_2^2+\lambda\left|\left|\mathbf{c}\right|\right|_2^2 \xrightarrow{\mathbf{c}} \min \tag{2.5}$$

with the regularization parameter λ. Multiple algorithms can be utilized to solve this problem. The Kaczmarz algorithm is the most common method for MPI applications [78]. The influence of the image reconstruction and the reconstruction parameters on the final image is part of this thesis and will be further analyzed in section 6.1.

The calculated MNP distribution $\mathbf{c}$ is usually presented in a grey scale image with intensities I, called the MPI image. Theoretically, these intensities are directly proportional to the amount of MNPs inside each voxel. Quantification of the MNP amount is mostly performed in terms of the iron concentration c_{Fe} or the iron mass m_{Fe}, which enables comparisons of different MNP types. The conversion of the image intensities into the MPI-determined iron mass $m_{\mathrm{Fe,MPI}}$ is performed using the iron mass of the sample used for SF acquisition $m_{\mathrm{Fe,SF}}$:

$$m_{\mathrm{Fe,MPI}} = I\, m_{\mathrm{Fe,SF}} \tag{2.6}$$

In the same way the MPI-determined iron concentration $c_{\mathrm{Fe,MPI}}$ is calculated for each voxel, if the iron concentration of the sample used for the SF acquisition $c_{\mathrm{Fe,SF}}$ is known:

$$c_{\mathrm{Fe,MPI}} = I\, c_{\mathrm{Fe,SF}} \tag{2.7}$$

Multi-color MPI

The SF-based reconstruction technique yields accurate reconstruction results only, if each parameter (drive fields, selection fields, MNP type, MNP environment, etc.) during the measurement matches to the parameters present during SF acquisition. If for instance a measurement is performed at a different temperature compared to the SF acquisition, the detected MPI raw signals are different and are not identified correctly in the image reconstruction. This leads to imaging artifacts (e.g. signal amplitudes in regions where no MNPs are located) and quantification errors. Rahmer et al. have presented a method to correct these errors [79]. This technique, called multi-contrast or multi-color MPI, is based on the incorporation of the effects of changing parameters (e.g. changing temperature) into the image reconstruction by adapting the SF. Let's assume a measurement of two MNP distributions characterized

by two different sets of parameters is performed. The two MNP distributions are given by $\mathbf{c}_1$ and $\mathbf{c}_2$. The different MPI raw signals generated by these MNPs are described by their respective SFs $\mathbf{S}_1$ and $\mathbf{S}_2$ and hence the forward problem can be formulated as:

$$\hat{\mathbf{u}} = \mathbf{S}_1 \cdot \mathbf{c}_1 + \mathbf{S}_2 \cdot \mathbf{c}_2 \tag{2.8}$$

If both SFs are known, they can be combined for image reconstruction as follows:

$$\left\| [\mathbf{S}_1 \mathbf{S}_2] \cdot \begin{pmatrix} \mathbf{c}_1 \\ \mathbf{c}_2 \end{pmatrix} - \hat{\mathbf{u}} \right\|_2^2 + \lambda \left\| \begin{pmatrix} \mathbf{c}_1 \\ \mathbf{c}_2 \end{pmatrix} \right\|_2^2 \xrightarrow{\mathbf{c}_1, \mathbf{c}_2} \min \tag{2.9}$$

This inverse problem is solved in a similar way as described previously using the Kaczmarz algorithm. Based on the reconstructed results, the two MNP distributions $\mathbf{c}_1$ and $\mathbf{c}_2$ can be distinguished. This technique not only prevents image distortions and quantification errors but also allows to extract additional information about the local MNP environment from the MPI results. However, from a mathematical point of view, the number of variables are doubled for the same number of equations, which complicates the image reconstruction. Recent studies utilized this technique to quantify the local temperature and viscosity around MNPs [80, 81]. Advantages of multi-color MPI are analyzed in more detail in chapter 7.

2.3 Magnetic Resonance Imaging

Magnetic resonance imaging (MRI) is one of the most common tomographic imaging techniques used for biomedical applications. MRI provides anatomical images with a sub-millimeter resolution without using ionizing radiation. MRI is the "gold standard" when it comes to quantitative imaging of MNPs for biomedical applications and is therefore used and compared to MPI in this study to investigate the advantages and disadvantages of both techniques. In the following, a summary of the basic principles used in MRI and the influence of MNPs on the MRI signal is presented.

2.3.1 Nuclear magnetic resonance

The principle of MRI is based on nuclear magnetic resonance (NMR) of hydrogen nuclei (protons). The most important characteristics of these hydrogen nuclei for NMR is their spin. Although the spin is a quantum mechanical property resulting from the Dirac equation, a basic description of NMR can be made using a model based on classical physics only [82]. The spin of a hdydrogen nucleus is coupled with an angular momentum and with a magnetic moment. In the absence of external magnetic fields, no energetically favored direction for the magnetic moments exist and they are distributed evenly in each direction (see figure 2.5 a)). Placing these nuclei in a strong, spatially homogenous static magnetic field $\mathbf{B}_0$ (parallel to z-axis) of flux densities up to several tesla, leads to a precession of each individual magnetic moment around the external field vector with the Larmor frequency $\omega_\mathrm{L} = \gamma |\mathbf{B}_0|$,

where γ is the gyromagnetic ratio. Additionally, the magnetic moments tend to align parallel to the external magnetic field, since this is the energetically favored state (see figure 2.5 b)). Compared to thermal fluctuations, the magnetic energy is much smaller, resulting in the formation of only a small net magnetization.

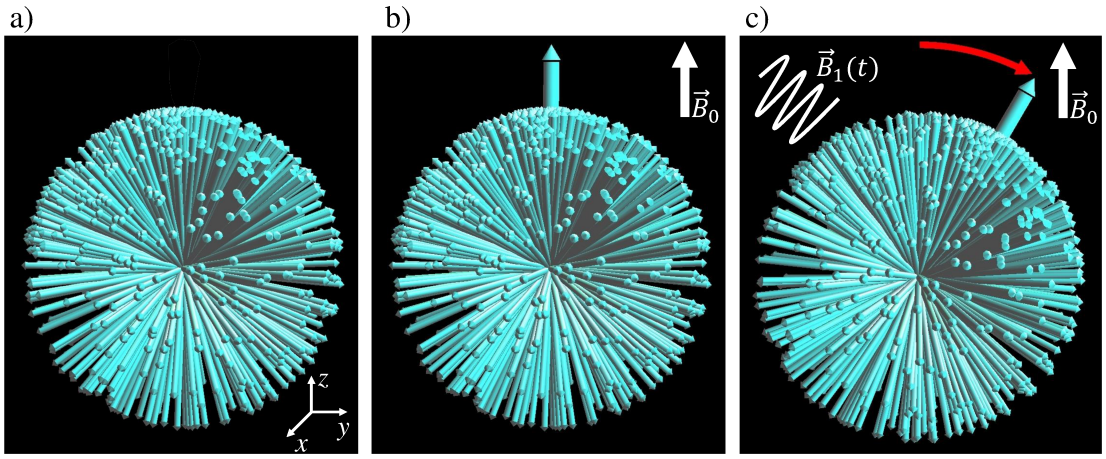

FIGURE 2.5: a) Visualization of an ensemble of magnetic moments of hydrogen nuclei in the abscence of external magnetic fields. b) An external static magnetic field $\mathbf{B}_0$ parallel to the z-axis is applied and leads to the formation of a net magnetization and the precession of each individual magnetic moment around the z-axis. c) A time-varying magnetic field ($\mathbf{B}_1 \perp \mathbf{B}_0$ also called radiofrequency pulse) is applied which is in resonance with the Larmor frequency ω_0 and leads to the rotation of each spin and therefore the net magnetization into the x-y-plane. Figure adapted from [82].

If an additional time-dependent magnetic field $\mathbf{B}_1(t)$ (also called radiofrequency (RF) pulse) is applied, orthogonal to $\mathbf{B}_0$ and in resonance with the Larmor frequency, the magnetic moments also precess around $\mathbf{B}_1(t)$. From a stationary reference frame, this precession looks like a rotation of the net magnetization from the longitudinal (z-) into the transverse (x-y-) plane. If $\mathbf{B}_1(t)$ is not in resonance with the Larmor frequency, the angle of rotation is not fixed and no transverse magnetization is formed. The amplitude and the duration in which $\mathbf{B}_1(t)$ is applied determine the angle of rotation (flip angle). After the RF-pulse is applied and the net magnetization is rotated into the x-y-plane, the NMR signal is acquired. Since each individual magnetic moment still precesses around $\mathbf{B}_0$, the net magnetization also precesses around $\mathbf{B}_0$, which is measured using inductive receive coils installed in the x-y-plane. The measured signal amplitude is mainly determined by the proton density and two relaxation processes.

The first relaxation process is called transverse or T_2 relaxation, which leads to an exponential signal decay of the transverse magnetization. The decay is characterized by the transverse relaxation time T_2 defined as the time when the transverse magnetization reaches $1/e \approx 37\,\%$ of the maximal value (see figure 2.6 b)). Transverse relaxation is caused by interactions between the magnetic moments, changing the local magnetic field strength and hence the Larmor frequency. Therefore some magnetic moments precess faster or slower compared to the rest, leading to a decreasing net transverse magnetization, which is also called dephasing of the spin ensemble.

The second relaxation process is called longitudinal relaxation and describes the realignment of the magnetic moments along $\mathbf{B}_0$. This process is caused by interactions between the magnetic moments with the environment and can also be described by an exponential function, using the relaxation time T_1 (see figure 2.6 a)). T_1 is defined as the time when the longitudinal magnetization reaches $1-1/e \approx 63\,\%$ of the maximal value. Both relaxation times and the proton density are tissue-dependent, which results in the contrast between different organs in the MRI image.

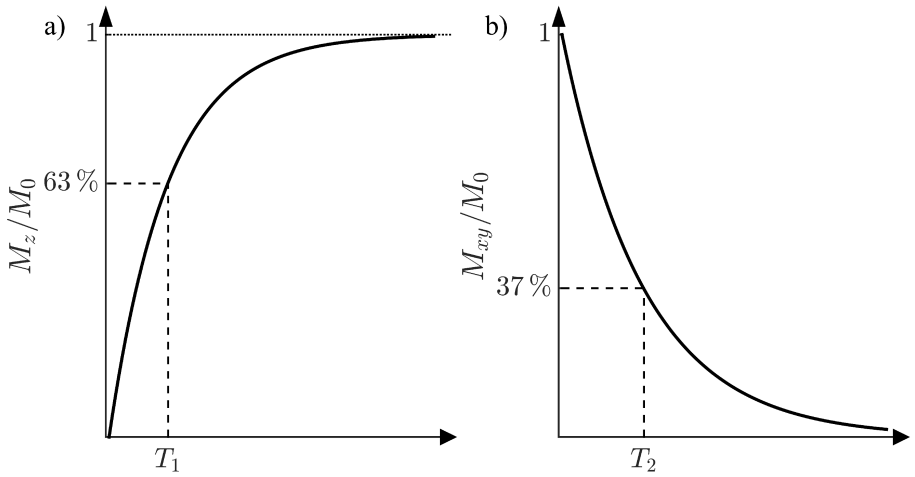

FIGURE 2.6: Visualization of the longitudinal (a) and transverse (b) relaxation processes in MRI. After applying the RF-pulse, the longitudinal magnetization M_z relaxes back to the state of thermal equilibrium. The longitudinal relaxation time T_1 is defined by the time when 63 % of the maximal value is reached. The transverse magnetization $M_{x,y}$ decreases over time and is characterized by the relaxation time T_2, defined by the time when the signal is reaching 37 % of the maximal value.

2.3.2 Spatial encoding and image reconstruction

Spatial encoding of the signal is achieved by magnetic gradients, which change the Larmor frequency depending on the spatial position. By choosing the bandwidth of the RF-pulse, the spatial region, in which signal is generated, is selected. Additional gradients are used to encode spatial information in the frequency and phase of the received MRI signal. This signal is utilized to reconstruct the MRI image via Fourier-transformation. The combination of RF-pulses and magnetic gradients of certain strength and duration is called a pulse sequence. Different pulse sequences are used depending on the application, e.g. to increase a specific tissue-contrast. A more detailed mathematical description of NMR, MRI physics and different pulse sequences is given in [83, 84].

2.3.3 Influence of MNPs

In MRI, MNPs are mainly used as contrast agents. A contrast agent serves to improve the visibility of a certain region of interest by increasing the signal difference of that area compared to the surroundings [85]. The effects of MNPs on the MRI signal are diverse, mainly depending on the MNP properties [86, 87]. MNPs lead to a decrease of the longitudinal and transverse relaxation

times. This decrease is caused by a faster dephasing of the spin ensemble based on the strong field distortions induced by the magnetization of MNPs. Depending on the MRI sequence, MNPs are used to generate positive or negative contrast. In most MRI images, MNPs appear as negative contrast, due to the shortening of T_2 and therefore a fast signal decay. Positive contrast images can be obtained by employing the T_1-shortening effect of MNPs [88]. Whether MNPs cause positive or negative contrast, depends on the MNP concentration and the MRI measurement and pulse sequence parameters [89].

Quantification of the MNP amount is achieved by determining the relaxation times from the MRI data. The relaxation rates $R_1 = 1/T_1$ and $R_2 = 1/T_2$ increase linearly with the MNP concentration:

$$R_i = R_{i,\mathrm{NoMNP}} + r_i\, c_{\mathrm{MNP}} \qquad i = 1,2. \tag{2.10}$$

The relaxivities r_1 and r_2 define the slope of this increase. If the relaxivity and the MNP-induced change of R_1 or R_2 is known, the MNP concentration can be calculated for each pixel using:

$$c_{\mathrm{MNP,MRI}} = \frac{R_i - R_{i,\mathrm{NoMNP}}}{r_i} \tag{2.11}$$

2.4 Characterization of a quantitative measurement technique

A main goal of this work is to characterize the performance of MPI regarding quantification of MNPs. Characterization is a broad term with multiple definitions. Several quantitative parameters can be found in the literature for characterizing analytical measurement techniques. Here, the focus will lay on three commonly-used parameters, which are introduced in this section. A more in-depth description of these and additional parameters is given in [90].

2.4.1 Linearity

Linearity is an important requirement for quantitative measurement techniques. It describes the correlation between the experimentally determined value y and the amount or concentration of the analyte x. Scott et al. proposed a way for quantifying the linearity using the response index r determined by fitting with the function [91]:

$$y = ax^r \tag{2.12}$$

A perfect linear relationship would yield $r = 1$, which can not be achieved due to imperfections of the measurement process. A measurement technique fulfills the linearity requirement if r lies in a certain range, commonly chosen arbitrarily to be $0.97 < r < 1.03$. The conditions of linearity are only satisfied in a certain analyte-concentration range. In the case of MPI, mainly the lower limit of this range is of interest, which is described in more detail in section 2.4.2.

2.4.2 Limit of detection

The limit of detection is used to describe the smallest amount or concentration of an analyte that is reliably detected by a measurement technique. In the literature, several different definitions for the limit of detection can be found. In this work, a definition is used based on the signal-to-noise ratio (SNR). The limit of detection is defined for the amount or concentration of the analyte, for which an SNR $= 3$ is obtained [90, 92]. In the same way, a limit of quantification is defined, which defines the lowest amount or concentration of an analyte, that is quantified with a certain accuracy (see section 2.4.3). Commonly the limit of quantification is defined by an SNR $= 9$, which is equal to three times the limit of detection [90]. In this work, the term "upper limit of detection" is used to refer to the largest amount or concentration of an analyte that fulfills the linearity condition presented in section 2.4.1. The range between the lower and upper limit of detection is also called the linear dynamic range, in which quantification of the analyte can be performed.

2.4.3 Accuracy

There is no generally accepted definition of the term accuracy. ISO 5725 defines accuracy as a combination of the terms trueness and precision, which will be used in this work [93]. Trueness refers to the deviation of the measured value from the true (or accepted reference) value y_{ref} and precision refers to the deviation between multiple identical measurements. Figure 2.7 depicts a visual summary of both terms. A quantitative evaluation of the qualitative term trueness is performed by determining the bias of the measurement $u_{bias} = \bar{y} - y_{ref}$ using the mean over multiple identically conducted measurements $\bar{y}$. The standard deviation s over multiple identically conducted measurements is used as a measure for the qualitative term precision. A high accuracy is achieved if both, trueness and precision, are high. A combination of these two values leads to the combined standard uncertainty u_c, which is used in this work for quantification of the accuracy of a measurement technique [90]:

$$u_c = \sqrt{s^2 + u_{bias}^2} \tag{2.13}$$

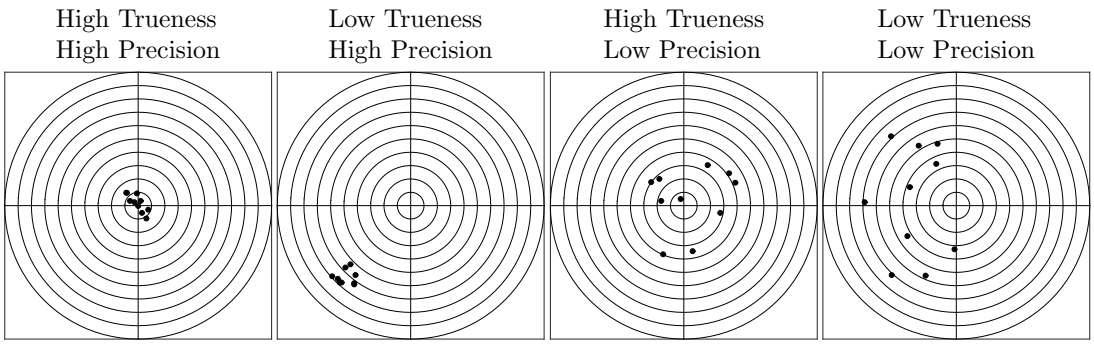

FIGURE 2.7: Visual depiction of trueness and precision. The center of the target represents the true value and the black dots the experimentally determined value of individual measurements. A high accuracy is achieved for a high precision and high trueness.

Chapter 3

Experimental setup

This chapter introduces the basic experimental setups of the magnetic particle imaging system, magnetic particle spectrometer, nuclear magnetic resonance system, magnetic resonance imaging system and the properties of the MNP types that were used in this thesis. The aim is to give an overview about the system specifications and the utilized physical principles of each system. The descriptions of the specific experimental setups for the different measurements performed in this thesis are stated at the beginning of each section, in which these measurements are presented. A summary of the MPI measurement parameter used for each experiment is given in the Appendix A.

3.1 Magnetic particle imaging system

The following section presents the experimental setup of the MPI system used for each MPI measurement performed in this work. Section 3.1.1 describes the fundamental hardware components of the system and the basic procedure of how an MPI image is obtained. Section 3.1.2 gives an overview about the system-specific parameters. Section 3.1.3 presents more detailed information about the receive hardware components, which are of particular interest for a quantitative analysis of MPI measurement data. Especially the design and the properties of a separate receive-only coil, optimized for MPI applications is described.

3.1.1 Basic experimental setup

MPI is based on the generation of different magnetic fields to excite a magnetic response of an MNP ensemble (see section 2.2). These magnetic fields are generated (transmitted) and detected (received) using electromagnetic coils. Figure 3.1 displays the schematic process of a conventional MPI measurement.

FIGURE 3.1: Schematic sequence of operations during a conventional MPI measurement.

In the first step, the static selection or gradient field is produced by a large coil pair in anti-Helmholtz configuration installed with the symmetry axis parallel to the z-axis (see figure 3.2).

In the second step three orthogonal drive or excitation fields are generated by three individual coils in x-, y- and z-direction. The drive fields in y- and z-direction are generated by two saddle coil pairs in Helmholtz configuration, called the y-TxRx (TxRx=transmit-receive) and z-TxRx-coils. The drive field in x-direction is generated by a single solenoid coil (x-TxRx).

In the third step, the MNP response is detected (received). In many MPI scanners, this is performed using the same coils, which are used for the generation of the drive fields, which is why they are called transmit-receive (TxRx)-coils. In the used MPI system, an additional separate receive-only (Rx)-coil was implemented and used instead of the z-TxRx-coil. Reasons for the incorporation of a separate receive coil and more detailed information about the receive hardware is given in section 3.1.3.

In the fourth step, the signals are pre-processed depending on the application (e.g. signal filtering, averaging, etc.) and finally the image is reconstructed. Image reconstructions are performed in the frequency domain based on the SF-approach, using a measurement-based SF as described in section 2.2.3.

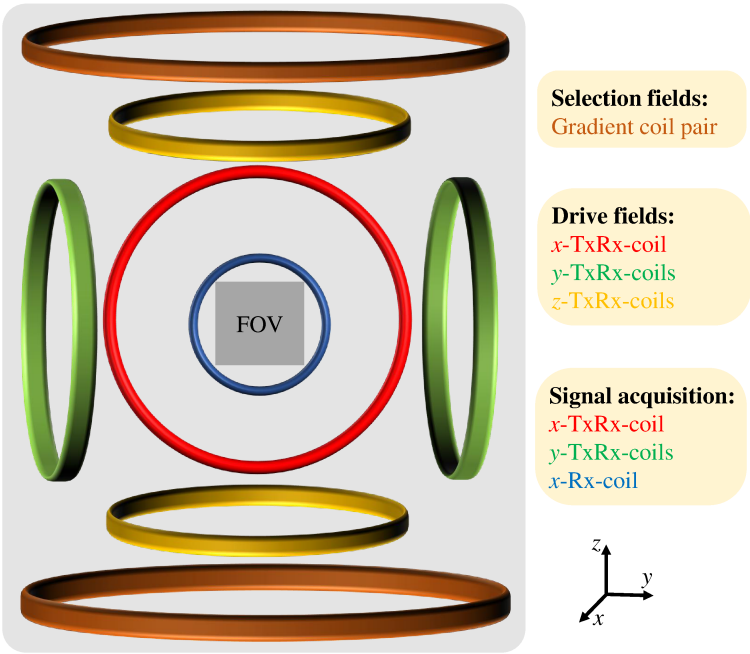

FIGURE 3.2: Schematic setup of the used MPI system. A large coil pair generates the static magnetic gradient field (brown). Three additional coils or coil pairs are used to produce the drive fields for the x-, y- and z-direction (red, green, yellow). For signal acquisition, two of the three drive field coils (x- and y-direction) and one additional separate receive coil (blue) are used.

3.1.2 System specifications

Each MPI measurement of this thesis was acquired on a commercial, preclinical system (MPI 25/20 FF, Bruker Biospin) installed at Charitė university hospital Berlin (see figure 3.3). The scanner frontend is

located in a low-frequency shielded room. The imaging FOV is centered in the scanner bore (parallel to x-axis) with an accessible diameter of about 6.5 cm. System electronics, cooling units and operating consoles are located outside the shielded environment. The Bruker ParaVision software is used for control of the measurement parameters, data acquisition and data storage.

The gradient coils generate a field free point in the center of the scanner bore, with an adjustable gradient strength of maximal $1.25/1.25/2.5\,\mathrm{T/m}$ (x/y/z-direction). The $1/1/2$ ratio is caused by the geometrical setup of the coils. The drive field frequencies are fixed to $f_x \approx 24.51, f_y \approx 26.04, f_z \approx 25.25\,\mathrm{kHz}$. Their amplitudes can be varied individually between $B_i = 0 - 12\,\mathrm{mT}$ $(i = x,\ y,\ z)$. The high power required to achieve such high amplitudes is provided by resonant circuits tuned to the respective frequency f_x, f_y or f_z. The data for a full 3D MPI image is obtained in 21.5 ms. Sampling of the measurement data is performed with a bandwidth of 1.25 MHz, resulting in a spectral resolution of 46.42 Hz over a frequency range of $0 - 1250\,\mathrm{kHz}$. SF acquisitions are performed experimentally using an in-build robotic sample positioning unit (see figure 3.3), which enables sub-millimeter precise 3D-positioning of small samples inside the field of view. Processing of the measured data and the image reconstruction is performed using self-written and open source Matlab codes (Mathworks, USA).

FIGURE 3.3: Left: MPI scanner frontend located inside the copper-shielded room. Right: Sample holder mounted to MPI calibration robot used for sample positioning and SF acquisitions.

3.1.3 MPI receive hardware

Figure 3.4 a) displays the full transmit-receive chain of a conventional dual-purpose (transmit and receive) coil. A digital-to analogue converter (D/A) controls the current generation for the drive fields. Amplification is achieved using power amplifiers (PA) and distortions are filtered using band-pass-filters (BPF) around 25 kHz. The filtered signal is connected to the TxRx-coil to generate the drive field. The same coil is used for signal generation, which allows for a compact, space-saving design. The use of the same coil for signal excitation and detection is theoretically possible since the currents

generating the drive fields are limited to the respective excitation frequencies, while the MPI raw signal is detected at higher frequencies. Hence, a band-stop-filter (BSF) is used to block the excitation frequency from the measured signal. The remaining signal is amplified using low-noise-amplifiers (LNA) and converted into digital units using analogue-to-digital converter (A/D).

In reality, the simultaneous presence of the large currents generating the excitation fields and much smaller (more than six orders of magnitude) currents induced by MNPs lead to distortions and background signals in the MPI raw data. This is mainly caused by non-linearities of hardware components in the transmit and receive chain, and thus the formation of higher harmonics, which are not filtered. Hence, a clear identification of the undistorted MNP signal at these frequencies is challenging.

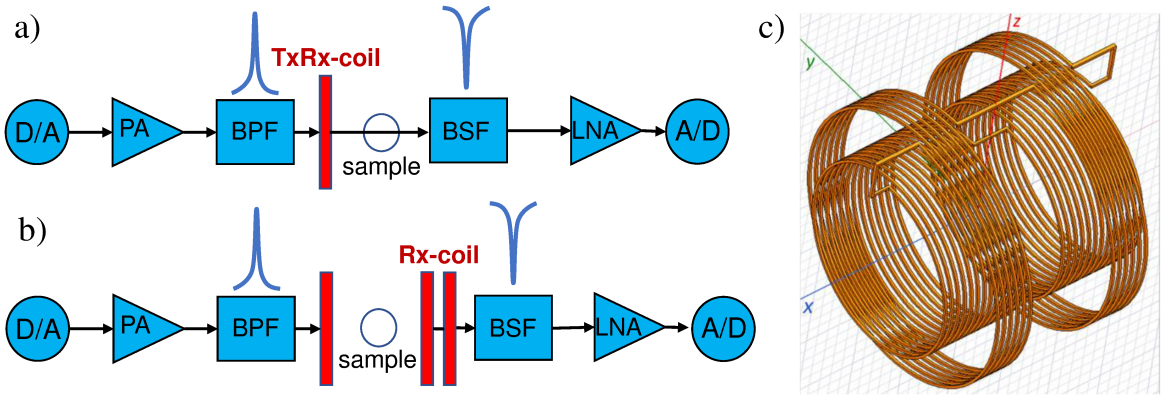

FIGURE 3.4: a) Full transmit-receive chain for standard dual-purpose coils: A digital-to-analogue converter (D/A) controls the signal generation, which is amplified using power amplifiers (PA), band-pass-filtered (BPF) and connected to the transmit-receive coil (TxRx-coil). The same coil is used for signal acquisition using band-stop filters (BSF) and low-noise amplifiers (LNA). An analogue-to-digital converter (A/D) is used to convert the signal into digital units. b) transmit-receive chain for receive only coil (Rx-coil). c) Design of the gradiometric separate receive coil (Rx-coil) consisting of an inner pick-up coil and an outer cancellation coil with opposing winding directions.

To circumvent these obstacles, a dedicated receive-only coil (Rx-coil) was built to decouple the transmit-receive-chain and to increase the overall MPI performance (see transmit-receive chain in figure 3.4 b). The design was made and manufacturing of this coil was performed by Bruker (Bruker BioSpin, Ettlingen). The coil was designed as a second-order gradiometer, consisting of two different diameters for pick-up ($R = 36\,\text{mm}$, 2x13 turns of copper litz-wire) and cancellation coil ($R = 52\,\text{mm}$, 2x6 turns of copper litz-wire) with opposing winding directions (figure 3.4 c). This gradiometric design allows the suppression of signals generated by spatially homogenous magnetic fields (e.g. the drive fields) [94–97]. If the pick-up and cancellation coil detect the same magnetic flux, the induced voltage in both coil parts are the same and cancel each other out, because of the opposing winding direction. The magnetic flux generated by MNPs is mainly detected by the pick-up coil and is not or only partially measured by the cancellation coil and thus is not canceled out.

Based on the larger radius of the cancellation coil, a large area of homogenous sensitivity was achieved, without big sensitivity degradations at the edges of the FOV. Overall, the diameter of the Rx-coil were chosen smaller compared to the diameter of the TxRx-coils (x-TxRx-coil: $R = 80\,\text{mm}$, 25 turns of copper litz-wire, size comparison of both coils shown in figure 3.5) to be able to fit it inside the scanner bore and more importantly, to increase the sensitivity due to the smaller distance to the signal sources. With an accessible bore diameter of 65 mm, it is optimized for small rodent studies. Inductance and capacity of the Rx-coil were chosen to be compatible with the in-built hardware components of the preclinical MPI scanner. Since the system hardware and software are limited to the simultaneous use of maximal three receive coils, the Rx-coil was installed and used instead of the z-TxRx-coil. A characterization of the improvements gained by this coil compared to the standard dual-purpose coils is part of this work and will be presented in chapter 4.

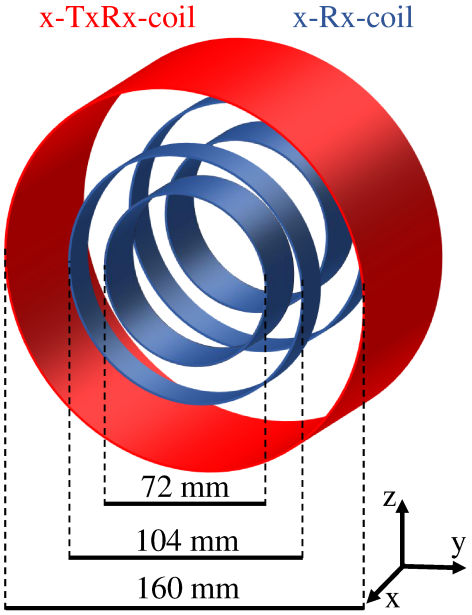

FIGURE 3.5: Models of the dual purpose (x-TxRx) and the separate receive-only (x-Rx) coils. Both coils are installed parallel to the x-direction of the MPI scanner and are used for signal acquisition.

3.2 Magnetic particle spectrometer (MPS)

A magnetic particle spectrometer (MPS) can be described as a "0D-MPI scanner" and works based on the same physical principal as MPI without using magnetic gradient fields for spatial encoding. Originally, MPS was developed to serve as a tool for the easy and fast analysis of new MNP types and their MPI performance [98]. Now, MPS is also used for quantification of MNPs in biological samples and to analyze changes of the dynamic magnetic behavior caused by interactions of MNPs with biological substances [63, 99].

In this work, MPS measurements were performed to compare the results with the MPI raw measurement data. A commercial system was used (MPS-3, Bruker BioSpin), which is shown in

figure 3.6 a). Signal excitation is performed in one axis with a spatially homogenous, oscillating magnetic field at $f = 25.25\,\mathrm{kHz}$. The amplitude can be varied between $B = 0 - 25\,\mathrm{mT}$. Signal acquisition of higher harmonics generated by MNPs is performed with a gradiometric coil (inner radius $R = 6\,\mathrm{mm}$). The excitation frequency is filtered and the remaining signal is amplified and further processed in the frequency domain. Empty sample holder measurements are subtracted, to remove time-constant background signals. Multiple sample holders can be mounted to the system, allowing measurements of different vessels for volumes of $< 200\,\mu\mathrm{L}$. The spatially inhomogeneous sensitivity profile of the receive coil were corrected by reference measurements of known amounts of MNPs for each sample containing $> 100\,\mu\mathrm{L}$.

The system converts the acquired voltages into magnetic moments based on a previously performed calibration using a reference coil. These magnetic moments are used for quantification of the MNP amount. The iron amount of a measured sample is determined based on a reference measurement using a sample with known $m_{\mathrm{Fe,ref}}$:

$$m_{\mathrm{Fe}} = |\hat{u}_3| \frac{m_{\mathrm{Fe,ref}}}{|\hat{u}_{3,\mathrm{ref}}|}. \tag{3.1}$$

$|\hat{u}_3|$ denotes the amplitude of the third harmonic of the excitation frequency. An additional parameter, which can be extracted from the MPS spectrum, is the ratio between the fifth and the third harmonic ($|\hat{u}_5|/|\hat{u}_3|$). This parameter is used to quantify the signal decay towards higher harmonics, which is in general independent from the MNP quantity and a hallmark for the dynamic magnetic behavior of the MNPs in the sample.

3.3 Nuclear magnetic resonance (NMR) system

A NMR system works on the same physical principle as MRI without using magnetic gradients for spatial encoding. In general NMR allows higher sensitivities compared to MRI due to the lack of magnetic gradients and smaller coil geometries. In this work, NMR measurements were performed using a commercial mq60 NMR relaxometer (Bruker BioSpin, see figure 3.6 b).

A homogenous magnetic field of 1.5 T is generated by electromagnets and additional coils are used to generate the RF-pulses and to acquire the signal. Sample volumes up to about $500\,\mu\mathrm{L}$ can be measured, limited by the spatial sensitivity profile of the receive coil. MNP quantification was performed using a Carr-Purcell-Meiboom-Gill (CPMG) spin-echo sequence to determine R_2 [100]. This sequence uses an initial 90°-pulse for signal excitation, followed by a train of 180°-pulses for signal refocusing at time intervals $n \cdot TE - TE/2,\ (n \in \mathbb{N})$. The transverse magnetization is measured at the so called echo times $n \cdot TE$. The transverse relaxation time is calculated by performing a mono-exponential fit using the signal amplitudes acquired for varying TE. The choice of TE has to be adapted to cover most of the exponential signal decay and is limited by a minimal achievable $TE \geq 0.04$ ms.

3.4 Magnetic resonance imaging (MRI) system

MRI measurements presented in this work were performed using a preclinical 1 T ICON system (Bruker Biospin, see figure 3.6 c). The system is equipped with a whole-body receive coil optimized for rodent studies. Magnetic gradients, used for spatial encoding, can be varied up to gradient strengths of 390 mT/m. This enables imaging of a maximal FOV of about 100x50x50 mm^3 limited by the sensitivity profile of the receive coil with an achievable spatial resolution down to about 0.2 mm^3.

Multiple pulse sequences can be used to acquire imaging data. Quantification of MNPs is mainly performed by analyzing changes of the transverse relaxation time (see section 2.3.3). A CPMG spin-echo sequence was used to determine R_2 (see section 3.3). This sequence acquires multiple images of the same slice with varying TE. Exponential fits are performed pixel-wise using the signal intensities to extract R_2. The range of TE is modified to cover the full exponential decay, mainly influenced by the MNP concentration. The MRI system is limited by an minimal $TE \geq 5$ ms. Long repetition time (TR) were chosen to minimize effects caused by the longitudinal relaxation time. The imaging FOV were adjusted manually to cover the whole region of interest and to avoid additional distortions by air or aliasing artifacts.

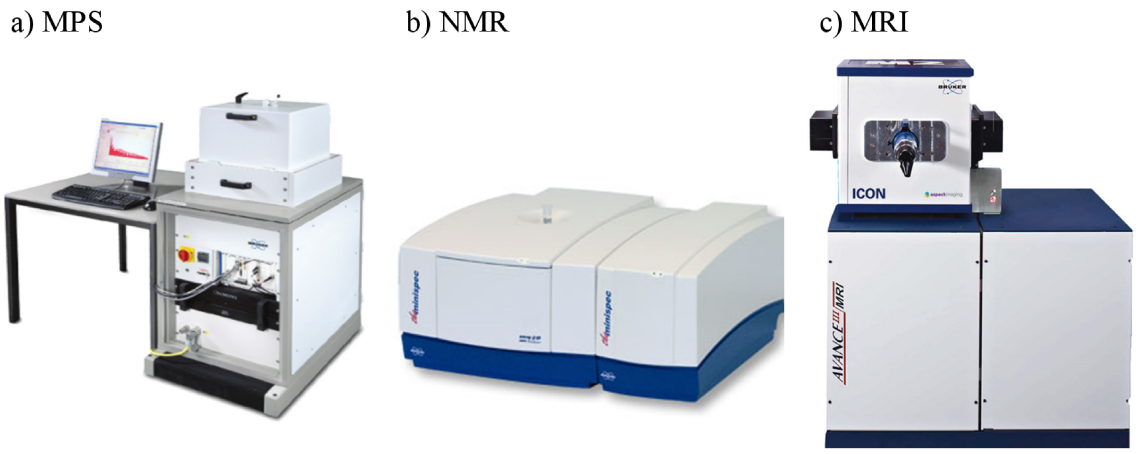

FIGURE 3.6: Photographs of the MPS, NMR and MRI system used in this work.

3.5 Magnetic nanoparticle (MNP) types

This section presents the main properties of the two MNP types namely Ferucarbotran and Synomag used for the measurements in this thesis. In general, MNPs are stored in liquid suspension consisting of pure water. Here, each MNP concentration is presented in terms of the respective iron concentration and the dilution medium is pure water unless additional information about the dilution medium is stated.

3.5.1 Ferucarbotran

Ferucarbotran (Meito Sangyo, Japan), a precursor of the MRI-contrast agent Resovist, was used for most phantom measurements presented in this work [101]. Ferucarbotran is widely used in MPI research for several applications and referred to as a "quasi-standard" material, due to the high MPI signal generation, commercial availability and reproducibility [26, 39, 81, 102, 103]. The MNPs consist of iron oxide crystals with a mean size of 5 nm, forming colloidally stable clusters. Dextran-coating prevents particle interactions and agglomeration with a hydrodynamic diameter of about 60 nm. The dynamic magnetic behavior shows no concentration-dependent changes over a wide iron concentration range of $0-940\,\mathrm{mmol/L}$, making Ferucarbotran especially attractive for characterization of the quantification performance of an MPI system [104].

Ferucarbotran has also been used as a contrast agent for MRI, especially for enhanced liver-contrast. The values for the transverse relaxivity r_2 reported in literature vary between $r_2 = 61\,\mathrm{L mmol^{-1} s^{-1}}$ and $r_2 = 186\,\mathrm{L mmol^{-1} s^{-1}}$ [101, 105–107]. More details about the magnetic properties of Ferucarbotran are given in [108, 109].

3.5.2 Synomag

Synomag (Micromod, Germany) is an MNP type, optimized for MPI and magnetic hyperthermia applications. The particles consists of a multi-core structure in the shape of "nanoflowers" with an average core diameter of about 15 nm [110]. Compared to Ferucarbotran, the MPI raw signal amplitudes normalized to the total iron amount are about 3-fold higher. Different coatings are available, optimized for various applications. In this work, COOH-coating were used, resulting in a total mean hydrodynamic diameter of 30 nm. The COOH-coating results in better cellular uptake performance, which is the main reason why these MNPs were used for the experiments presented in chapter 7.

Chapter 4

MPI hardware and noise characterization

This chapter presents my investigations focusing on objective one, the characterization of the MPI hardware components. Each MPI measurement starts with the excitation and acquisition of the MPI raw signals using electromagnetic coils (see section 3.1). The properties of the hardware used for the field generation and signal acquisition are analyzed in the first section 4.1. The field-generating (transmit, Tx) hardware is mainly checked regarding temporal stability and reproducibility. The hardware for signal acquisition (receive, Rx) is analyzed regarding the frequency-dependence and spatial-dependence of the sensitivity. The second section 4.2 focuses on the characterization of random noise and systematic background components in the MPI raw signals. Empty scanner measurements are performed with adapted field settings to analyze the influence of multiple signal sources. Possible techniques for removing or correcting these signals from the MPI raw signals are presented and discussed. Particular focus is set on the comparison of the conventional dual-purpose TxRx (transmit-receive) and the receive-only (Rx) coils, which were described in detail in section 3.1.3. The results of my investigations presented in this chapter show the importance of considering the influence of the MPI hardware, noise and background signals for a quantitative analysis of MPI data.

4.1 Hardware characterization

MPI hardware components are separated into two categories: field-generation or transmit hardware and signal detection or receive hardware. Transmit hardware includes each component used to produce drive and selection fields. The major requirement for these hardware components is that the generated field amplitudes and gradient strengths are reproducible and stable over time, which is analyzed in section 4.1.1. Receive hardware includes each part used to detect, filter and amplify the MPI raw signal. Since the signals are further processed in the frequency domain, especially the knowledge about the frequency-dependent sensitivity are necessary for a quantitative evaluation. Another important factor is the dependence on spatial position. Section 4.1.2 presents measurement and simulation results concerning these factors. Special interest is given to differences between the conventional TxRx-coils

and the gradiometric Rx-coil installed in the used MPI system (see section 3.1.3). Partial results of this section have been published in HP2.

4.1.1 Transmit hardware

Drive fields

The drive fields generate the magnetic response from MNPs as described in section 2.2.1. They are produced by currents running through three separate coils installed in x-, y- and z-direction (detailed description given in section 3.1). Variations of the field parameters, like the amplitude or the frequency, affect the MPI raw signals. Therefore, the temporal stability are checked by monitoring the currents through the coils during a MPI measurement with nominal drive field amplitudes of $B_x = B_y = B_z = 12\,\mathrm{mT}$. These settings are used for most of the following measurements presented in this work.

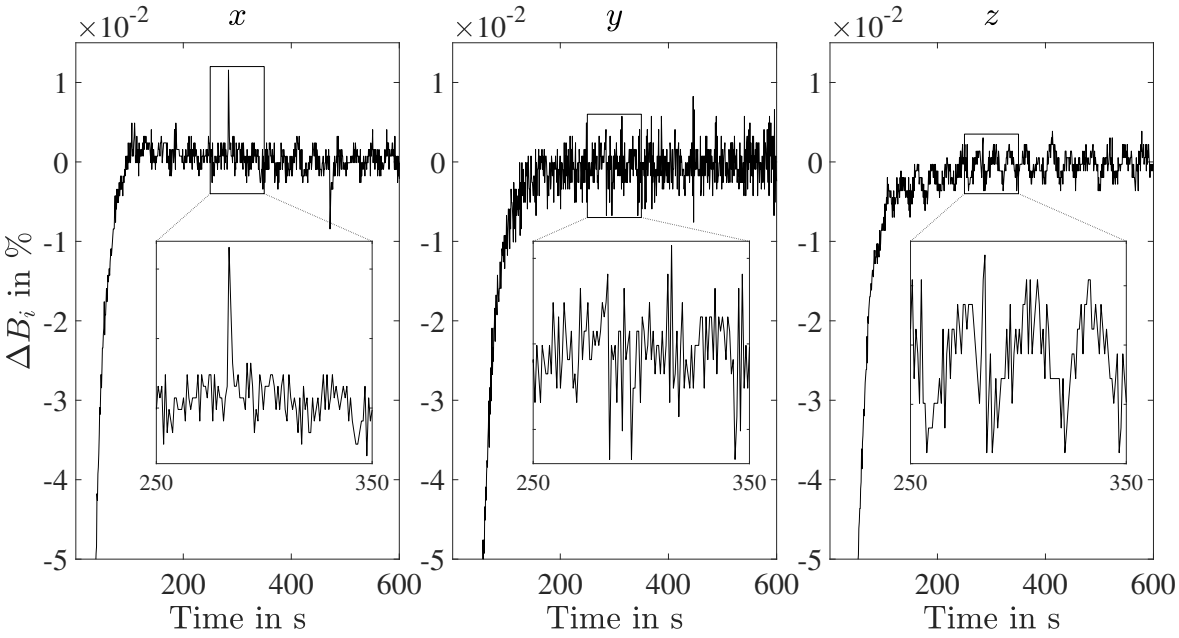

FIGURE 4.1: Relative deviations of drive field amplitudes as a function of time for x-, y- and z-direction. Nominal drive field amplitudes were set to the maximum of $B_i = 12\,\mathrm{mT}$ for x-, y- and z-direction. The strongest deviations up to 1 % are observed during the start of each measurement caused by heating of the coils, which decrease over 90 s. After 90 s, smaller variations of about 0.002 % are observed.

Figure 4.1 shows the relative deviation of the drive field amplitude for x-, y- and z-direction as a function of time. The strongest deviations of about 1 % was detected at the start of each measurement, which decreased during the first 90 s. These large deviations are related to heating of the coils caused by the electrical resistance. After 90 s saturation was reached, showing smaller fluctuations in the range of 0.002 %. A detailed analysis of the influence of the drive field variations on the MPI raw signal is presented in section 4.2.3.

Selection fields

The static magnetic gradient field is generated by an anti-Helmholtz coil pair (see section 3.1) and is needed for spatial encoding (see section 2.2.2). Measurements of the static magnetic gradient field were performed using a Hall-sensor (Teslameter FM 210, radial and axial, Projekt Elektronik Mess- und Regelungstechnik GmbH, Germany). The probe was positioned using a robot at defined locations covering twice the size of the MPI-FOV ($38/38/18\,\mathrm{mm}$ $x/y/z$-direction). Note that no measurement data could be acquired in z-direction for $z > 7\,\mathrm{mm}$ due to geometrical restrictions inside the MPI scanner.

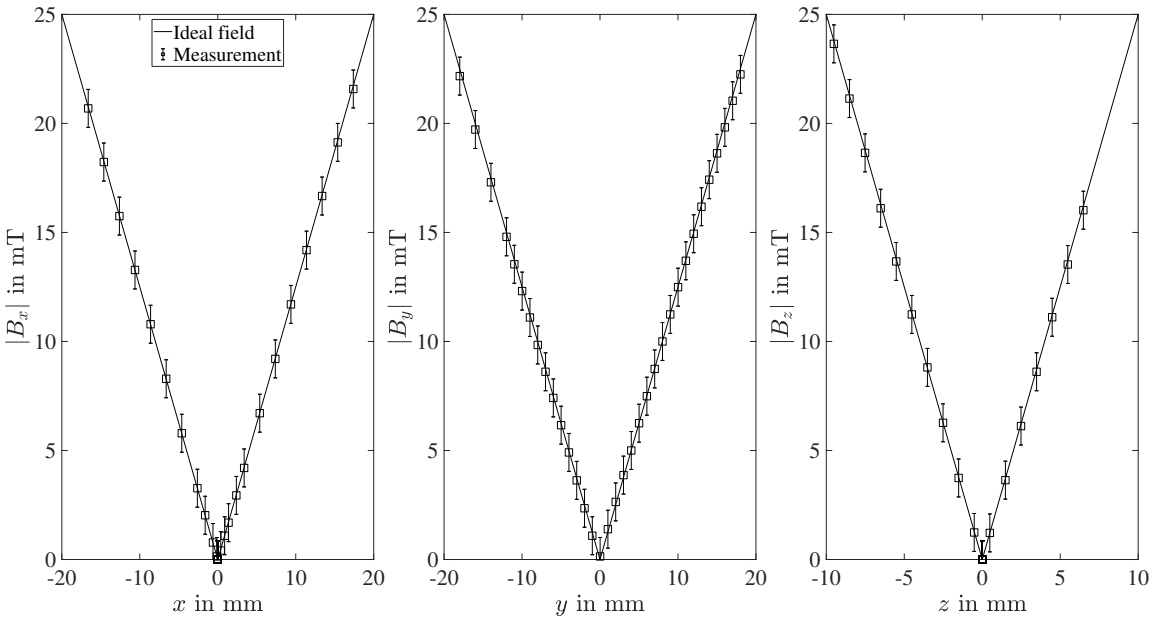

FIGURE 4.2: Measurements of the magnetic fields generated by an anti-Helmholtz coil pair compared to the idealized field conditions for x-, y- and z-direction with gradient strengths of $1.25/1.25/2.5\,\mathrm{T/m}$ respectively. The measurement uncertainty of the Hall-sensor is visualized as error bars. A mean relative difference of 2.1 % or lower was determined between measurements and ideal field conditions by averaging over all data points.

Figure 4.2 displays the measurement results in comparison to the idealized field conditions using the highest gradient strength of $1.25/1.25/2.5\,\mathrm{T/m}$, which was used for most of the MPI measurements presented in this work. No significant temporal drifts of the gradient strength were detected independent of spatial position. Comparing the measurement results with the idealized field conditions, a mean relative difference of $(0.5/1.56/2.1)\,\%$ ($x/y/z$-direction) was determined, which is below the measurement uncertainty of the Hall sensor of $0.9\,\mathrm{mT}$.

4.1.2 Receive hardware

Transfer functions

Three receive coils (x-TxRx, y-TxRx and x-Rx-coil) are installed at the MPI scanner (see section 3.1). The full receive chain consists of multiple hardware components. To identify the influence of these components on the MPI raw signal, a transfer function ρ of the whole receive chain was determined for each coil. For this purpose, a network analyzer (Agilent E5061B ENA, Santa Clara, USA) was used in combination with a small 3-axes coil (Bruker BioSpin, Germany) generating a known reference signal at a certain frequency. The coil was connected to the function generator output of the network analyzer and positioned at the center of the FOV inside the MPI scanner. The induced voltage within each receive coil was recorded, varying the frequency between 10 kHz – 2 MHz, which covers the full range relevant for MPI. The transferred power from the reference coil to the respective receive coil ($S21$) was determined and used as a measure for the receive sensitivity $|\rho|$ (absolute of the transfer function). An optimal sensitivity would therefore be represented by a value of 1 for each frequency.

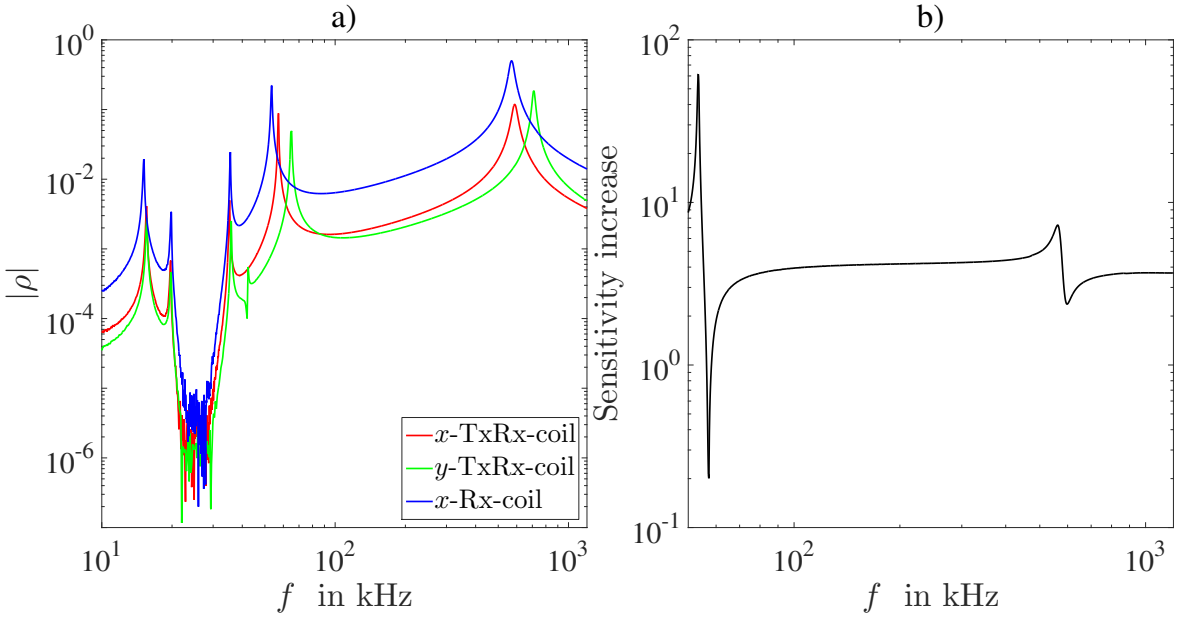

FIGURE 4.3: a) Frequency-dependent transfer functions (unit-less) for the x-TxRx, y-TxRx and x-Rx MPI receive coils measured using the full receive chain and a reference coil positioned at the center of the FOV for signal generation. Frequencies close to 25 kHz are suppressed by band-stop-filters, which also lead to sensitivity peaks for frequencies below 70 kHz due to parasitic resonances. The resonance peak of the whole receive chain is reached around 600 kHz. b) Sensitivity increase of the Rx-coil compared to the x-TxRx-coil. An almost constant increase by a factor of 4 is observed. The variations are mainly caused by different resonance frequencies of the coils.

Figure 4.3a) displays the unit-less, frequency-dependent receive sensitivities for the x-TxRx, y-TxRx and x-Rx-coils. Similar behavior is observed over the whole frequency range for each coil. The band-stop-filters, used to suppress the feed-through of the excitation fields, cause a strong attenuation

of the sensitivity of about 10^{-6} in the frequency range $20-30\,\mathrm{kHz}$. Additionally, these filters result in sensitivity peaks for frequencies below 70 kHz due to parasitic resonances. Above 100 kHz, the sensitives increase until resonance peaks are reached around 600 kHz. The frequency of the resonance peak and the sensitivity peaks caused by the filters differ for each receive coil, mainly influenced by a different inductance of each receive coil.

The sensitivity increase of the *x*-Rx-coil compared to the *x*-TxRx-coil was calculated by dividing the sensitivities of the respective coils and is displayed in figure 4.3b). The frequency region below 40 kHz was neglected due to the strong variations caused by the band-stop-filters. Overall, a mean sensitivity increase by a factor of 4 was achieved using the Rx-coil. The different resonance frequencies and different positions of the sensitivity peaks caused by the filters caused the variance around 600 kHz and 60 kHz. The higher sensitivity of the Rx-coil was achieved by a smaller coil radius ($R = 36\,\mathrm{mm}$) compared to the TxRx-coil ($R = 80\,\mathrm{mm}$) and better noise matching with the low-noise-amplifier (see figure 3.5). Using the sensitivity scaling based on the radius of a solenoid coil derived in [38], an increase by a factor of 3.2 is expected, which is in good agreement with the measured factor of 4.

Spatial sensitivity profile

The sensitivity of the receive coils varies depending on the spatial location. The sensitivity profile of the TxRx-coils and the Rx-coil were determined by finite element simulations (using Ansys Maxwell, Ansys Inc., Canonsburg Pennsylvania). These simulations were performed in cooperation with Bruker Biospin (Ettlingen). A simplified model of the MPI scanner was simulated including the copper shielding taking eddy current effects into account. Ideal conditions were assumed for modeling of the coils, neglecting eddy current effects inside the coils. The generated magnetic field amplitudes were calculated for an frequency of 25 kHz. These magnetic field amplitudes are equivalent to the receive sensitivities according to the law of reciprocity [111].

For validation of the simulations, measurements of the sensitivity were acquired at discrete positions using the same network analyzer and reference coil setup described in section 4.1.2. The band-stop-filters and low-noise-amplifiers were disconnected for the measurement to exclude the influence of these hardware components and to measure the sensitivities at 25 kHz for comparison with the simulations. The reference coil was moved along the central *x*-axis and *y*-axis of the scanner acquiring the sensitivity at each position. No additional measurements along the *z*-axis were necessary due to the radial symmetry of the coils.

Figure 4.4 a) and b) displays central ($z = 0$) slices of the sensitivity profiles for the *x*-TxRx-coil and the *x*-Rx-coil. Due to the large coil diameter of the TxRx-coil in comparison to typical MPI FOVs with sizes of a few centimeters, a homogenous sensitivity profile is achieved around the center of the FOV. The spatial homogeneity of the sensitivity is quantified inside a reference volume defined by a $6\mathrm{x}3\mathrm{x}3\,\mathrm{cm}^3$ cuboid. This volume would be sufficient for most in-vivo rodent studies. Inside this volume, the ratio between maximal and minimal sensitivity was determined to be 14 %, which is used as a measure for spatial homogeneity of the sensitivity. A similar homogenous sensitivity is achieved

by the other TxRx-coils. The sensitivity profile of the Rx-coil shows greater variations compared to the TxRx-coil due to the smaller coil size. However, inside the MPI-relevant volume, a maximal deviation of 15 % is calculated. Therefore, no degradations in terms of homogeneity are present by implementing the Rx-coil for most MPI applications.

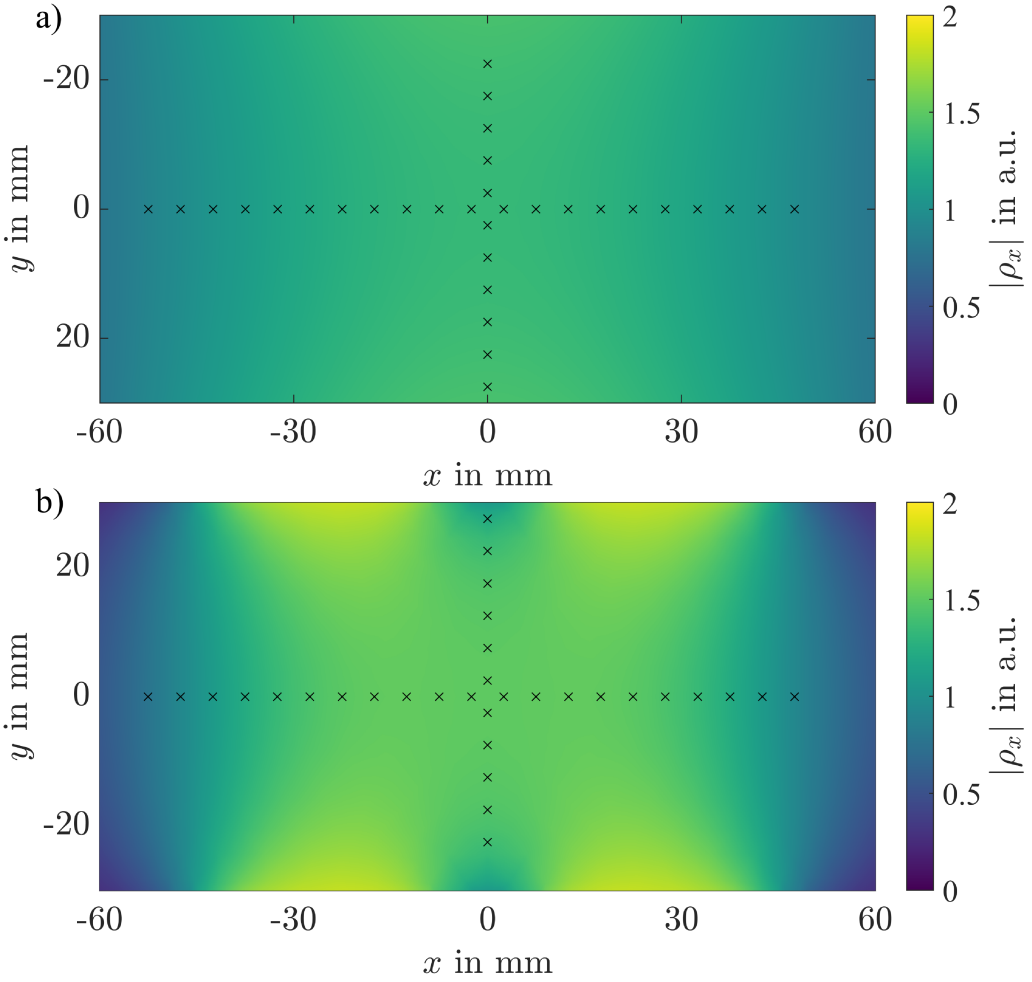

FIGURE 4.4: Simulated sensitivity profiles of a central slice ($z = 0$) for the x-TxRx-coil (a) and the x-Rx-coil (b). A homogenous sensitivity is achieved by both coils at the center of the coils. The black crosses mark the positions of the reference coil used for comparisons with measurement data, which is displayed in figure 4.5.

Figure 4.5 a) and b) display central line plots along the x- and y-axis of the simulations in comparison to measured values. Qualitatively, measurement data and simulations show the same behavior. For a quantitative comparison, the measurement data were normalized to the maximal sensitivity of the simulations. This allowed to extract a mean relative deviation between measurements and simulation of 0.5 % for both, the x-TxRx and x-Rx-coils.

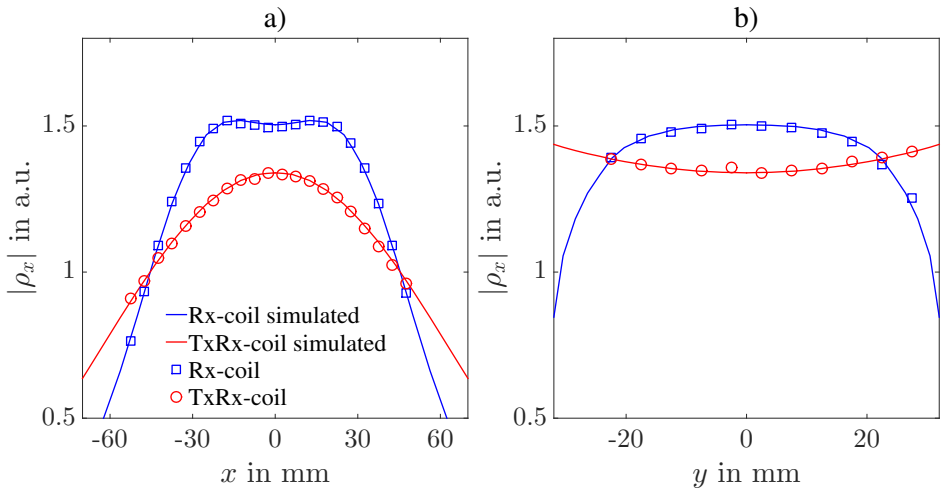

FIGURE 4.5: Comparison of measurements and simulations of the sensitivity profiles of the x-TxRx and x-Rx-coils along the x-axis (a) and y-axis (b). The measurement data were normalized to the maximal sensitivity of the simulation. Measurement data and simulations are in good agreement with a mean relative deviation of 0.5 %.

4.2 MPI noise characterization

The measured MPI raw signal not only contains contributions caused by the response of MNPs. A phenomenological model including additional signal sources is given by:

$$\hat{u} = \hat{u}^{\mathrm{MNP}} + \hat{u}^{\mathrm{N}} + \hat{u}^{\mathrm{BG}} + \hat{u}^{\mathrm{T}} \tag{4.1}$$

$\hat{u}^{\mathrm{MNP}}$ is the signal generated by MNPs. $\hat{u}^{\mathrm{N}}$ describes signals originating from random processes (white noise, pink noise, quantization noise, etc.). $\hat{u}^{\mathrm{BG}}$ is caused by systematic background signals (scanner hardware components, external radiation, etc.). An additional term ($\hat{u}^{\mathrm{T}}$) is added to describe phenomenological observed transient signals or distortions, leading to a sudden change of the MPI raw signals. The identification of signal components generated by MNPs requires that the influence of each other signal source is known, which is the focus of this section.

Multiple MPI-specific methods for removal of noise and background signals have been proposed in the last years [112, 113]. A straightforward approach consists of the subtraction of an empty scanner measurement ($\hat{u}^{\mathrm{MNP}} = 0$) from the actual measurement data. However, this method only removes signal components, which are constant over the acquisition time. Temporal variations, drifts and sudden changes caused by distortions are not corrected and lead to remaining contributions to the MPI raw signal, which could be misinterpreted as MNP signals. Advanced methods include interpolation using the data of multiple empty scanner measurements over time, extension of the SF-based image reconstruction or modified imaging sequences [114–117]. For each of these methods the precise knowledge of the different signal components and their temporal variation is crucial.

In this section the dominant causes for noise and distortions are identified and characterized by inspecting measurements of the empty scanner. The measurement data are converted into magnetic moments using the calibration technique presented in the next section 5.1. Each frequency component of the MPI raw signal is analyzed for each of the three receive coils individually. For simplicity and to quantify the mean influence of each noise component, a single parameter is extracted from each individual MPI raw signal data set. This parameter is defined by the mean signal amplitude over certain MPI-relevant frequency components:

$$\overline{u}_{\mathrm{MPI}} = \sum_{n=1}^{N} \frac{1}{N} |\hat{u}(f_n)| \tag{4.2}$$

n is defined as the index of MPI-relevant signal components, given by each frequency component (f_n) with a mixing order below 20, for which the strongest MNP response is expected (see section 2.2). Frequency components below $f_n < 60\,\mathrm{kHz}$ are neglected due to the strong variations caused by the receive chain (see section 4.1.2). Note that the quantitative results might differ for certain frequency components, but qualitative similar behavior was observed for each frequency component.

4.2.1 Random noise

The term $\hat{u}^{\mathrm{N}}$ of equation 4.1 describes signal contributions generated by random processes (noise). The differentiation between signals generated by random noise or systematic noise is challenging. However, in MPI, major background signals are generated by the hardware itself [41]. By turning off the drive and gradient fields, one can minimize the acquisition of these systematic signals to estimate the signals generated by random noise.

Characterization of random noise

MPI raw measurement data were acquired measuring the empty scanner with drive and selection fields turned off. Figure 4.6 displays the amplitude (a) and phase (b) of averaged ($N = 1000$) MPI raw data sets for the x-TxRx, y-TxRx and x-Rx-coils respectively. Similar qualitative behavior is observed for each receive coil. No coherent phase information of the complex MPI raw signal was detected for the whole frequency range, indicating that the detected signal components were generated by random processes. Above 80 kHz a so-called pink noise characteristic, following a $1/f$-function, is observed for the signal amplitudes with maximal signal amplitudes of about $10\,\mathrm{pAm}^2$. Similar behavior has been reported in [118, 119]. This underlines the assumption that the acquired signals were generated by random processes.

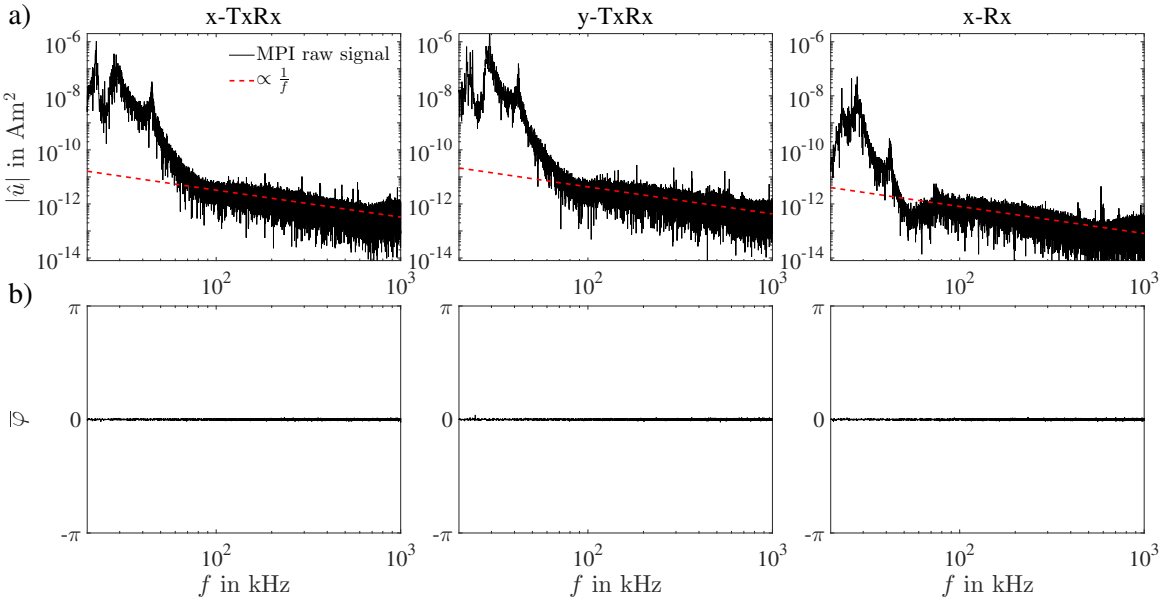

FIGURE 4.6: a) MPI raw data amplitude spectrum acquired with drive and selection fields turned off using the x-TxRx, y-TxRx and x-Rx-coils (1000 averaged measurement repetitions). The data were converted into magnetic moments using the calibration technique presented in section 5.1. For visualization of the pink noise characteristic, a $1/f$-function was fitted to the data. Below 80 kHz deviations from the $1/f$-characteristic are observed based on distortions caused by the resonant circuits used to produce the drive fields. b) Averaged phase spectrum, determined by averaging over 1000 independent measurements. No coherent phase information is observed.

Below 80 kHz, strong deviations from the $1/f$-characteristic were detected, with amplitudes up to about 2 µAm^2. These distortions were likely caused by the resonant circuits of the transmission chain used to generate the drive fields. Although no fields were generated in these measurements, the sensitivity of these resonant circuits is much higher in the frequency region around 25 kHz compared to higher frequencies, leading to a stronger acquisition of distortions and increased signal amplitudes.

Removal of random noise

A complete removal of $\hat{u}^{\mathrm{N}}$ for a measured MPI data set is not possible due to the random nature of the signals. The influence of random noise is minimized by increasing the number of averages. Figure 4.7 displays $\overline{u}_{\mathrm{MPI}}$ acquired for the x-TxRx, y-TxRx and x-Rx-coils dependent on the number of averaged measurement repetitions N. A signal decrease proportional to $\frac{1}{\sqrt{N}}$ was determined for each receive coil, agreeing with the assumption that the signals were generated by random noise. The two TxRx-coils show similar behavior with slightly lower signal amplitudes for the x-TxRx-coil due to the smaller coil diameter. The mean MPI signal amplitudes detected by the Rx-coil are lower compared to the TxRx-coils due to the smaller coil size and the gradiometric design, attenuating external random signal sources. The influence of the remaining random noise is further minimized by regularization techniques used in the image reconstruction process (see section 6.1.2).

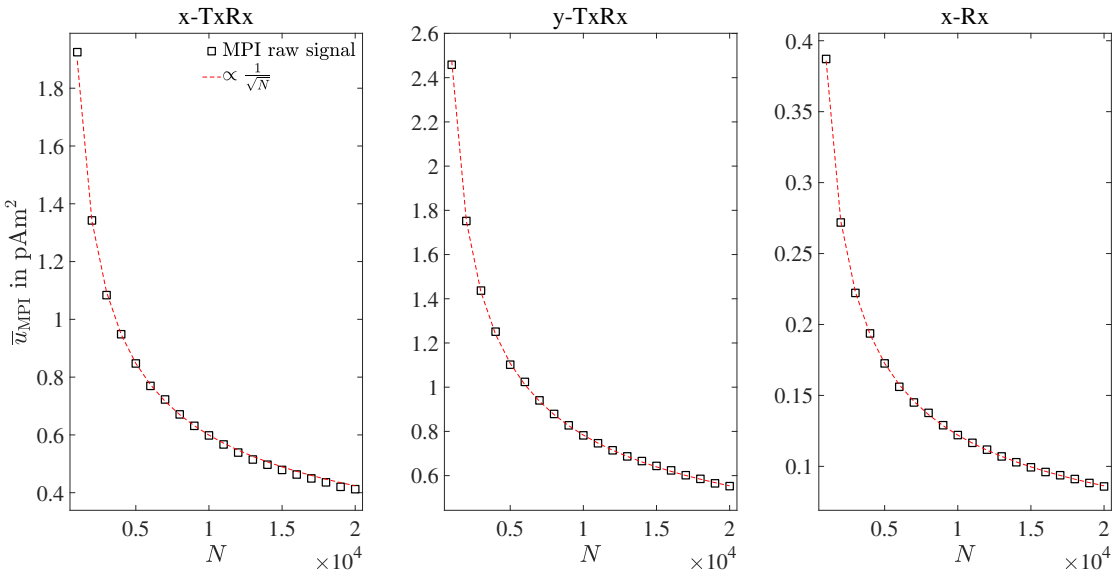

FIGURE 4.7: $\overline{u}_{\mathrm{MPI}}$ acquired for the x-TxRx, y-TxRx and x-Rx-coil with a varying amount of averaged measurement repetitions N. The signal strength decreases proportional to $\frac{1}{\sqrt{N}}$ and is correlated to the diameter of the respective coil.

4.2.2 Background signals

Systematic background signals are caused by signal sources other than MNPs. This includes electromagnetic radiation of external devices, possible contamination of the scanner bore and the magnetic fields generated by the MPI device itself. External electromagnetic fields are minimized by the shielded environment of the scanner and no static systematic background signal contributions have been detected in the measurements presented in the previous section 4.2.1. Sudden changes caused by transient signals or other fast changing external distortions are considered separately in section 4.2.4. This section focuses on the characterization of the influence of background signals generated by the magnetic fields needed for MPI signal excitation.

Influence of drive and gradient fields

Measurements of the empty scanner were performed, in which the gradient and drive fields were turned on in succession to analyze the qualitative and quantitative influence on the MPI raw signals. To minimize the effects caused by random noise, 1000 independent measurement repetitions were averaged. Figure 4.8 displays the qualitative influence of drive and gradient fields on the amplitude and phase spectra of the complex MPI raw signal. Shown are the data acquired with the x-TxRx-coil. Similar qualitative behavior is observed using the other coils. The data visualized in figure 4.8 a) and c) were acquired using the highest gradient strength of $2.5\,\mathrm{T/m}$ and no drive fields. No significant

qualitative influence of the gradient strength on the amplitude and phase spectra is observed compared to the contributions caused by random noise, discussed before.

Figure 4.8b) and d) display the amplitude and phase spectra acquired with the maximal drive field amplitudes of 12 mT for x-, y- and z-direction. Strong additional signal components were acquired at frequency components generated by mixing of the three fundamental excitation frequencies with amplitudes up to hundreds nAm^2, which represents an up to 10^5-fold higher signal amplitude compared to components generated by random noise. A coherent phase information at these frequency components support the assumption that these signals were generated by non-random processes. The strongest signal contributions and signal variations were determined around the odd harmonic frequency components with an overall decrease for higher mixing orders (see section 2.2). These background signals were caused by non-linear behavior of hardware components in the signal transmission and receive chains, most likely induced by power-amplifiers. Although filters are used to minimize these effects, parts of the drive fields are still detected during an MPI measurement.

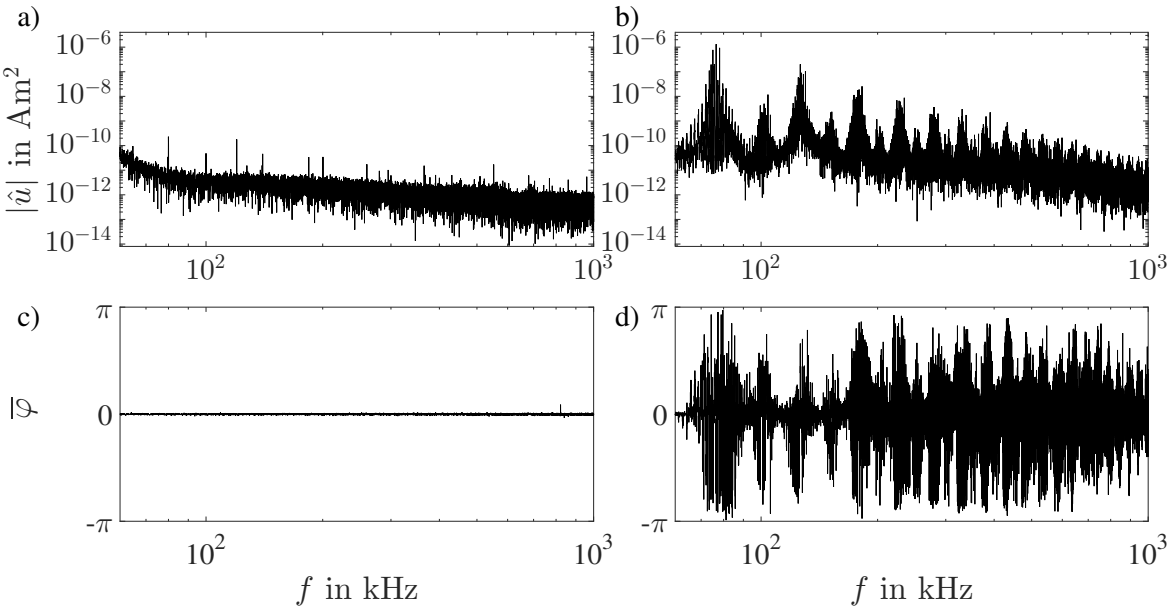

FIGURE 4.8: MPI raw data amplitude (a,b) and phase (c,d) spectra acquired from empty scanner measurements. Presented are data averaged over 1000 independent measurement repetitions. a) and c) were acquired with maximal gradient strength of $G_z = 2.5\,\mathrm{T/m}$. No significant differences compared to measurements without a gradient are observed. b) and d) were acquired with maximal drive field amplitude of $B_i = 12\,\mathrm{mT}$. Strong background signal contributions for mixed frequency components of the excitation frequencies are observed with high amplitudes and a coherent phase.

Figure 4.9 displays the quantitative influence of the gradient strength and drive field amplitudes on $\overline{u}_{\mathrm{MPI}}$. The gradient field showed no significant quantitative influence on the signals acquired with the x-TxRx and x-Rx-coil. A small increase of up to $(83.6 \pm 0.1)\,\mathrm{pAm^2}$ was determined for the y-TxRx-coil for a gradient strength of $2.5\,\mathrm{T/m}$. This small offset could be related to the closer proximity of the y-TxRx-coil to the gradient coils and therefore a stronger heat transfer.

A much stronger signal increase was detected correlated to the drive field amplitudes. Especially for the x-TxRx and y-TxRx-coils, a mean signal increase of up to $(2.7 \pm 0.1)\,\mathrm{nAm}^2$ and $(1.4 \pm 0.1)\,\mathrm{nAm}^2$ (mean$\pm$std) for the maximal drive field amplitudes of 12 mT were determined respectively.

Similar, qualitative behavior is observed for the signal detected using the x-Rx-coil. Ideally, the influence of the excitation fields would be canceled out completely by the gradiometric design. Due to imperfect removal of these fields, caused by the positioning of the cancelation-coil parts, signal amplitudes up to a maximum of $(40.0 \pm 0.1)\,\mathrm{pAm}^2$ were detected. Another possibility for the remaining signals detected with the x-Rx-coil, would be small magnetic contamination of the material of the MPI scanner, which are not attenuated by the gradiometric design. Comparing the background signals acquired with x-TxRx-coil and x-Rx-coil, a mean attenuation of up to a factor of (65.5 ± 1.8) was determined. This factors represents the mean attenuation determined by $\overline{u}_{\mathrm{MPI}}$ and differs for individual frequency components.

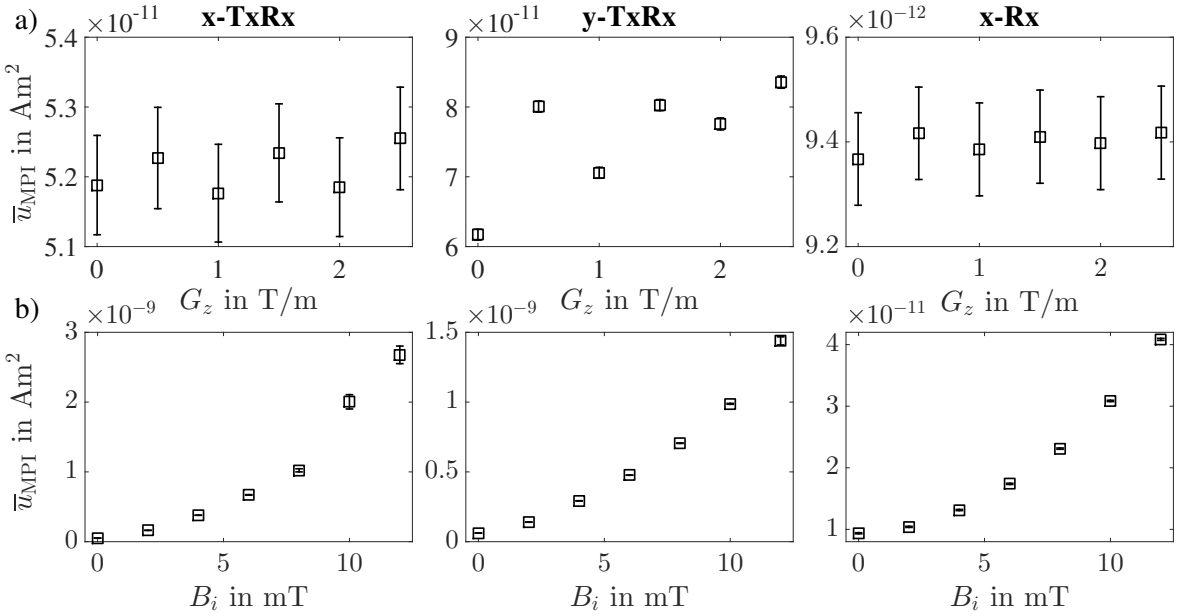

FIGURE 4.9: $\overline{u}_{\mathrm{MPI}}$ determined from data acquired measuring the empty scanner using different gradient strengths G_z (a) or drive field amplitudes $B_i = B_x = B_y = B_z$ (b). Each data point represents the mean value of 1000 independent measurements with the standard deviation visualized as error bars. The gradient strength shows only minor influence on $\overline{u}_{\mathrm{MPI}}$. A strong dependency of $\overline{u}_{\mathrm{MPI}}$ with drive field amplitude is observed, especially for the TxRx coils.

Due to the systematic origin of background signals, they can be excluded from the measurement data by performing appropriate reference measurements. However, this requires the knowledge of the temporal variations of these kind of signals, which is analyzed in the following section.

4.2.3 Signal stability analysis

The previous section showed that major signal contributions are caused by hardware components of the MPI scanner. The removal of these contributions is necessary to clearly identify signals generated

by MNPs. For this purpose, measurements of the empty scanner are performed and subtracted from subsequent measurements. However, this approach assumes that the background signals are stationary over the whole acquisition time. If the signals vary over time, these changes have to be included in the background correction method.

In the following, the temporal variations of the background signals are analyzed. Three different time regimes are investigated: the short-term regime in the range of seconds up to minutes (variations during a single MPI measurement), the mid-term regime in the range of hours (variations in between MPI measurements and during SF acquisitions) and the long-term regime in the range of months up to years (variation of the whole scanner performance).

Short-term stability (seconds-minutes)

The signal variations in the short-term regime are analyzed based on measurements of the empty scanner acquired with maximal drive field amplitudes (12/12/12 mT) and gradient strengths (1.25/1.25/2.5 T/m). Single repetitions were acquired over a total acquisition time of 10 min (30000 repetitions). This was repeated to obtain 100 individual data sets.

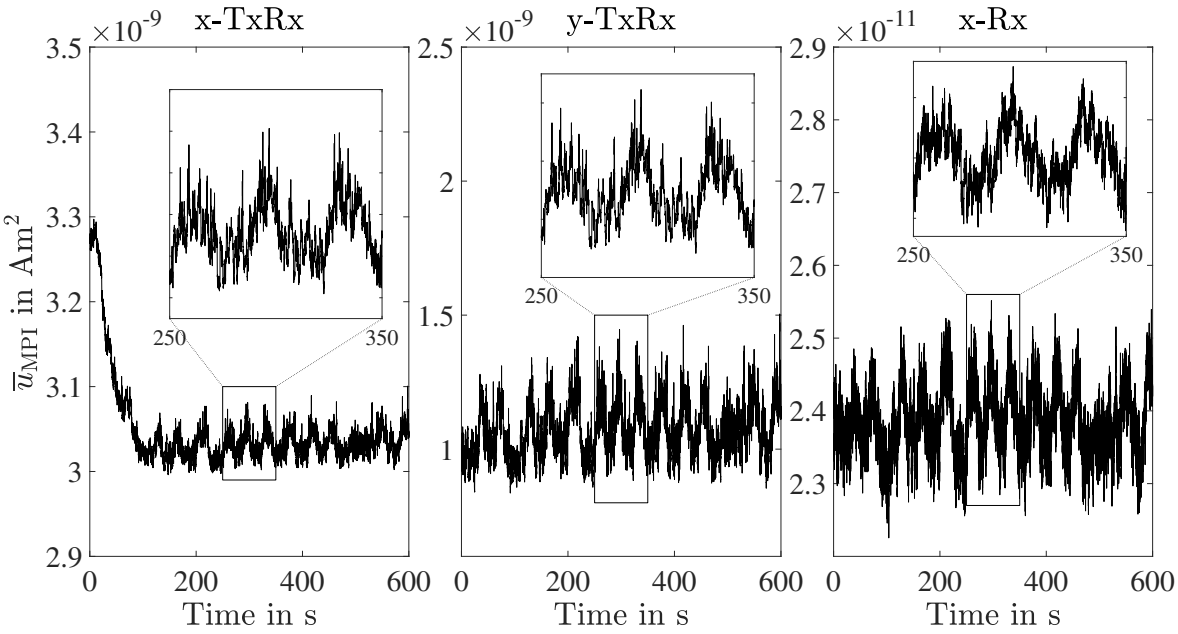

FIGURE 4.10: $\overline{u}_{\mathrm{MPI}}$ acquired from empty scanner measurements as a function of time using the x-TxRx, y-TxRx and x-Rx-coil respectively. Displayed are 30000 single repetition measurements acquired over a total acquisition time of about 10 min. The strongest variations are observed during the first 90 s for the x-TxRx-coil caused by heating of the coils.

Figure 4.10 displays $\overline{u}_{\mathrm{MPI}}$ as a function of time for one representative data set. Qualitative similar behavior is observed in the other data sets. A continuous drift during the first 90 s was detected for the data acquired with the x-TxRx-coil, changing the measured amplitude by about 250 pAm^2. Similar, less

pronounced drifts are observed in certain frequency components acquired with the y-TxRx and x-Rx-coils, but are not visible for $\overline{u}_{\mathrm{MPI}}$. After 90 s an almost constant signal level was reached with smaller signal fluctuations, quantified by the standard deviations of $(13.2 \pm 1.3)\,\mathrm{pAm}^2$, $(83.5 \pm 6.9)\,\mathrm{pAm}^2$ and $(0.4 \pm 0.1)\,\mathrm{pAm}^2$ (mean$\pm$std of 100 individual data sets) for the x-TxRx, y-TxRx and x-Rx-coil respectively. Note that the saturated MPI signal level, reached after the first 90 s was not constant for each measurement and is further analyzed in section 4.2.3. The observed effects are caused by variations of drive field amplitudes, which were described in section 4.1.1. The strong drifts at the start of each measurement are caused by heating of the coils and deviations of the drive field amplitudes of up to 1 %. The remaining signal fluctuations are likely caused by the smaller variations of the drive field amplitudes of about 0.002 %.

Mid-term stability (minutes-hours)

The short-term analysis revealed that an almost constant signal level is reached after an initial heating period during the first 90 s of each measurement. In the following it is investigated if this signal level itself changes over the course of hours. For this purpose, measurement data were acquired over a total acquisition time of 12 h, which represents a typical acquisition time of a SF. Data averaging was performed in 10 min-blocks (30000 measurement repetitions), calculating the mean and standard deviation of $\overline{u}_{\mathrm{MPI}}$, which are visualized as a function of time in figure 4.11. Note that the data acquired during the first 90 s of each measurement were truncated due to the initial heating effects described in section 4.2.3.

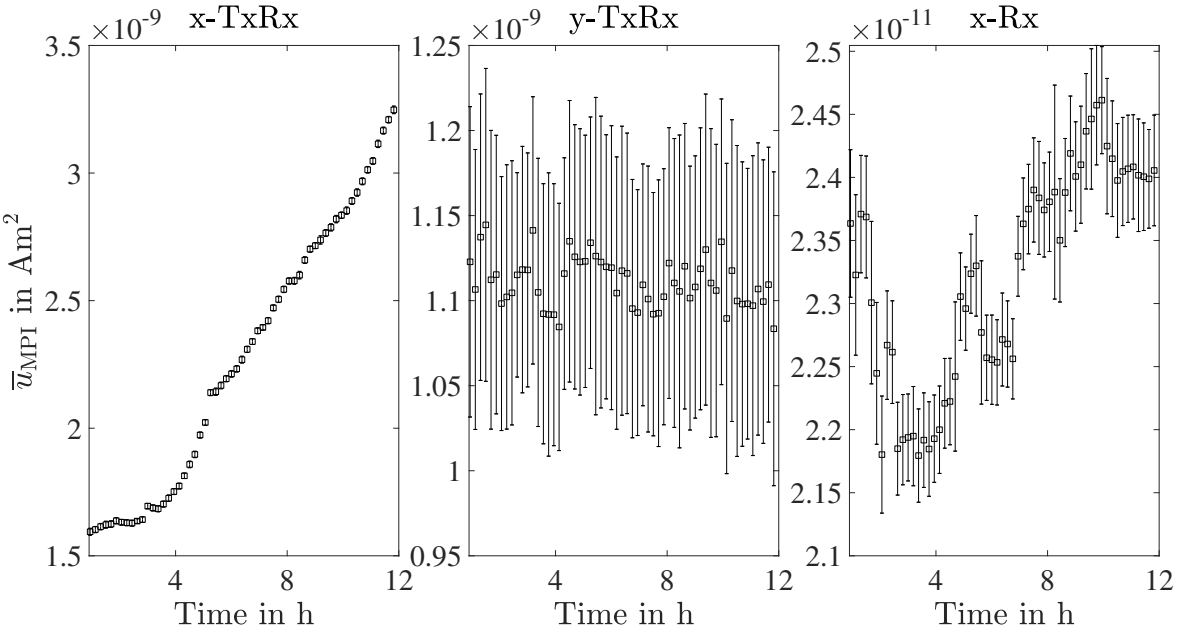

FIGURE 4.11: Variations of $\overline{u}_{\mathrm{MPI}}$ acquired from empty scanner measurements as a function of time. Displayed are averaged values (30000 measurement repetitions) with the standard deviation visualized as error bars. The signal changes over the course of hours are likely caused by thermal drifts of the MPI hardware components.

The data acquired with the x-TxRx-coil show strong signal drifts over 12 h, with changes up to 1.6 nAm^2. The data acquired with the y-TxRx and x-Rx-coils show similar qualitative behavior for certain frequency components but overall lower signal variations in the range of 0.2 nAm^2 and 35 pAm^2 respectively. These signal variations are likely caused by thermal drifts of hardware components e.g. the low-noise amplifiers in the receive chain. The standard deviation of $\overline{u}_{\mathrm{MPI}}$ stays constant over time (as described in section 4.2.3). Therefore, the detected drifts can be described as an "offset" for the signal amplitude, which can be corrected with appropriate reference measurements.

Long-term stability (days-months)

Finally, the signal variations as a function of time are analyzed for the last 3 years. The aim is to investigate, how environmental conditions (temperature, humidity, external distortions, etc.) influence the MPI background signals. Additionally, this information allows monitoring of the performance of hardware components to identify possible wear, damage or contamination.

The data used for this analysis were extracted from SF acquisitions, in which measurements of the empty scanner are performed at regular intervals. In general, these data are used for background signal correction. For each new particle type or change of the measurement parameters, a new SF has to be acquired. Over the last three years, a total of 122 individual SF acquisitions were measured using the same parameters (see table 4.1). Each individual data set consists of 500-5500 measurements of the empty scanner depending of the SF settings, acquired over a time span between 3-41 hours. $\overline{u}_{\mathrm{MPI}}$ was determined by averaging over the total acquisition time for each SF data set.

TABLE 4.1: Measurement parameters used to filter the SF data base.

Parameter	**Value**
Drive field amplitudes $x/y/z$ in mT	$12/12/12$
Gradient strength $x/y/z$ in T/m	$1.25/1.25/2.5$
Receiver Bandwidth in MHz	$1.25 \cdot 10^6$
Averages	100
Minimal acquisition time	>3 h

Figure 4.12 displys $\overline{u}_{\mathrm{MPI}}$ as a function of the acquisition date. In the time between January 2017 and February 2018, only small signal variations between (0.46 ± 0.03) nAm^2 and (0.58 ± 0.03) nAm^2 (mean$\pm$std) were detected using the x-TxRx and y-TxRx-coils. Starting from February 2018, much stronger signal variations were detected. Ten-fold or five-fold higher signal amplitudes were detected by the x-TxRx and y-TxRx-coils respectively, also showing higher standard deviations (visualized as error bars). The signals detected with the x-Rx-coil showed only minor variations over the last three years with a mean signal amplitude of (13.3 ± 3.5) pAm^2 (mean$\pm$std).

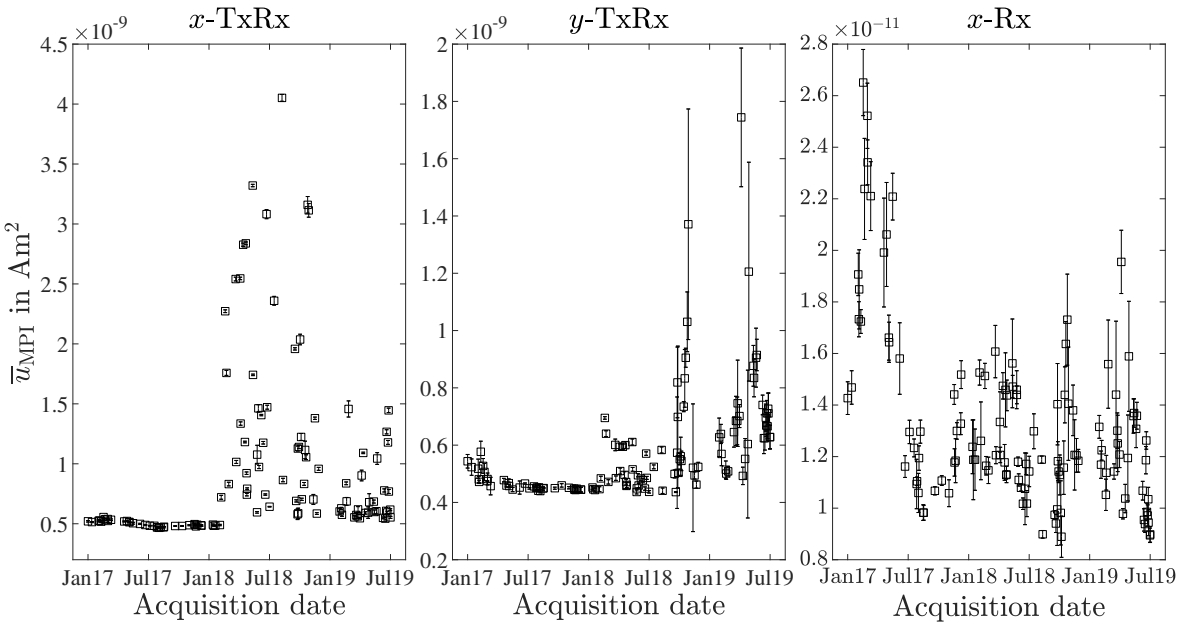

FIGURE 4.12: $\overline{u}_{\mathrm{MPI}}$ acquired from empty scanner measurements as a function of the measurement date using the x-TxRx, y-TxRx and x-Rx-coil respectively. Displayed are averaged values over the time span of a complete SF acquisition with the standard deviations visualized as error bars. Starting from February 2018, increased signal amplitudes were detected for the x-TxRx and y-TxRx-coils.

The increased background signal contributions, starting in February 2018, were only detected in the two TxRx-coils. Possible explanations for these changes include damage or wear of hardware components. Since no changes were detected using the x-Rx-coil, magnetic contamination or changes in the magnetic field settings can be excluded from the possible causes. Another possible explanation could be related to external radiation caused by changes in the environment e.g. new devices in the clinical environment around the MPI scanner, which would be attenuated by the gradiometric design of the x-Rx-coil.

Removal of background signals

Due to the systematic origin of the measured background signals, they can not be completely removed by averaging over multiple measurement repetitions. A straightforward way for removing these kind of signals is by performing empty scanner measurements, which are subtracted from subsequent measurements. For empty scanner measurements, ideally only the random noise components remain after background correction (see section 4.2.1). This requires that background signals are stationary, which is not the case for MPI as it was demonstrated in the previous sections. In the following, the influence of these temporal variations on the background correction method is discussed. Background correction was performed by subtracting two averaged measurements separated by the time τ:

$$\hat{u}_{corr} = \hat{u}_t - \hat{u}_{t+\tau} \tag{4.3}$$

τ needs to be chosen as short as possible, to minimize the effects observed in the mid- and long-term regime. Empty scanner measurements were acquired using drive field amplitudes of $12/12/12\,\mathrm{mT}$ and gradient strengths of $1.25/1.25/2.5\,\mathrm{T/m}$. 1000 measurement repetitions were averaged to minimize the influence of random noise. Two averaged data sets were subtracted from each other, which were acquired with a time gap of $\tau = 1\,\mathrm{min}$.

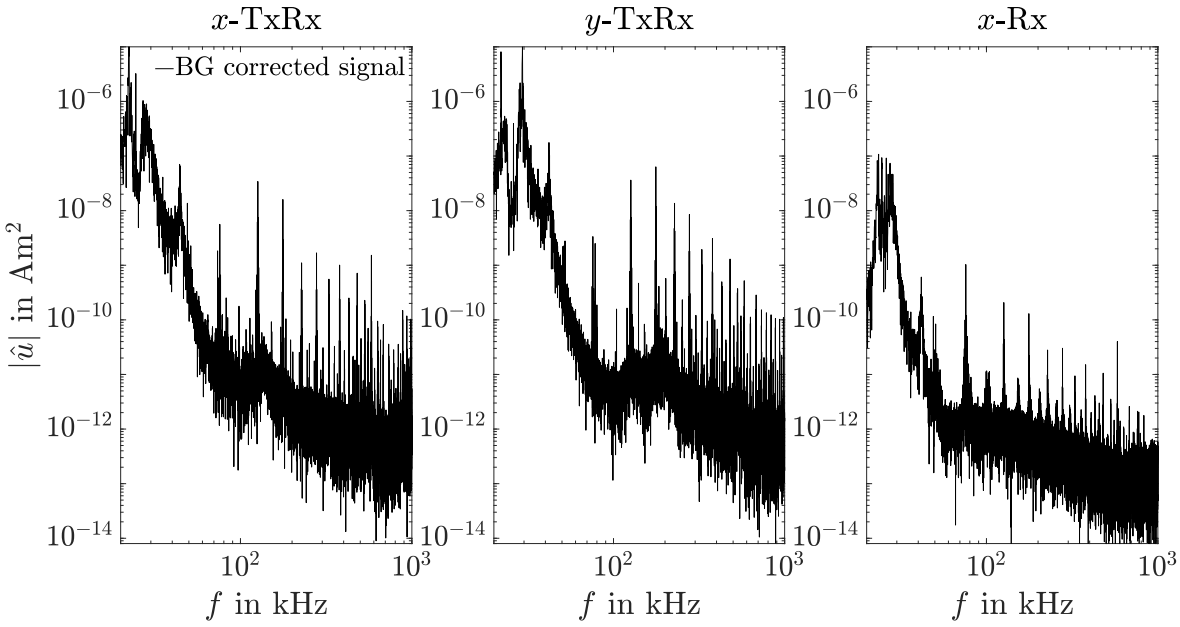

FIGURE 4.13: Background corrected MPI signal amplitudes acquired from empty scanner measurement. Background correction was performed by subtraction of two averaged measurements (1000 individual measurement repetitions) with a time gap $\tau = 1\,\mathrm{min}$. The background signals generated by the drive fields are attenuated but not completely removed due to variations of the signals in the short-term regime.

Figure 4.13 displays the background corrected MPI raw signals for the x-TxRx, y-TxRx and x-Rx-coil respectively. The detected background signals, generated by the drive fields, were attenuated by factors up to 10^4 but a complete removal was not achieved. A quantitative analysis of the remaining signal contribution after background correction was performed by calculating $\overline{u}_{\mathrm{MPI}}$, which were determined to be $(22.3 \pm 11.0)\,\mathrm{pAm^2}$, $(88.7 \pm 46.9)\,\mathrm{pAm^2}$ and $(1.2 \pm 0.3)\,\mathrm{pAm^2}$ (mean$\pm$std of 100 individual data sets) for the x-TxRx, y-TxRx and x-Rx-coil respectively. The determined mean amplitudes are still up to 30-fold higher compared to the contributions generated by random noise. Especially frequency components generated by low mixing orders show strong remaining signal contributions. The main cause for these uncorrected signals are the variations in the short-term regime generated by small drive field amplitude fluctuations described in section 4.2.3. These remaining signals after background correction need to be taken into account when calculating the signal to noise ratio (see section 5.1) since they contribute to the blank signal of a measurement.

4.2.4 Transient signals

The last term of equation 4.1 $\hat{u}^{\mathrm{T}}$ describes abrupt signal changes, called transient signals, which was added based on phenomenological observations. Figure 4.14a) displays an example, for the occurrence of a transient detected during an MPI measurement. Presented is the amplitude of a single frequency component measured as a function of time. An abrupt signal increase was detected after 120 s and a subsequent decrease after additional 40 s. These sudden changes of the signal amplitudes could be related to a discharge of a hardware component, or could be produced by external signal sources but the exact causes for these changes are not known. The removal of these transient signals can be performed similar as described for systematic background signals (see section 4.2.3) or by excluding single frequency components from the further signal processing. However, the random occurrence of these signals complicate the clear identification and hence the removal of these signal contributions. In the following, a technique for the identification of transient signals is described and used to obtain statistics about the occurrence of these distortions.

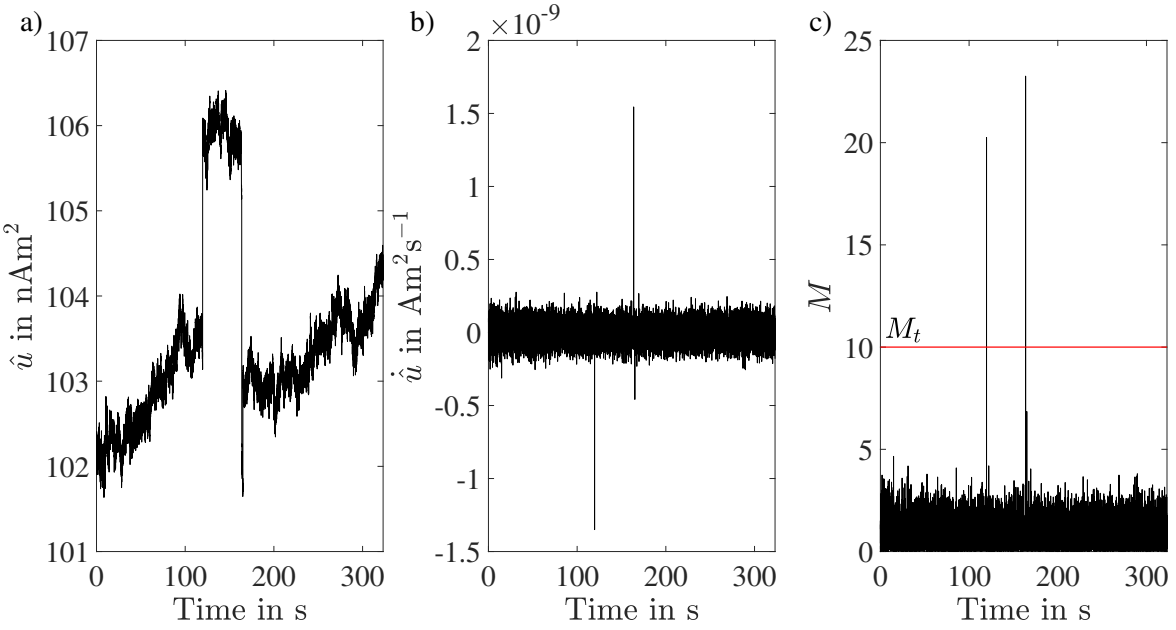

FIGURE 4.14: a) MPI raw signal amplitude of a single frequency component measured over time, showing the effects of the detection of a transient signal. b) Time derivative of the amplitude presented in a). M calculated for each time point (see definition 4.4), which allows to identify the occurrence of a transient signal by defining an appropriate threshold M_t.

Based on the phenomenological observation that transient signals lead to a sudden change of signal amplitude, the time derivative of the signal ($\frac{\partial}{\partial t}\hat{u} = \dot{\hat{u}}$) is calculated. Figure 4.14b) displays the time derivative for the previously described example. The start and end point of the transient signal can clearly be identified. An outlier-detection algorithm was used to automatically identify these points by calculating the M-parameter for each time point [120]:

$$M = \frac{\dot{\hat{u}} - \mathrm{MED}}{\mathrm{MAD}} \tag{4.4}$$

With the median (MED) and the median absolute deviation (MAD). Based on a phenomenological chosen threshold parameter of $M_t \geq 10$, sudden changes of the signal amplitudes are detected (see figure 4.14).

This algorithm was used to determine the probability for the occurrence of transient signals in MPI measurements. For this purpose, single repetitions were acquired over a total acquisition time of 24 h, measuring the empty scanner. Each frequency component was analyzed individually using the described method to identify transient signals. A probability for the occurrence of a transient signal in a single repetition was determined based on the number of detected transients (n_d) and the total number of measurement repetitions (N):

$$p_\mathrm{d} = \frac{n_\mathrm{d}}{N} \tag{4.5}$$

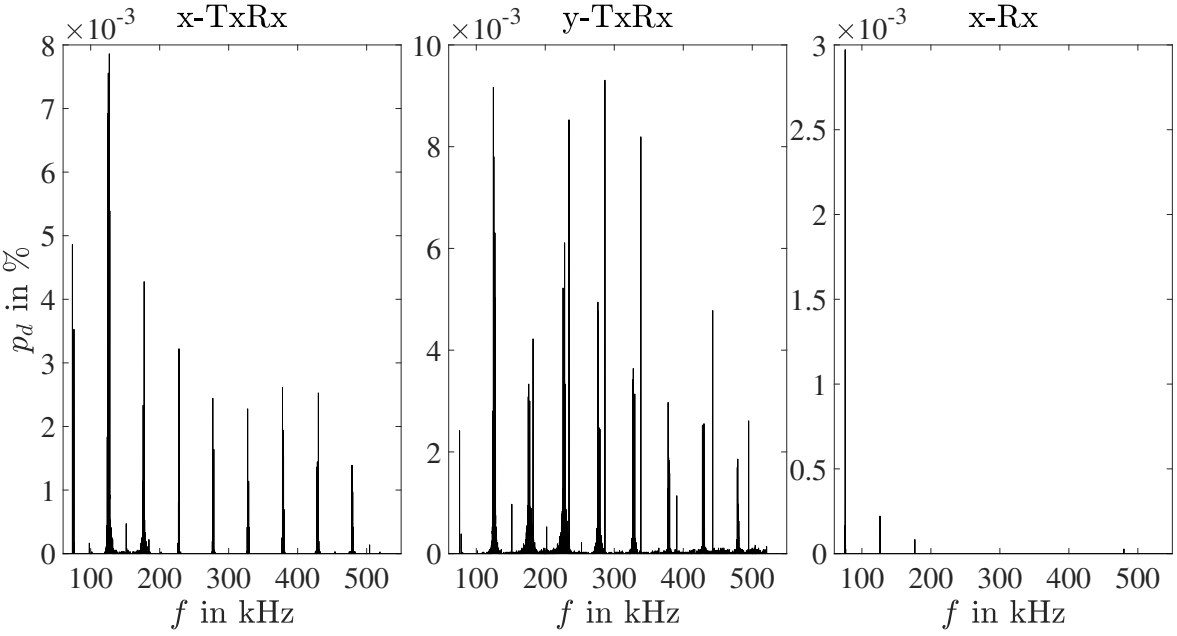

FIGURE 4.15: Probability for the occurrence of transient signals during a single repetition for each receive coil (see definition 4.5). High probabilities are mainly observed for frequency components at low mixing orders and the TxRx-coils, which indicate that the occurrence of these transients are related to the drive fields.

Figure 4.15 displays the probabilities for each frequency component of the x-TxRx, y-TxRx and x-Rx-coils. The highest probabilities are detected for frequency components of low mixing orders, in which also the highest background signal contributions caused by the excitation fields were observed (see section 4.2.2). Therefore, it is assumed that the measured transient signals are correlated to changes of the excitation fields. This would also explain, why much lower probabilities of transient

signals were determined for the x-Rx-coil compared to the TxRx-coils, as the Rx-coil provides a stronger attenuation of background signals based on the gradiometric design. The overall probability for the detection of a transient signal in any frequency component in a single measurement repetition was determined to be 0.24 %, 0.59 % and 0.004 % for the x-TxRx, y-TxRx and x-Rx-coil respectively. This yields probabilities of 90.9 %, 99.7 % and 3.9 % for detecting at least one distortion in 1000 measurement repetitions. These probabilities were determined using data acquired by performing continuous measurements for 24 h and might differ for shorter acquisition times.

4.3 MPI hardware and noise: Summary and discussion

The objective of this chapter was to characterize the MPI hardware and analyze its influence on the MPI raw signals. The hardware necessary for generating the drive and selection fields were checked for deviations from the nominal values. The gradient fields showed no significant deviations and were stable over time. The drive field amplitudes showed strong variations of up to 1 % during the start of each measurement related to heating of the coils and smaller variations around 0.002 % after the first 90 s. Based on this knowledge, preheating was performed before data acquisition was started for each following MPI measurement.

The receive hardware was characterized by measurements of transfer functions over the whole MPI relevant frequency range using each receive coil. Comparisons of the x-Rx-coil with the TxRx-coils showed a mean sensitivity increase by a factor of 4. Simulations of the sensitivity profiles were performed, showing good agreement with measurement data (relative difference $< 0.5\,\%$). Based on these profiles, the variations of the sensitivity were determined in the MPI-relevant FOV and were below 15 % for each coil.

Next, empty scanner measurement data were analyzed to characterize the MPI raw signal contributions, generated by other sources than MNPs. With random noise, systematic background signals and distortions, three main components were identified. The signal contributions of these components were determined individually by performing measurements with adapted field settings of the empty scanner.

Random noise, following a $1/f$-characteristic, showed the smallest quantitative influence on the MPI raw signals with maximal amplitudes of about 10 pAm^2. The measured effects are minimized by signal averaging and the use of regularization techniques in the MPI image reconstruction.

Systematic background signals were mainly caused by the excitation fields of the MPI scanner itself and showed the strongest quantitative effects with amplitudes up to several hundreds nAm^2. The main contribution to these signals were caused by the drive fields. Nonlinear behavior of hardware components in the transmission or receive chain result in strong signals at mixed frequencies. Although the gradiometric receive coil design of the Rx-coil provides strong attenuation of these background signals by a mean factor of 65 compared to the standard dual-purpose (field generation and signal acquisition) TxRx-coils, a complete removal is not achieved due to imperfect positioning of the cancellation coil parts. The temporal variations of the drive field amplitudes complicate the necessary removal of the remaining background signal contributions. The mid- and long-term signal contributions

could be removed via background correction methods. However, background signal contributions generated by drive field fluctuations in the short-term regime remain, which are up to 30-fold higher than the signals generated by random noise. These remaining signal contributions will be considered in the further analysis (e.g. calculation of SNR).

A long-term analysis of the MPI raw signals of empty scanner measurements showed strong variations starting from February 2018 for both TxRx-coils with up to ten-fold higher signal amplitudes. Possible causes for these increased signals are damage or wear of hardware components or external distortions. The Rx-coil showed no significant changes during the last 3 years. The results demonstrate that the long-term performance of the MPI scanner can be monitored based on empty scanner measurements extracted from SF data sets, to identify hardware damage or other changes of the measurement setup.

The effects of abrupt signal changes (transient signals) were described and seemed to be correlated with fluctuations observed in the drive fields. Due to the sudden and random occurrence of these transients, a method was developed to characterize the probabilities for their occurrence in a single MPI repetition. These results showed much higher probabilities for the TxRx-coils compared to the Rx-coil, agreeing with the assumption that these effects are correlated to the drive fields.

The observed characteristics for noise and background signals might vary for other MPI scanners, especially if other excitation schemes are utilized (field-free-line scanning, traveling wave MPI, etc.) But the presented analysis can easily be adopted for these systems, as the fundamental physical principles are similar. The knowledge gained by the detailed characterization of MPI noise sets the basis for improved reconstruction results, which can be realized by improved background correction methods and modern regularization techniques [121] (see section 6.1.2).

Concluding the results from this chapter, the separate, gradiometric receive coil (Rx-coil) showed superior performance over the standard dual-purpose (field generation and signal acquisition) coils (TxRx-coils) regarding sensitivity, noise, background signal suppression and distortions. It was demonstrated before, that no major information is lost when only a single receive coil is used for SF-based image reconstruction [122]. Therefore, only the x-Rx-coil is used for data acquisition in the following measurements presented in this work.

Chapter 5

MPI raw signal characterization

This chapter focuses on my investigations conducted to accomplish objective two, analyzing the influence of the MPI raw signal data processing, including each step before the image reconstruction. Section 5.1 demonstrates how the MPI raw signals are converted into magnetic moments, allowing a quantitative and hardware-independent analysis. This technique is further tested and used in section 5.2 to quantify the iron masses of MNP samples, without the need for an image reconstruction, excluding possible distortions or errors from the reconstruction. For this purpose, measurements of MNP samples are performed using adapted MPI excitation fields. The limit of detection and accuracy of this quantification technique are determined and compared to MPS measurements, which are based on the same physical principle (see section 2.4 and section 3.2). Finally, section 5.3 analyzes the MPI raw signal of a measured system function, used in the following chapters for image reconstruction. Averaged signal to noise ratios are defined, which are further utilized for signal truncation to improve the MPI image quality. Partial results of this chapter have been published in HP1.

5.1 MPI raw signal calibration

The fundamental physical property generating the MPI raw signal is the magnetic moment. Inductive receive coils, used to acquire the MPI raw signals, detect only the temporal derivative of the magnetic fields generated by these magnetic moments. In addition, the sensitivity of these receive coils is frequency dependent, complicating a quantitative analysis (see section 4.1.2). This section presents a method for converting the MPI raw signals into magnetic moments, which enables to extract quantitative and hardware-independent information. For this purpose, MNP samples were measured using the same field conditions in the MPI scanner and a calibrated MPS, used as a reference measurement modality.

The MNP type Ferucarbotran was used for each measurement (see section 3.5.1). A sample containing 10 µL Ferucarbotran at an iron concentration of 0.935 mol/L was measured in the MPS at 25 kHz, a field amplitude of 12 mT and a total acquisition time of 10 s. The same sample was measured in the MPI system under equal conditions, using a drive field amplitude of 12 mT in x-direction only, no magnetic gradients (1D-MPI) and the x-Rx-coil for data acquisition. Background correction was performed using empty measurements as described in section 4.2.3. The influence of the MPI receive

chain was compensated by complex division of the determined transfer functions for the MPI-relevant frequency region (see section 4.1.2).

Based on the similar excitation field conditions, the minimal influence of noise and background signals on the measured data after background correction and the removal of the influence of the receive hardware, the detected magnetic moments in MPI and MPS must be similar. The calibration factor for the MPI raw signals from the amplified voltages ($k \cdot V$, dimensionless amplification factor k) to magnetic moments (Am^2) is given by:

$$\phi = \frac{|\hat{u}_{3,\mathrm{MPS}}|}{|\hat{u}_{3,\mathrm{MPI}}|} \tag{5.1}$$

The third harmonic frequency component $|\hat{u}_3|$ was used for the calibration procedure, since it contains the strongest signal for the chosen field settings.

5.2 1D-MPI quantification

Measurements of multiple MNP samples at different iron concentrations were acquired to test the accuracy of the calibration procedure. Additionally, the data acquired from 1D-MPI excitation were used to quantify the iron amount of each sample. Fourteen different samples containing $10\,\mu$L Ferucarbotran with varying iron concentrations between $0.935\,\mathrm{mol/L} - 0.59\,\mu\mathrm{mol/L}$ were measured.

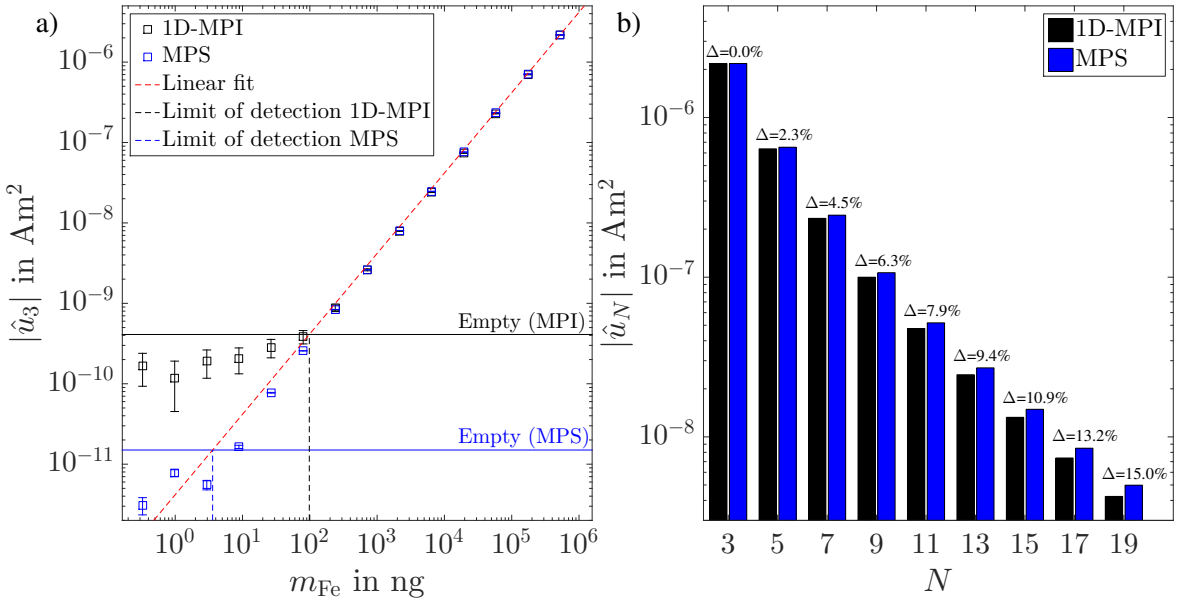

FIGURE 5.1: a) Calibrated amplitudes of the third harmonic acquired with MPS and 1D-MPI measuring Ferucarbotran samples at different iron concentrations. The error bars display the standard deviations. The signals generated by an empty sample are displayed as a horizontal line, which were used to determine the limits of detection of 3.6 ng and 98 ng for MPS and MPI respectively. b) Odd harmonic amplitudes (harmonic number N) acquired for MPI and MPS using the same sample. The relative deviation between MPI and MPS are visualized above each harmonic.

Figure 5.1a) displays the calibrated values of $|\hat{u}_3|$ as a function of m_{Fe}. A linear relationship is observed for both measurement techniques with response indices of $r = 1.03 \pm 0.01$ (MPI) and $r = 1.02 \pm 0.01$ (MPS) (see section 2.4.1). A plateau is reached caused by the influence of noise and background signals of the respective measurement technique, which is used later in this section to determine the limits of detection. Above the plateau, a good agreement between MPS and 1D-MPI measurements is determined with a relative difference of $(2.2 \pm 1.7)\,\%$ (Mean±Std) in $|\hat{u}_3|$. The remaining differences could be related to small temperature differences during the MPS and MPI measurements respectively.

To further verify the use of the calibration factor ϕ, the amplitudes of odd harmonics $|\hat{u}_N|$ are compared for the highest concentrated sample (Figure 5.1b). The relative difference between MPS and 1D-MPI, indicated above each harmonic, increases systematically for higher frequencies up to 15 %. Similar results are observed for lower concentrated samples. This behavior could indicate a remanent offset field in the MPI scanner, caused by a residual magnetization of a hardware component induced by the gradient fields. Other possible sources for the discrepancies could be small deviations from the nominal drive field amplitudes in either the MPS or the MPI system or differences of the sample temperatures during the measurements. Overall, the results demonstrate that the presented calibration procedure accurately converts MPI raw signals into magnetic moments for low harmonics.

The signal to noise ratio (SNR) was used to define the limits of detection for both measurement techniques, as described in section 2.4.2:

$$\mathrm{SNR} = \frac{|\hat{u}_{3,\mathrm{Signal}}|}{|\hat{u}_{3,\mathrm{BG}}|} \tag{5.2}$$

The mean of the background signal $|\hat{u}_{3,\mathrm{BG}}|$, determined based on twenty empty measurements, was used instead of the standard deviation for the calculation of the SNR, to include possible remaining systematic background signals after performing the background correction (see section 4.2.3). The determined limits of detection for MPS and MPI are 3.6 ng and 98 ng of iron using Ferucarbotran. Since the generated signal depends on the properties of the MNP type, the limit of detection differs for other MNP types. The lower limit of detection of the MPS setup is mainly caused by two factors: A smaller coil radius of $R = 6$ mm compared to the $R = 36$ mm of the coil used in the MPI scanner and an improved cancellation of the background signals generated by the drive field. The determined limits of detection are only valid for the chosen field settings and differ for other frequency components. The same analysis was performed using the MPI data without performing the background correction, which resulted in an about 75-fold higher limit of detection of 7300 ng, demonstrating the importance of removing the background signals.

Quantification of m_{Fe} was performed based on a reference measurement as described in section 3.2. Comparing the iron masses determined by MPS or MPI with the nominal reference values, a combined standard uncertainty of $u_{\mathrm{c,MPS}} = 6.8\,\%$ and $u_{\mathrm{c,1DMPI}} = 8.9\,\%$ were acquired (see section 2.4.3). These accuracies were caused by the influence of random noise and temporal variations of background signal contributions, discussed in section 4.2. Additionally, the uncertainty of the determination of $m_{\mathrm{Fe,ref}}$

might influence these values, which was neglected in this study to completely focus on the MPI-related parameters. Each characteristic described above is dependent on the local environmental conditions of the MNPs, which is analyzed in more detail in chapter 7.

5.3 System function analysis

The previous section demonstrated the possibility to extract quantitative information about the MNP amount from 1D-MPI measurements. These measurement data provide no information about the spatial position or distribution of MNPs and can only be used to determine the total iron quantity. Spatial encoding is achieved by employing a static magnetic gradient field ($G_z = 2.5\,\mathrm{T/m}$) and 3D-MPI excitation ($B_x = B_y = B_z = 12\,\mathrm{mT}$) as described in section 2.2.2. The amplitude spectrum acquired from a sample containing 10 µL Ferucarbotran ($c_{\mathrm{Fe}} = 0.935\,\mathrm{mol/L}$), positioned at the center of the FOV using these field settings, is displayed in figure 5.2.

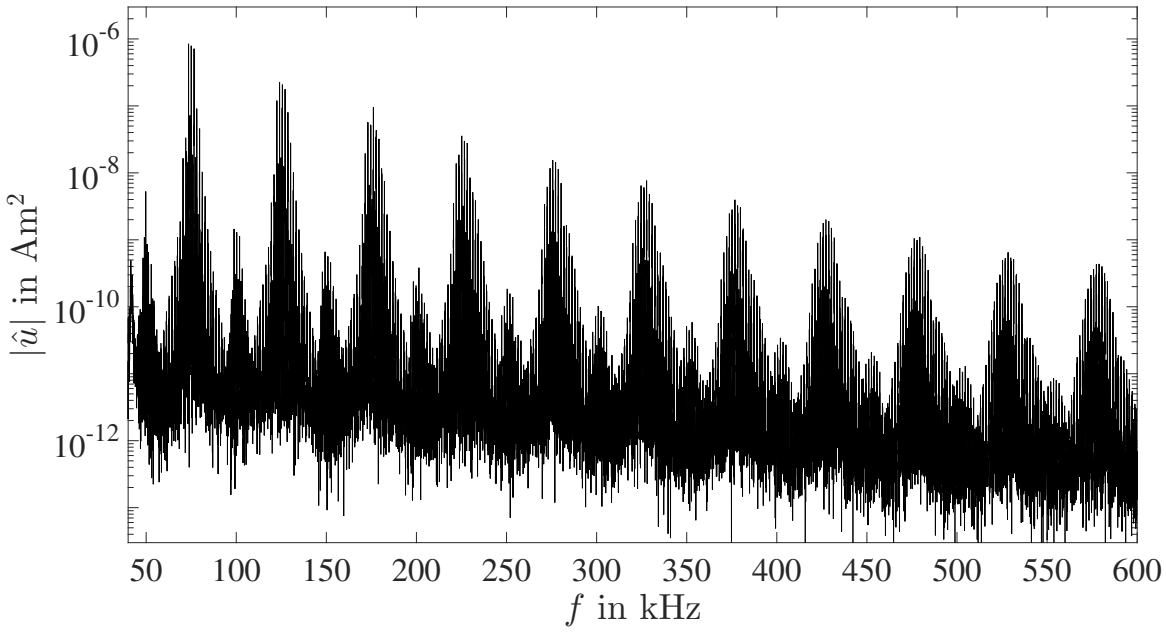

FIGURE 5.2: Amplitude spectrum of a MNP sample containing 10 µL Ferucarbotran at an iron concentration of 0.935 mol/L measured at the center of the FOV. Signal excitation was performed using drive field amplitudes of $B_x = B_y = B_z = 12\,\mathrm{mT}$ and a magnetic gradient strength of $G_z = 2.5\,\mathrm{T/m}$. The strongest signal contributions were detected around the odd harmonic frequency components of the excitation frequencies.

The strongest amplitudes were detected around the odd harmonic frequency components, decreasing for higher mixing orders. In principle, quantification is feasible using each frequency component in a similar way as presented in section 5.2. However, this requires that the spatial distribution of the MNP ensemble is known and does not change over time, since the magnetic gradient affects the MPI raw signals dependent on the spatial position.

To investigate the influence of the spatial position of MNPs on the MPI raw signals, a SF was acquired and analyzed. Measurements were performed using a sample containing 1 µL Ferucarbotran ($c_{\mathrm{Fe}} = 0.935\,\mathrm{mol/L}$) in a cubic $1\,\mathrm{mm}^3$ container. The sample was moved on a discrete grid with 32x32x16 positions through a field of view covering $22\mathrm{x}22\mathrm{x}11\,\mathrm{mm}^3$ using a robot. At each position, 100 measurement repetitions were acquired and averaged. After 32 measured positions, the sample was moved completely outside the scanner to acquire five empty scanner measurements. These empty measurements were used to interpolate the MPI raw signals of each frequency component over the whole acquisition time to remove background signals from the data (see section 4.2.3).

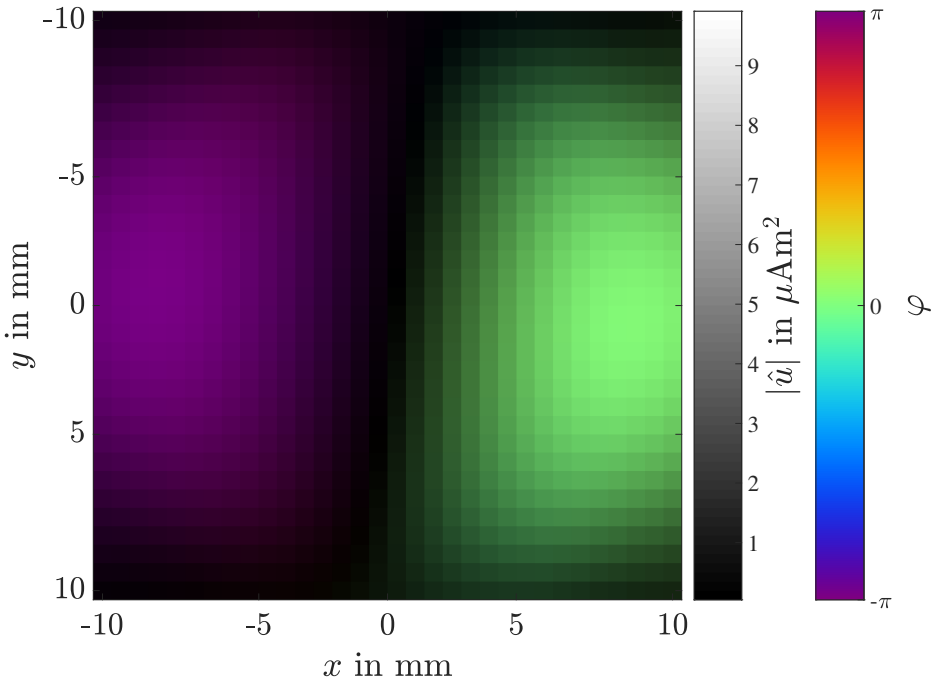

FIGURE 5.3: Spatial dependence of amplitude (visualized by brightness) and phase (visualized by color) of a frequency component generated by the mixing orders $n_x = 1$, $n_y = 1$, $n_z = 0$ in a central slice ($z = 0$).

Figure 5.3a) presents the spatial dependence of the MPI raw signal for a single frequency component. Displayed are amplitude (brightness) and phase (color) in a central ($z = 0$) slice for the frequency component generated with mixing orders $n_x = 1$, $n_y = 1$, $n_z = 0$ (see section 2.2.2). Figure 5.3b) shows the same slice for multiple frequency components generated by different mixing orders. Frequency components generated by higher mixing orders are linked to higher spatial frequencies. For high mixing orders, the spatial patterns are disturbed by noise. By analyzing these SF patterns, estimations of the performance of different MNP types (e.g. the spatial resolution) can be made [45, 46]. In general, frequency components generated by high mixing orders are required to achieve a high spatial resolution in the MPI image.

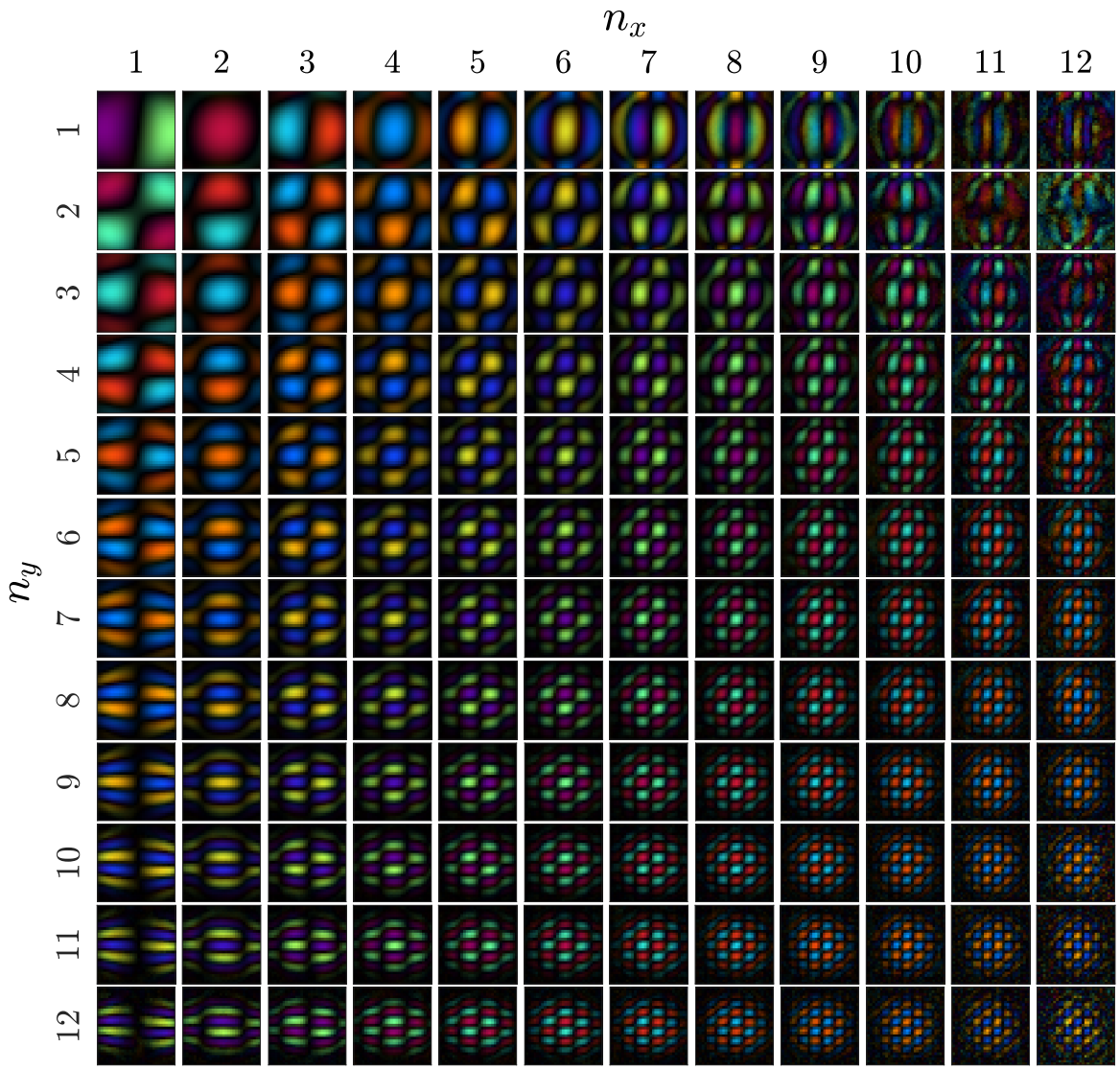

FIGURE 5.4: Same slice as displayed in figure 5.3 for multiple frequency components generated by varying mixing orders n_x and n_y (n_z=0 for all). The amplitude color bars were scaled based on the maximal amplitude for each frequency component respectively. Higher mixing orders are linked to higher spatial frequencies and therefore needed to resolve finer structures.

To be able to make estimations about the mean signal strength for each frequency component, a mean SNR is defined based on the full SF data by averaging over each spatial position M:

$$\mathrm{SNR} = \frac{\sum_{m=1}^{M} |\hat{u}_m|/M}{\sum_{n=1}^{N} |\hat{u}_{n,\,\mathrm{BG}}|/N} \tag{5.3}$$

with m as the index for the spatial position, and n as the index of N total empty scanner measurements.

Figure 5.5a) displays the SNR as a function of frequency. The highest SNR-values are observed around the pure harmonic frequency components. Additionally, mean $\overline{\mathrm{SNR}}$-values were determined by averaging over each frequency component, generated by the same mixing order $n_{\mathrm{mo}} = |n_x| + |n_y| + |n_z|$

(see figure 5.5b). An overall decrease for higher mixing orders is observed. Even mixing orders showed higher SNR-values based on stronger background signal contributions determined for odd harmonic frequency components as described in section 4.2.2.

The SNR-values are used to truncate the number of frequency components, before image reconstruction is performed. Since they were determined by averaging over each position inside the FOV, no additional information about the spatial position has to be considered. Due to the linear scaling of the MPI raw signal amplitudes with m_{Fe}, the limit of detection can be estimated for each frequency component as described in section 2.4.2. Analyzing the frequency component with the highest SNR an limit of detection of 18 ng was determined for Ferucarbotran. Since the SNR represents averaged values over each spatial position, the limit of detection might differ for certain particle distributions.

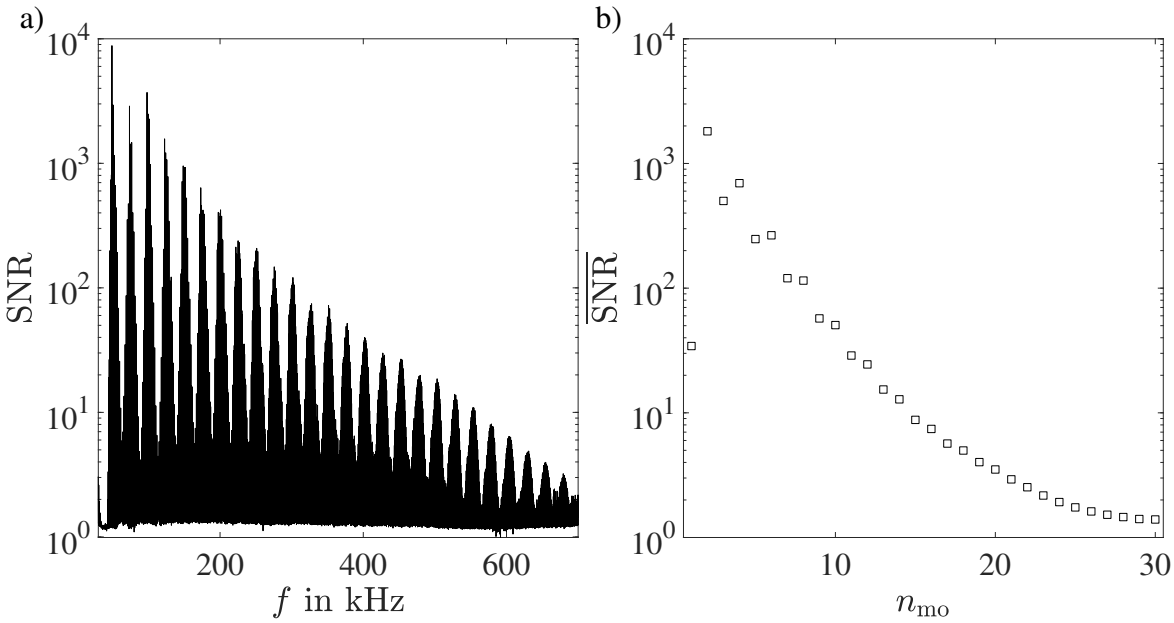

FIGURE 5.5: a) SNR determined from a SF acquisition by averaging over the data acquired for all sample positions (see equation 5.3), displayed as a function of frequency. b) Averaged SNR values ($\overline{\mathrm{SNR}}$) dependent on the mixing order. Even mixing orders showed a higher $\overline{\mathrm{SNR}}$ compared to odd frequency components, due to smaller contributions of background signals for even harmonics.

5.4 MPI raw signal characterization: Summary and discussion

The focus of this chapter was to analyze the data processing steps before image reconstruction (objective two). MNP samples were measured and the signals were converted into magnetic moments, which is the underlying physical property relevant for the MPI signal generation and allows a quantitative and hardware-independent analysis. This was achieved by correcting the frequency-dependent influence of the hardware components and by removing background signals from the MPI raw measurement data. The presented calibration technique showed good agreement with calibrated MPS measurements and a mean relative deviation of $(2.2 \pm 1.7)\,\%$ for the amplitude of the third harmonic $|\hat{u}_3|$. Other frequency

components showed systematically growing deviations with increasing frequency, which could indicate a remanent static offset field inside the MPI scanner. The calibration of the MPI raw signals to absolute units is beneficial to compare different MNP types and simplifies inter-site comparisons between MPI scanners.

Quantification of m_{Fe} was achieved based on the amplitude of the third harmonic $|\hat{u}_3|$ using MPS and MPI. Limits of detection of 3.6 ng (MPS) and 98 ng (MPI) and accuracies of $u_{\mathrm{c,MPS}} = 6.8\,\%$ and $u_{\mathrm{c,MPI}} = 8.9\,\%$ were acquired for the widely used MNP type Ferucarbotran. The limiting factor, determining the limit of detection and the accuracy, is the influence of noise and background signals. Performing the analysis with the same data without using the background correction resulted in an 75-fold higher limit of detection. Further improvements are expected when the remaining background signal contributions (described in the previous section 4.2.3) are removed, e.g. by optimizing the positions of the cancellation coils. Measurements performed using multi-dimensional excitation demonstrated that signal components are generated at mixed frequency components. Since the background signal contributions vary depending on the frequency component, the limit of detection might be further reduced by analyzing different frequency components.

Next, the spatial patterns of a SF were analyzed and the MPI raw signals used to define an averaged SNR-value for each frequency component. These SNR-values set the basis for the choice of frequency components used in the image reconstruction, and are used to improve the image quality as described in the following section 6.1.1. Additionally, an imaging limit of detection of 18 ng was estimated, which is in good agreements with the imaging results presented in the following section 6.2.

In conclusion, the MPI raw signals were successfully converted into magnetic moments. This required a detailed characterization of the influence of the receive hardware and the removal of background signals to yield accurate results. Based on this calibration, quantitative information about m_{Fe} was extracted from the MPI raw signals. Additionally, parameters were defined, based on the MPI raw signals, with beneficial information for the image reconstruction, which are further utilized in the following chapters.

Chapter 6

Quantitative imaging

This chapter shows the results of my investigations focusing on reconstructed MPI images of MNP distributions. The previous sections demonstrated that quantification of the MNP amount is feasible by analyzing the MPI raw signals. However, this approach is only capable of quantifying the total iron mass without information about the spatial distribution of MNPs, which is highly valuable for many biomedical applications. The spatial distribution of MNPs is obtained by performing the image reconstruction as described in section 2.2.3.

The first section of this chapter 6.1 focuses on the quantitative influence of the image reconstruction and the adjustable image reconstruction parameters on the MPI images (objective two). Next, section 6.2 presents results of phantom measurements, in which the limit of detection and accuracy of MPI quantification based on reconstructed images are determined. Section 6.3 compares the MPI results to MRI measurements, as one of the most common biomedical measurement techniques for imaging and quantification of MNPs. For each of the above mentioned measurements, the conditions of the MNP environment are known and are not changed during or in between measurements. The influence of the MNP environment on MPI and MRI quantification is analyzed in section 6.3.2, which is further investigated in chapter 7 (objective three).

6.1 Influence of reconstruction parameters

The MPI image is obtained by solving a least square minimization problem as described in section 2.2.3. Multiple algorithms and techniques to solve this problem were presented during the last years [47–57]. Although many studies investigated the performance regarding the image quality and computation time, little attention was paid to the quantitative influence on the reconstructed values. In this section, a reconstruction parameter study is performed with the focus on the quantitative influence.

The most-used reconstruction algorithm for MPI is the Kaczmarz-algorithm with Tikhonov regularization. This is mainly due to the high convergence speed and the possibility to implement additional constraints (e.g. real, non-negative values) [47, 78, 123]. Each reconstruction in this work was performed using the Kaczmarz algorithm with non-negativity and non-imaginary restraints, but the presented analysis can easily be adapted for other techniques. Using the Kaczmarz algorithm, three reconstruction parameters need to be adjusted: The number of frequency components used in the

reconstruction (N_{FC}), the regularization parameter (λ) and the number of iterations (N_{it}). The choice of these parameters varies strongly based on the application. In the majority of published MPI studies, these parameters were manually adjusted based on visual inspection of the reconstruction results [15, 26, 27, 32, 36, 38, 39, 79, 114, 124–129].

This section investigates the impact of each reconstruction parameter on the qualitative and quantitative MPI results. A dot-like phantom (about 1x1x1 mm^3) was prepared using 1 µL Ferucarbotran ($c_{Fe} = 0.935\,mol/L$) and is displayed in figure 6.1. Dot-like phantoms were chosen to concentrate completely on the analysis of the quantitative information in MPI imaging data and minimize influences from more complex spatial distributions. The sample was measured at the center of the FOV. See A.2 for a detailed list of the measurement, SF and reconstruction parameters. The identical sample was used to acquire the measurement data and the SF, to minimize the uncertainties of sample preparation. Background signal correction was performed using empty scanner measurements as described in section 4.2.3. In the following sections 6.1.1, 6.1.2 and 6.1.3, the qualitative and quantitative influence of each reconstruction parameter is analyzed, using the same measurement data for each reconstruction. Section 6.1.4 summarizes and discusses the results and proposes methods for choosing reconstruction parameters for accurate quantification.

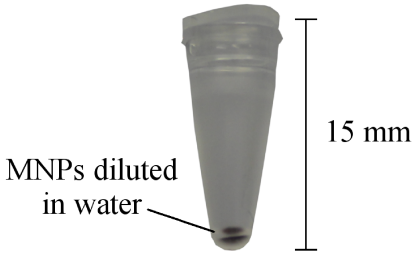

FIGURE 6.1: Photograph of the measured sample: Fast reaction tube filled with 1 µL Ferucarbotran diluted in water.

6.1.1 Frequency component selection

Qualitative influence

The truncation of frequency components is mandatory to minimize the influence of noise on the reconstructed images [130]. Additionally, it is beneficial to exclude frequency components, which show remaining background signal contributions and variations after background correction (see section 4.2.3). The selection of frequency components is usually performed based on SNR-values, defined using the MPI raw signals (see section 5.3) [47]. Only those frequency components are included for which the SNR is above a certain threshold σ_t. The threshold is often chosen manually depending on the determined signal amplitudes of the measurement data [38].

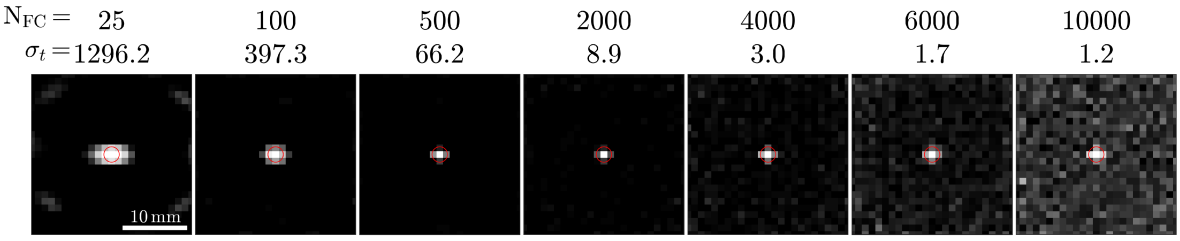

FIGURE 6.2: Reconstructions of a dot-phantom determined with varying number of frequency components N_{FC}. The corresponding SNR thresholds (σ_t) are depicted. The red circles mark the nominal sample sizes and positions. Displayed are intensities integrated along the z-axis. The color bars were adjusted based on the maximal intensity for each image respectively. The spatial resolution increases with N_{FC}. By including too many frequency components, the images are disturbed by noise.

Figure 6.2 shows reconstructed images of the dot-phantom using a varying number of frequency components $N_{FC} = 25 - 10000$ chosen based on the SF-SNR. $N_{it} = 10000$ iterations were used to ensure convergence and no regularization ($\lambda = 0$) was applied. These parameters were chosen to analyze the influence of N_{FC} as independent from the influence of λ and N_{it} as possible. Presented are integrated intensities (along z-axis) to visualize the 3D data in a 2D image. The color bar was adjusted based on the maximal intensity for each image individually. The red circle displays the nominal sample size and position. Each following MPI image presented in this work is visualized in a similar way. N_{FC} and the corresponding SNR threshold σ_t are depicted above each reconstruction. For low $N_{FC} < 25$ imaging artifacts at the edges of the FOV are visible. Qualitatively, the spatial resolution increased with N_{FC}, leading to an improved localization of the dot-phantom. This was caused since more frequency components were included in the reconstruction generated by higher mixing orders, which are linked to high spatial frequencies as presented in section 5.3. But for high $N_{FC} > 4000$ images are disturbed by noise, complicating a clear identification and localization of the dot-phantom. These effects are caused by including frequency components with SNR < 3.

Quantitative influence

A quantitative image analysis is usually performed by analyzing the image intensities in certain region of interests (ROIs). Here, it is assumed that no a priori knowledge of the MNP distribution is given. Hence the intensities are integrated over the whole FOV, including possible distortions by noise or imaging artifacts. The image intensity was then converted into the iron mass $m_{Fe,MPI}$ by scaling with the iron mass of the SF sample (see section 2.2.3). Figure 6.3 depicts $m_{Fe,MPI}$ as a function of N_{FC}. The blue line represents the nominal iron mass of the dot-phantom. Below $N_{FC} < 1000$ (σ_t=24.8), no significant variation of $m_{Fe,MPI}$ is observed. Compared to the nominal iron mass, the MPI determined values overestimate the iron quantity by a mean value of 14.7 µg (relative deviation 24.3 %). These variations could be related to noise and background signals in the data. Above $N_{FC} > 1000$, $m_{Fe,MPI}$ increases, resulting in overestimations of the nominal iron mass of up to hundreds of µg (> 1000 %).

These strong deviations were likely caused by frequency components with a low SNR leading to an unstable solution based on the lack of regularization.

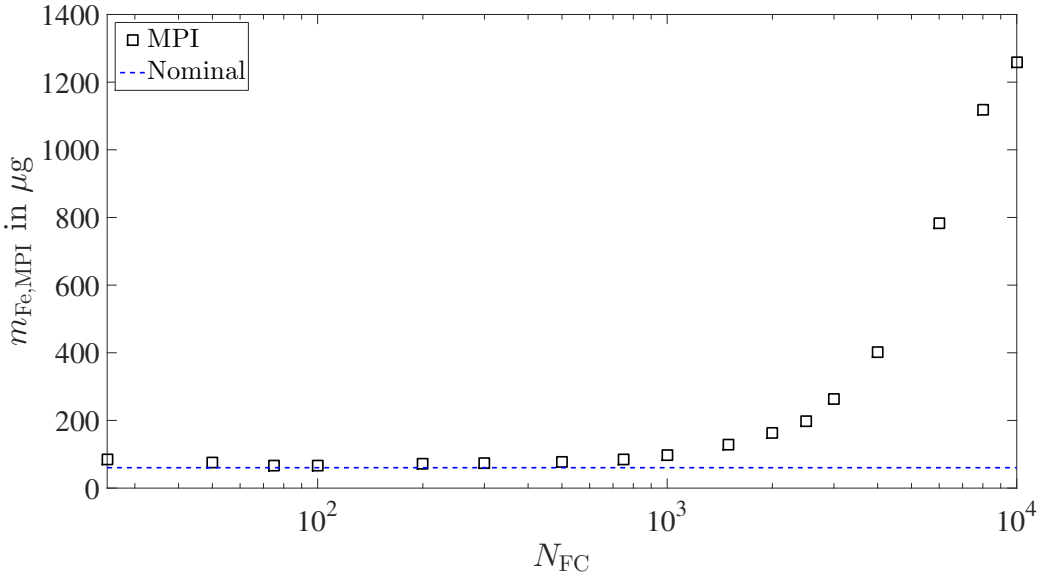

FIGURE 6.3: Quantified iron mass $m_{\mathrm{Fe,MPI}}$ determined based on MPI images dependent on the number of frequency components ($\mathrm{N_{FC}}$) used in the reconstruction. The blue line represents the nominal iron mass of the measured dot-phantom. Big deviations from the nominal iron mass are observed for $\mathrm{N_{FC}} > 1000$ due to the increased noise in the images by including frequency components with a low SNR.

6.1.2 Regularization

Ill-posed problems require regularization, to guarantee a stable solution (see section 2.2.3) [131, 132]. The most used technique for MPI applications is the Tikhonov regularization [133]. In general, this technique approximates the original, ill-posed linear system by a second system, which is well-posed. The regularization parameter λ determines the weight of the approximation. The choice of λ can be performed automatically using e.g. the L-curve or U-curve method [134, 135]. However, these techniques require long computation times and do not yield optimal MPI reconstruction results in all cases [47]. Therefore, λ is usually adjusted manually. An initial guess is determined by $\lambda_0 = \mathbf{S}^H\mathbf{S}$. Most MPI publication state the so called relative regularization parameter $\hat{\lambda}$, which is defined as a scaling factor in the following way: $\lambda = N^{-1}\hat{\lambda}\lambda_0$, where N denotes the number of columns of the system function $\mathbf{S}$.

Qualitative influence

Figure 6.4 shows reconstructions of the dot-phantom determined for $\mathrm{N_{FC}} = 10000$ and varying $\hat{\lambda}$ to demonstrate the influence of regularization on noisy data . $\mathrm{N_{it}} = 10000$ iterations were used to ensure convergence. Qualitatively, no considerable influence is observed for $\hat{\lambda} < 10^{-10}$. The noise in the image is suppressed and the image quality improved significantly by increasing $\hat{\lambda}$. The increase of $\hat{\lambda}$

also results in blurring of the image, complicating the localization of the dot-phantom. Based on visual inspection, the optimal regularization is determined to be $\hat{\lambda} \approx 10^{-5}$.

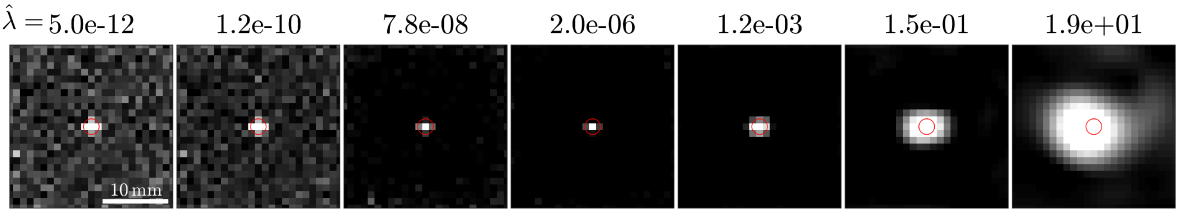

FIGURE 6.4: Reconstructions of a dot-phantom determined with varying regularization parameter $\hat{\lambda}$. The red circles mark the nominal sample positions. The color bars were adjusted based on the maximal intensity for each image respectively. Increasing $\hat{\lambda}$ results in suppression of noise but also leads to blurring if $\hat{\lambda}$ is chosen too high.

Quantitative influence

Increasing $\hat{\lambda}$ results in a stronger suppression of noise in the measurement data and a decrease of $m_{\text{Fe,MPI}}$ (see figure 6.5). The range between $10^{-5} < \hat{\lambda} < 10^{2}$ shows the smallest variation and minimal influence on the quantitative values. A minimal deviation compared to the nominal iron mass of the dot-phantom of 5.7 µg (relative deviation 9.5 %) is determined for $\hat{\lambda} = 6.1 \cdot 10^{-3}$. Using the optimal regularization parameter determined based on visual inspection results in a higher deviation of 7.7 µg (relative deviation 12.7 %). This demonstrates that the choice based on a visual inspection of the reconstructed images does not necessarily provides the most accurate quantification results. Over-regularization is reached for $\hat{\lambda} > 10^{2}$ leading to a decrease of $m_{\text{Fe,MPI}}$ to zero.

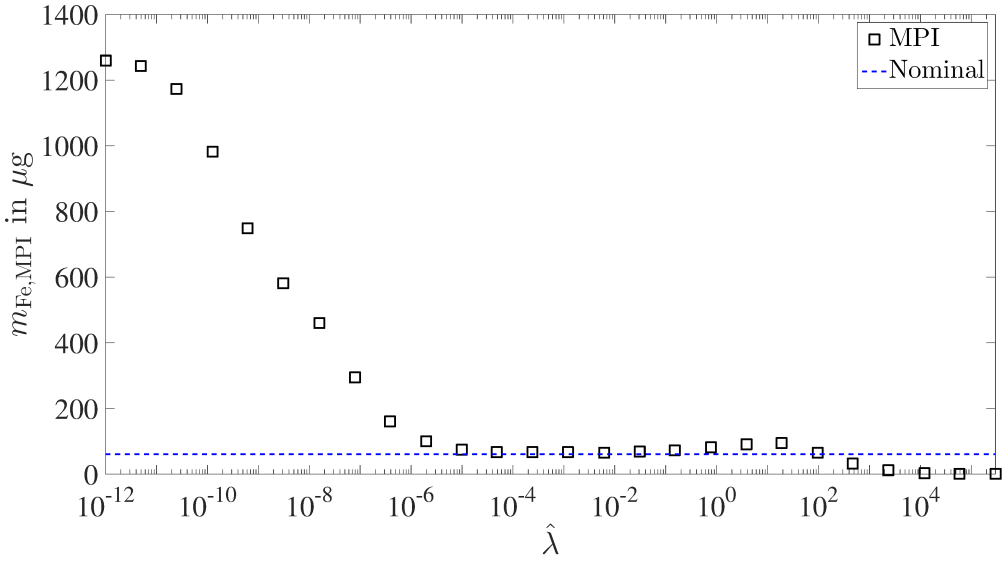

FIGURE 6.5: Quantified iron mass $m_{\text{Fe,MPI}}$ determined based on MPI images dependent on the regularization parameter ($\hat{\lambda}$) used in the reconstruction. The blue line represents the nominal iron mass of the measured dot-phantom. Increasing $\hat{\lambda}$ suppresses noise and therefore $m_{\text{Fe,MPI}}$ approaches the nominal iron mass. If $\hat{\lambda}$ is chosen too high, $m_{\text{Fe,MPI}}$ decreases to zero.

6.1.3 Number of Iterations

Qualitative influence

Since the Kaczmarz algorithm is an iterative technique, the number of iterations N_{it} can be adjusted. In general, N_{it} needs to be chosen high enough to ensure convergence of the solution. The number of iterations also act as a regularization technique [125, 136]. Fast convergence after only a few iterations was reported for most MPI applications, based on the high orthogonality of SF components [47]. Previous MPI studies report, that a degradation in image quality was observed when increasing N_{it} above a certain number [47, 125].

Figure 6.6 displays reconstructions of the dot-phantom performed with $N_{FC} = 10000$ and varying N_{it}. The regularization parameter was chosen to be $\hat{\lambda} = 10^{-5}$ based on visual inspection. Imaging artifacts and noise disturb the results for iterations below 25. The influence of these distortions decreases with N_{it} leading to image quality improvements. No significant image quality improvements are visible when N_{it} was further increased (> 25). No image degradations are observed for $N_{it} \leq 10000$, which could be related to the simple spatial structure of the dot-phantom. Higher number of iterations are rarely used, due to long computation times (in this case up to 2.5 h for a single reconstruction).

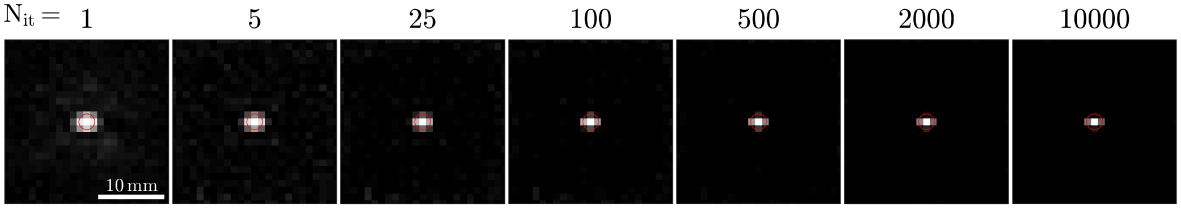

FIGURE 6.6: Reconstructions of a dot-phantom determined with varying number of iterations N_{it}. The red circles mark the nominal sample positions. The color bars were adjusted based on the maximal intensity for each image respectively. Qualitative improvements in terms of spatial resolutions are observed when N_{it} is increased. Above $N_{it} > 25$ no big differences are observed.

Quantitative influence

$m_{Fe,MPI}$ decreases depending on N_{it} as depicted in figure 6.7. This decrease could be related to the minimization of artifacts, which result in overestimations of the nominal iron mass. Although no significant qualitative differences are observed for $N_{it} > 25$, the quantitative results show strong deviations until convergence is reached around $N_{it} > 1000$. This also underlines that a choice of the reconstruction parameters based on a visual inspection is not sufficient to guarantee accurate quantification results. The MPI determined iron mass converges to the nominal iron quantity of the dot-phantom.

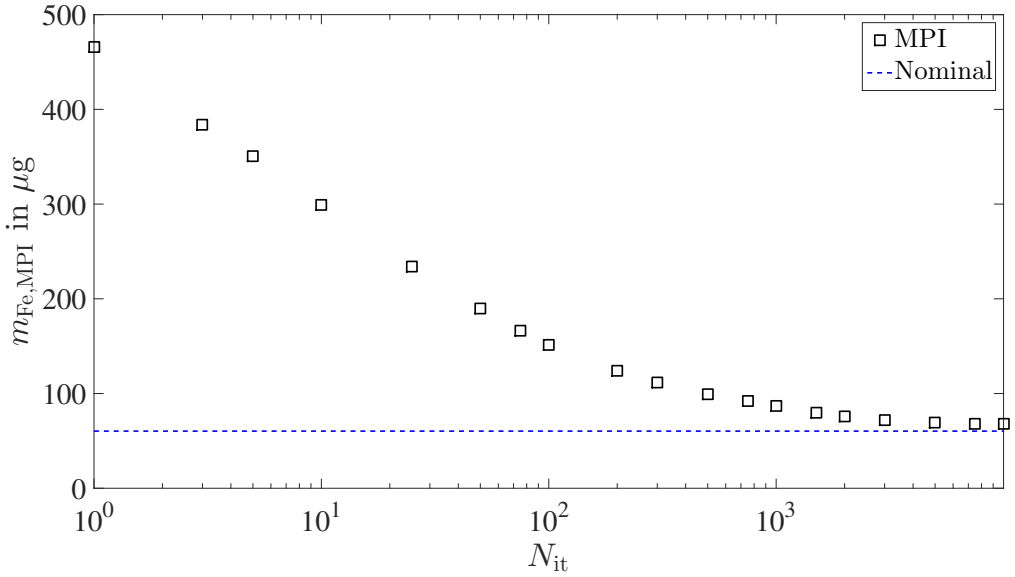

FIGURE 6.7: Quantified iron mass $m_{\mathrm{Fe,MPI}}$ determined based on MPI images dependent on the number of iterations (N_{it}) used in the reconstruction. The blue line represents the nominal iron mass of the measured dot-phantom. $m_{\mathrm{Fe,MPI}}$ converges to the nominal iron mass with increasing N_{it}.

6.1.4 Reconstruction parameter choice

The previous sections demonstrated the strong influence of each reconstruction parameter on the qualitative and quantitative results. Already for a simple dot-phantom, containing a large quantity of MNPs, deviations up to several hundred percent compared to the nominal iron content of the sample were determined although the same MPI raw data were used. Even bigger deviations are expected for more complex spatial distributions or for lower iron content in the measured sample. These strong deviations complicate accurate MPI quantification. Therefore, two methods offering solutions for this problem are hypothesized, aiming to provide accurate quantification while maintaining a flexible choice of the reconstruction parameters.

Method 1

The reconstruction parameters are adjusted manually based on visual inspection of the image and the same parameters are used for each reconstruction. An additional reference measurement has to be performed using a sample with known $m_{\mathrm{Fe,ref}}$, which is reconstructed with the chosen parameters. The integrated reference image intensity I_{ref} are calculated in an ROI centered around the nominal sample location. The iron mass $m_{\mathrm{Fe,MPI}}$ of each subsequent measurement is calculated by using the relative image intensities compared to the reference scan:

$$m_{\mathrm{Fe,MPI}} = \frac{I}{I_{\mathrm{ref}}} m_{\mathrm{Fe,ref}} \tag{6.1}$$

The advantages of this method are that each reconstruction parameter can be manually optimized for different purposes (e.g. high spatial resolution/temporal resolution/sensitivity), while still providing quantitative results. On the downside, an additional measurement and reconstruction has to be performed, which requires time and a suitable reference phantom with known $m_{\mathrm{Fe,ref}}$. This technique is used to obtain the results presented in the next section 6.2.

Method 2

The presented method 1 is problematic when multi-color MPI reconstructions are performed, since this would require multiple reference samples with known $m_{\mathrm{Fe,ref}}$ (see section 2.2.3). In many MPI applications, no suitable reference sample are available. In the following, a second method is proposed, focused on multi-color reconstructions. This method can be described as discrete optimization [137]. If the nominal iron mass of the measured object/patient for one of the reconstructed MNP distributions is known ($m_{\mathrm{Fe,ref}}$, e.g. by measurements of fiducial markers for localization at the beginning of a measurement), the optimal reconstruction parameters are determined and used for each subsequent reconstruction:

$$|m_{\mathrm{Fe,MPI}} - m_{\mathrm{Fe,ref}}| \xrightarrow{\mathrm{N_{FC}},\mathrm{N_{it}},\lambda} \min \tag{6.2}$$

A straightforward way to find the "optimal" reconstruction parameter set is achieved by varying each parameter in a certain range. These ranges are adapted iteratively to minimize $|m_{\mathrm{Fe,MPI}} - m_{\mathrm{Fe,ref}}|$. Additional constraints for $\hat{\lambda} < 10^3$ and $\sigma_t > 3$ are applied to prevent over-regularization and disturbance from noise in the measurement data, as described in sections 6.1.1 and 6.1.2. Depending on the parameter range, this procedure is very time consuming (several hours up to days). The big advantage compared to method 1 is that only partial information about the nominal MNP distributions is needed and no additional measurements have to be performed. This method is used to obtain the results presented in chapter 7.

6.2 Characteristics of MPI quantification

Little information about the characteristics of MPI quantification can be found in published literature. Multiple studies report the limit of detection for MPI measurements. Graeser et al. presented a summary of multiple limits of detection obtained from different MPI scanners [38]. But other important parameters, e.g. the accuracy of MPI quantification compared to a known reference measurement (e.g. MPS or MRI) is rarely stated in any of these published studies. This section presents measurements performed to determine the main characteristics of MPI quantification under idealized conditions, as presented in section 2.4. The knowledge gained from the previous sections is utilized to determine the dominating factors for MPI quantification based on reconstructed images. Partial results of this section have been published in HP2 and HP3.

6.2.1 Total iron mass

A serial dilution of Ferucarbotran was prepared with samples containing 1 µL volumes with varying total iron amounts of $m_{\mathrm{Fe}} = 4.1\,\mu\mathrm{g}$ to $m_{\mathrm{Fe}} = 0.5\,\mathrm{ng}$ filled into fast reaction tubes (MicroAmp Fast Reaction Tubes, 0.2 mL Appl. Biosystems, USA, see figure 6.1). These samples were used to determine the limit of detection and quantification accuracy based on reconstructed MPI images. Dot-like phantoms were used, to minimize the impact of the field-free-point-encoding scheme and the gradient fields [38]. The iron content was verified by MPS measurements, which was calibrated using a reference sample with a known quantity of MNP (see section 5.2).

MPI measurements were performed using drive field amplitudes of 12 mT in x-, y- and z-direction a gradient strength of $G_z = 2.5\,\mathrm{T/m}$ and 100 averages. For decreasing m_{Fe} the MPI raw signal generated by MNPs decreases and therefore the relative influence of noise and background signals on the reconstructed image increases, leading to stronger imaging artifacts. In a real application, without a priori knowledge about the MNP location, such artifacts could be misread as actual MNPs. To prevent misinterpretation of these artifacts, 27 measurement repetitions (1 min acquisition time) were performed for each sample at three locations inside the FOV (A=$(-5,-5,0)$ mm, B=$(0,0,0)$ mm, C=$(5,5,0)$ mm), respectively. Empty scanner measurements were acquired for each new sample and used to correct for background signals as described in section 4.2.3. The reconstruction parameters were chosen according to method 1, presented in section 6.1.4. A summary of the measurement, SF and reconstruction parameters is given in A.2.

Qualitative analysis

Figure 6.8 presents the reconstructed MNP distributions for positions A, B and C. Since the intensities vary over a large range depending on the iron content of the measured sample, the color bars were adapted individually based on the maximal intensity of each image for improved visibility. The use of a high regularization parameter minimized the influence of noise on the reconstructions and were used to increase the MPI sensitivity. This also resulted in strong blurring effects as described in section 6.1.2, overestimating the actual sample size. Samples containing $m_{\mathrm{Fe}} \geq 20\,\mathrm{ng}$ are reconstructed accurately at the nominal positions A, B and C, marked with a red cross. Measurements of samples containing lower iron quantities are disturbed by noise causing imaging artifacts and the samples are not reconstructed at their nominal positions, which could result in misinterpretations in a real application. Above this threshold, no significant image quality differences are observed, when using the same reconstruction parameters.

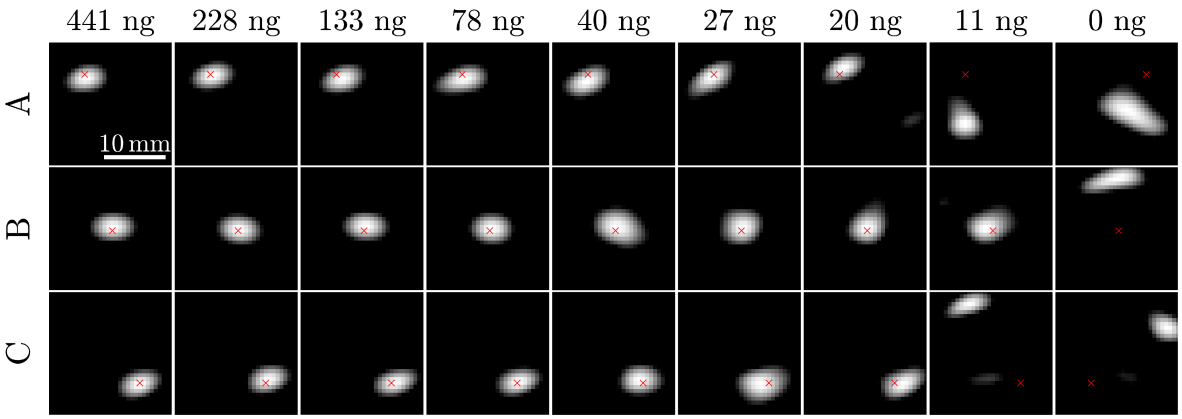

FIGURE 6.8: MPI images of dot-phantoms measured at three positions A,B and C with the nominal sample positions visualized by a red cross. The color bars were adapted individually for each image, for improved visibility of the large range of intensities. A quantitative analysis of the data is presented in figure 6.9. Shown is one representative data set of 27 individual measurements for each position. Samples containing $m_{\mathrm{Fe}} \geq 20\,\mathrm{ng}$ are reconstructed at the correct location. Reconstructions of samples containing less MNPs exhibit imaging artifacts and might lead to misinterpretations of the real MNP distributions.

Quantitative analysis

Iron quantification was performed by extracting $m_{\mathrm{Fe,MPI}}$ from the reconstructions in an ROI centered around the nominal sample positions. Only voxels with intensities above a threshold 0.5 of the maximal intensity were included in the calculation, to minimize the influence of imaging artifacts. Figure 6.9 displays $m_{\mathrm{Fe,MPI}}$ over the nominal iron mass $m_{\mathrm{Fe,nominal}}$ for positions A, B and C. Shown are mean values over 27 repetitions with the standard deviations as error bars. A linear relationship is observed above a certain iron mass, which is verified by a response index of $r = 1.02 \pm 0.02$ determined as described in section 2.4.1. SNR-values are defined in a similar way as in section 5.2 using the intensities instead of the MPI raw signals, to determine the limit of detection. Empty scanner measurements were reconstructed to acquire the contribution of noise and background signals (visualized as horizontal lines in figure 6.9). The limit of detection was calculated as described in section 2.4.2 and determined to be 16 ng. These results agree with the results obtained from the previous analysis performed in section 5.3, from which a limit of detection of 18 ng was estimated. This demonstrates that the limit of detection is mainly caused by the noise and background signals, characterized in section 4.2, and is not strongly affected by the image reconstruction. Minor differences of the limit of detection below 2 ng were determined depending on the spatial position of the dot-phantom. This could be caused by the fact, that different frequency components are essential to reconstruct the dot-phantom at a given position. The temporal variation of background signals differs for each frequency component as described in section 4.2, which results in different limits of detection.

To demonstrate the importance for the removal of background signals, the same analysis was performed using the same data without performing the background correction. This resulted in an almost 30-fold higher limit of detection of about 441 ng.

The MPI quantification accuracy was determined for samples with iron masses above the limit of quantification by a relative combined standard uncertainty of $u_{c,MPI} = 8.8\,\%$ (see section 2.4.3). This value is similar to the accuracy determined for quantification based on the MPI raw signals presented in section 5.2 and is mainly determined by noise and varying background signals. The stated characteristics are only valid using Ferucarbotran diluted in pure water at room temperature and differ for other MNP types or environmental conditions, which is discussed in more detail in chapter 7.

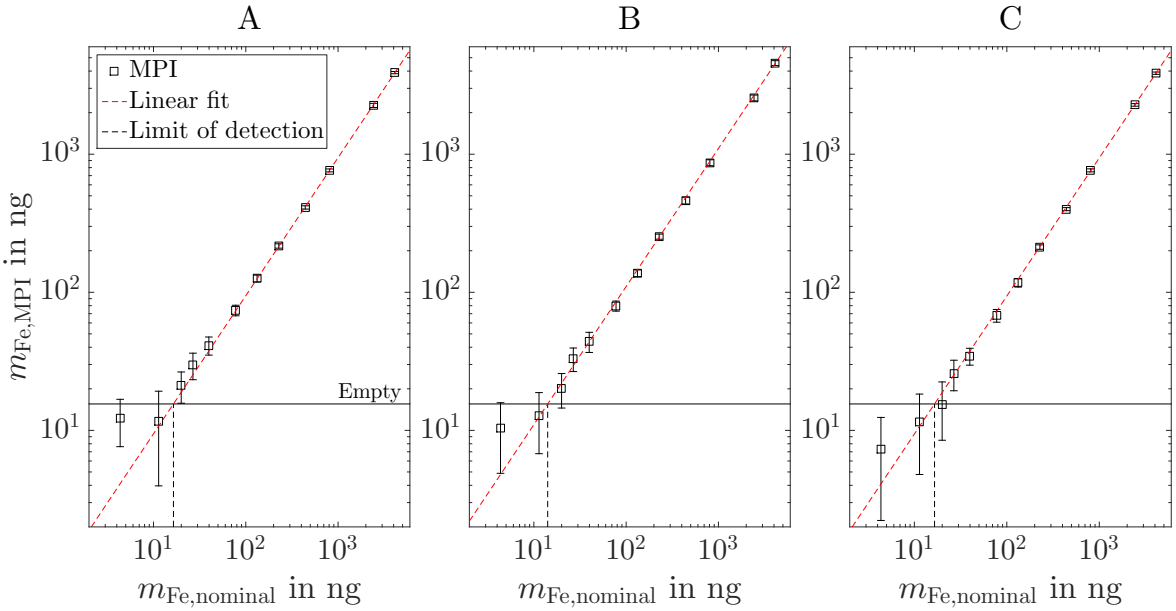

FIGURE 6.9: Quantified iron amounts extracted from MPI reconstructions displayed over the nominal iron amount of each sample. Displayed are mean values with the standard deviation presented as error bars for three measured positions A,B and C. The mean intensity of empty scanner measurements are shown as black horizontal lines and were used to determine the limit of detection of 16 ng. Compared to the nominal iron masses, an accuracy of $u_{c,MPI} = 8.8\,\%$ was achieved above the limit of quantification.

6.2.2 Iron concentration

The previous section 6.2.1 focused on measurements of samples, in which the total iron amount was concentrated in a small volume. Previous studies demonstrated, that the limit of detection might differ for diluted samples [38]. In the following, measurements using homogeneously diluted MNP samples with a larger volume were performed to obtain the limit of detection regarding the iron concentration c_{Fe} instead of the total iron mass. Samples were prepared using Ferucarbotran containing 160 µL in fast reaction tubes at iron concentrations ranging from 2.4 µmol/L to 0.18 mol/L (see figure 6.10). The sample volume was chosen to be compatible with MPS, for validation of the iron content, and MRI, for comparisons between MPI and MRI quantification (presented in section 6.3). Ten measurement repetitions were acquired for each sample at the center of the MPI FOV. The reconstruction parameters

were chosen following the procedure described by method 1 in section 6.1.4. A detailed list of measurement, SF and reconstruction parameters is given in A.3.

FIGURE 6.10: Photograph of one representative sample used for MPI and MRI measurements: Fast reaction tube filled with 160 µL Ferucarbotran diluted in water.

Qualitative analysis

Figure 6.11 displays MPI images of the phantom measurements for varying c_{Fe}. The color bars are normalized to the maximal intensity of each image respectively, for improved visibility of the large range of signal intensities. The red circles mark the nominal sample sizes and positions. A low amount of frequency components used in the reconstruction and a high regularization result in image blurring as described in sections 6.1.1 and 6.1.2 and an overestimation of the actual sample size. Qualitatively, no image quality degradations are observed for samples with $c_{\mathrm{Fe}} = 59.8\,\mu\mathrm{mol/L}$ or higher. Reconstructions for samples with lower c_{Fe} exhibit imaging artifacts and are disturbed by noise, due to the low MNP signal amplitudes, similar as described in section 6.2.1.

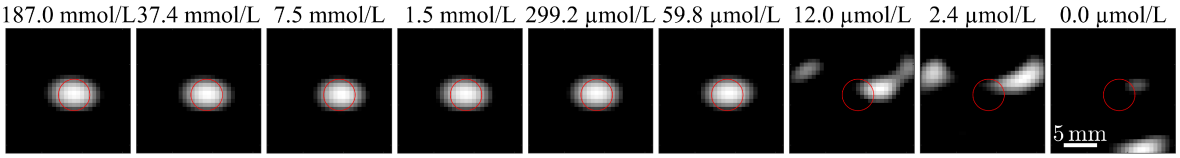

FIGURE 6.11: MPI images of diluted MNP samples with varying iron concentration. The color bars of each image are scaled by the maximal intensity respectively, since a common color bar would deteriorate the visibility. The red circles mark the nominal sample position. Reconstructions of samples containing $c_{\mathrm{Fe}} < 59.8\,\mu\mathrm{mol/L}$ are disturbed by imaging artifacts and a clear identification of the nominal MNP distribution is not possible.

Quantitative analysis

Quantification of $c_{\mathrm{Fe,MPI}}$ was performed using the intensities extracted from an ROI centered around the nominal sample position. Figure 6.12 displays averaged values of $c_{\mathrm{Fe,MPI}}$ with the standard deviations visualized as error bars. Similar analysis as presented in section 6.2.1 was performed and a response index $r = 0.98 \pm 0.01$, a limit of detection of $15.8\,\mu\mathrm{mol/L}$ and a relative combined standard uncertainty $u_{\mathrm{c,MPI}} = 8.7\,\%$ was determined, which is in good agreement with the previous results acquired using dot-phantoms.

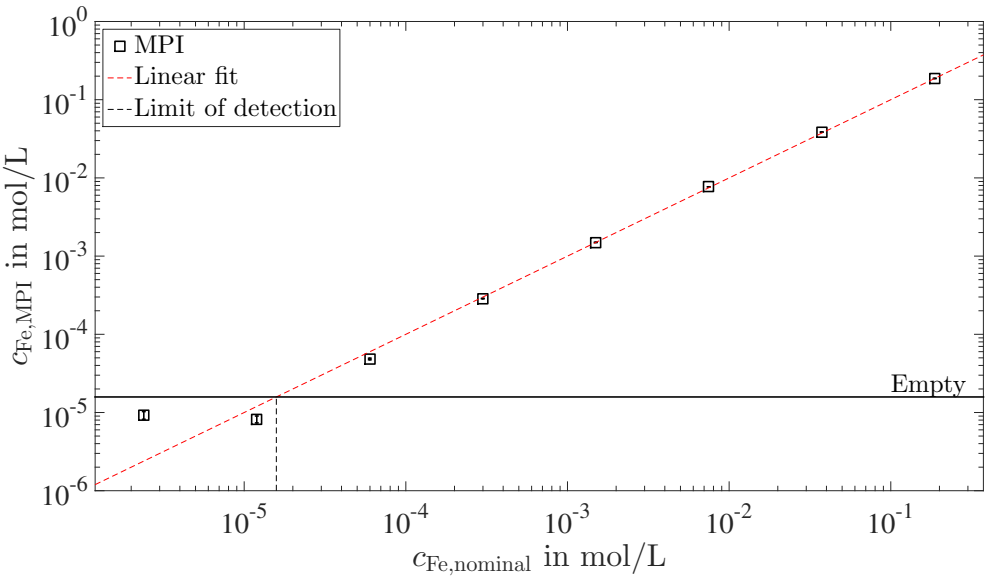

FIGURE 6.12: $c_{\mathrm{Fe,MPI}}$ displayed as a function of $c_{\mathrm{Fe,nominal}}$ of diluted MNP samples using pure water. Displayed are mean values with the standard deviation presented as error bars. The mean intensity acquired from empty scanner measurements is visualized as a horizontal line and was used to determine the limit of detection of 15.8 µmol/L. Compared to the nominal values an accuracy of $u_{\mathrm{c,MPI}} = 8.7\,\%$ was achieved by MPI above the limit of quantification.

6.3 MNP quantification using magnetic resonance imaging

There are multiple imaging techniques, which are capable of quantifying MNPs in biomedical applications [138, 139]. The most common modality regarding imaging and quantification of MNPs is MRI [140]. The physical basics of MRI and the influence of MNPs on the MRI signal are presented in section 2.3. There are fundamental differences between the principles of MPI and MRI concerning quantification of MNPs. In MPI, MNPs are the primary source of signal, making the signal directly proportional to the MNP amount. In MRI, MNPs are detected indirectly by their influence on the MRI signal decay. In the following, the advantages and disadvantages of both imaging techniques are investigated with the focus on quantification of MNPs. The characteristics of MPI quantification have been presented in section 6.2. Similar results are obtained for MRI and the two techniques are compared. In addition to MRI measurements, each sample is measured using an NMR system, which is based on the same physical principle as MRI without spatial encoding. The use of the NMR system provides a higher sensitivity compared to the MRI scanner, which enables measurements over a larger concentration range.

Finally, MRI and MPI measurements are repeated using MNP samples diluted in a copper sulfate ($CuSO_4$) solution to investigate the influence of the MNP environment and more realistic biological MRI relaxation times on the quantification. Partial results of this section have been published in HP3.

6.3.1 MNPs in pure water

The analysis presented in section 6.2.2 for MPI was repeated using MRI for the same samples. Since a minimal signal is required for the MRI system to obtain an image, the sample tubes were sealed and placed in a vessel filled with pure water. A multi-spin echo CPMG sequence was used to obtain a single imaging slice through the sample center. A detailed description of the sequence and how to extract the transverse relaxation rate (R_2) for quantification is presented in section 3.4 and a list of the MRI measurement parameters is given in table 6.1.

Parameter	Value
FOV	$80x40\,\mathrm{mm}^2$
Slice thickness	2.5 mm
Matrix size	128x64
Repetition time	1.5 s and 15 s
First echo time	5 ms and 75 ms
Number of echos	28
Total acquisition time	96 s and 16 min

TABLE 6.1: MRI measurement parameters used for determining R_2 for MNP quantification

The pulse sequence parameter TE was adapted between 5 ms and 75 ms for the measurements to cover the full exponential decay, depending on the iron concentration of the samples. In addition to the MRI measurements, NMR measurements were obtained by acquiring 2000 data points with varying TE between 0.04 ms and 3 ms (see section 3.3).

Qualitative analysis (MRI)

Figure 6.13 displays the MRI signal amplitude of diluted MNP samples inside a water bath for the measurement with the lowest echo time. The red circles mark the nominal sample sizes and positions. Signal changes induced by MNPs are observed only for samples containing $c_{\mathrm{Fe}} > 12\,\mu\mathrm{mol/L}$. Samples containing lower iron quantities show no significant contrast compared to pure water and could not have been identified without a priori knowledge of the sample position. Increasing c_{Fe} resulted in an increase of signal amplitude compared to pure water in the concentration range from about $12\,\mu\mathrm{mol/L}$ to $300\,\mu\mathrm{mol/L}$. This increase is mainly caused by shortening of the longitudinal relaxation time T_1 as described in section 2.3.3. Samples with $c_{\mathrm{Fe}} > 300\,\mu\mathrm{mol/L}$ show decreasing signal amplitudes due to shortening of the transverse relaxation time T_2 (see section 2.3.3). For iron concentrations $c_{\mathrm{Fe}} \geq 37.4\,\mathrm{mmol/L}$ imaging artifacts around the nominal sample positions appear, caused by magnetic field distortions in the vicinity of MNPs, complicating the localization of the nominal sample position.

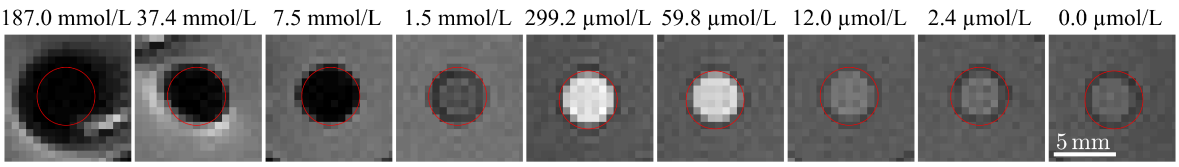

FIGURE 6.13: MRI amplitude images of MNP samples with varying c_{Fe} diluted with pure water. The samples were sealed and positioned inside a water bath to obtain sufficient signals. The red circles display the nominal sample positions. Samples containing $> 37.4\,\mathrm{mmol/L}$ induced imaging artifacts, complicating the sample localization. Below $c_{Fe} > 12\,\mu\mathrm{mol/L}$, no significant signal differences are observed between the MNP samples and the surrounding pure water.

The described behavior of the MRI signal amplitude in the stated MNP concentration ranges is only valid using Ferucarbotran and for the chosen measurement parameters and differs for other parameter settings or sequences, especially considering different MRI pulse sequence parameters (TE and TR), as described in section 2.3.3.

Qualitative comparison of MPI and MRI

MRI provides a higher spatial resolution and a larger, adjustable FOV compared to MPI. Signal is generated by the surrounding water, which would enable imaging of the anatomical structure simultaneously to MNP quantification in a biomedical application. On the other hand, this complicates the clear identification of MNPs, since their influence differs depending on the surrounding tissue, iron concentration and measurement parameters. Additionally, the signal changes induced by MNPs are hard to distinguish from other possible sources as changes of temperature, diffusion, oxygenation or imaging artifacts [141]. MPI on the other hand allows the imaging of MNPs with higher specificity and greater contrast since no background signals are generated by water, tissue or air.

Quantitative analysis (MRI)

Quantification of the iron concentration based on the MRI data was performed by extracting the transverse relaxation rate R_2 in ROIs around the nominal sample position, as described in section 3.4. These values were converted into the respective iron concentration using the determined relaxivity $r_2 = (136 \pm 3)\mathrm{Lmmol^{-1}s^{-1}}$, which is in good agreement with the literature values (see section 3.5.1). Figure 6.14 shows the results acquired from MRI and NMR measurements. A linear relationship of $c_{Fe,MRI}$ and $c_{Fe,nominal}$ was determined with a response index $r = 1.01 \pm 0.01$ (see section 2.4.1). An upper limit of detection of the MRI system is reached for samples containing $c_{Fe,nominal} > 1.5\,\mathrm{mmol/L}$ as not enough signal is received to determine R_2. Based on the higher sensitivity, the NMR system allows measurements of samples containing concentrations up to $0.187\,\mathrm{mol/L}$.

Below $c_{Fe,nominal} < 3.1\,\mu\mathrm{mol/L}$, no significant differences in $c_{Fe,MRI}$ were determined, since the measured R_2 reached the R_2 of pure water (visualized by a black horizontal line in figure 6.14). At these low iron concentrations, the field distortions caused by MNPs are not strong enough to cause a

measurable change in R_2. Therefore the lower limits of detection were determined to be 3.1 µmol/L for NMR and MRI.

A mean relative deviation of $(18 \pm 14)\,\%$ (mean±std) between NMR and MRI measurements was determined. These discrepancies are likely caused by the different magnetic field strengths of 1 T (MRI) and 1.5 T (NMR), which affect the spin dephasing and therefore the relaxation rate [105]. Comparing $c_{\mathrm{Fe,MRI}}$ and $c_{\mathrm{Fe,nominal}}$, resulted in a relative standard uncertainty of $u_{\mathrm{c,MRI}} = 16.8\,\%$ (see section 2.4.3).

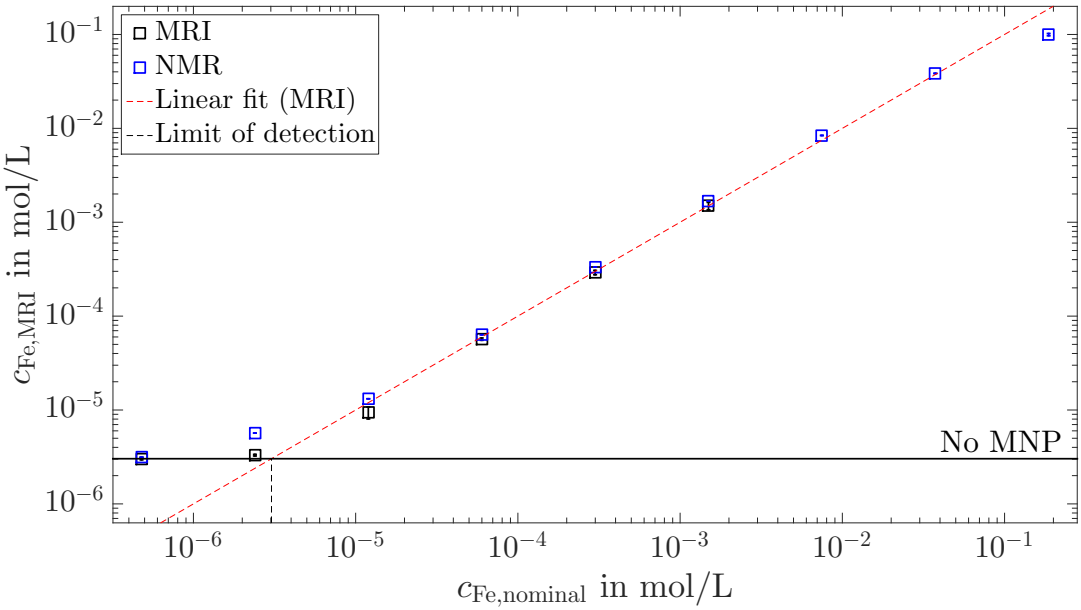

FIGURE 6.14: $c_{\mathrm{Fe,MRI}}$ determined for MNP samples with varying $c_{\mathrm{Fe,nominal}}$ diluted with pure water (MRI images shown in figure 6.13). The standard deviation is presented as error bars. The dotted line represents the linear fit determined using the MRI data. The black horizontal line visualizes the lower limit of detection of 3.1 µmol/L caused by the R_2 of the medium without the influence of MNPs. Additionally, an upper limit of detection of the MRI system is reached for 1.5 mmol/L, since no R_2 could be determined due to the fast signal decay. Quantification was achieved with an accuracy of $u_{\mathrm{c,MRI}} = 16.8\,\%$ above the limit of quantification.

Quantitative comparison of MPI and MRI

A main difference of MPI and MRI quantification is that MRI requires a reference scan without MNPs to subtract $R_{2,\mathrm{NoMNP}}$. This can be challenging, since additional scans are time demanding and multiple temporal changing parameters as temperature, oxygenation and diffusion rates might change and influence $R_{2,\mathrm{NoMNP}}$ [142–144]. Furthermore, physiological or pathological changes also affect $R_{2,\mathrm{NoMNP}}$, complicating the identification of the MNP effects and therefore the quantification [145, 146].

The linearity of the MPI signal and the transverse relaxation rate determined by MRI were verified by a response index in the linear regime $0.97 < r < 1.03$. MRI achieved worse quantification accuracy with a combined standard uncertainty twice as high compared to MPI. The limits of detection

are substantially different based on the different physical principle of MPI and MRI utilized for quantification. Since the MPI signal is directly proportional to the MNP amount, the lower limit of detection is mainly influenced by noise and background signals. An upper limit of detection is caused only by saturation of the low-noise amplifiers, which is reached for total iron masses of about 10 mg. These amounts are far above the dosage used for biomedical applications and are neglected in the further discussion.

Since MRI quantification is based on the influence of MNPs on the MRI signal, every other factor, influencing the MRI signal, also affects the limit of detection. The limit of detection for low MNP concentrations is reached when no difference of R_2 and $R_{2,\mathrm{NoMNP}}$ is detected. Therefore, the limit of detection of MRI is highly dependent on $R_{2,\mathrm{NoMNP}}$ and thus the MNP environment. Using pure water, the limit of detection of MRI is 5-fold lower compared to MPI. Section 6.3.2 presents results obtained by MRI measurements with more realistic biological relaxation times. The upper limit of detection of MRI is caused by the increasing signal decay caused by MNPs. At a certain MNP concentration, the signal decay is too rapid and a determination of R_2 is not possible. This limit is mainly dependent on the sensitivity of the measurement system and the chosen measurement parameters, especially TE. The minimal TE of the used MRI system is 5 ms. Decreasing TE further would allow the detection of higher concentrated samples. UTE (ultrashort echo time) sequences are utilized to measure concentrations up to several tens of mmol/L [89, 147]. However, a compromise between shorter TEs and a downgrade in spatial/temporal resolution or SNR has to be made.

6.3.2 MNPs in copper sulfate solution

This section investigates the influence of the local MNP environment on the MPI and MRI/NMR quantification (objective three). There are several environmental factors that affect the MPI or MRI signals. Here, only one well-controlled representative example is analyzed to demonstrate the impact on the quantitative results. Detailed studies on the influence of multiple parameters (ph-value, ionic strength, complex media, etc.) on the MPI raw signal are given in [62, 148].

MNP samples at identical iron concentration as used for the experiments presented in sections 6.2.2 and 6.3.1 were prepared using a copper sulfate ($CuSO_4$) solution instead of pure water. A $CuSO_4$ concentration of 27 mmol/L was chosen, to mimic the MR relaxation times of liver tissue [149]. The measurements and the post-processing steps were identical to the previous analysis of water samples. Especially, the same calibration measurements were used to determine the iron concentrations using MPI and MRI, deliberately ignoring the fact of the changed MNP environment to test the influence on the quantitative results.

Qualitative analysis

Figure 6.15 shows the MPI (a) and MRI (b) images of copper sulfate samples with varying $c_{\mathrm{Fe,nominal}}$. No major image quality degradations are observed using MPI for samples containing

$c_{\mathrm{Fe,nominal}} \geq 299.2\,\mu\mathrm{mol/L}$ compared to samples containing pure water. Imaging artifacts and distortions are visible for $c_{\mathrm{Fe,nominal}} = 59.8\,\mu\mathrm{mol/L}$ instead of $c_{\mathrm{Fe,nominal}} = 12\,\mu\mathrm{mol/L}$ as it was observed for pure water. Possible reasons for these effects are discussed in the quantitative analysis.

Samples containing pure $CuSO_4$-solution show stronger MRI signals compared to pure water, caused mainly by a shorter longitudinal relaxation time. Increasing $c_{\mathrm{Fe,nominal}}$ has no significant effect on the MRI signal below $1.5\,\mathrm{mmol/L}$. For higher concentrated samples the signals decrease and image artifacts are visible similar as observed before for pure water samples.

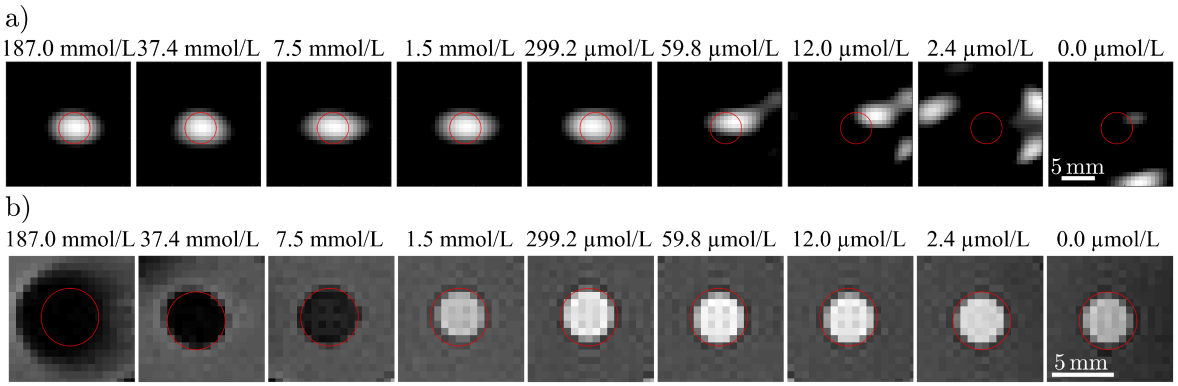

FIGURE 6.15: MNP samples diluted in $CuSO_4$-solution imaged by MPI (a) and MRI (b). The nominal sample positions are visualized by red circles. The color bars of the MPI images were normalized individually by the maximal intensity of each image for improved visibility. Imaging artifacts hamper a clear localization of the sample positions for concentrations below $59.8\,\mu\mathrm{mol/L}$ in MPI and above $37.4\,\mathrm{mmol/L}$ in MRI.

Quantitative analysis

Figure 6.16 displays $c_{\mathrm{Fe,MPI}}$ (a) and $c_{\mathrm{Fe,MRI}}$ (b) for varying $c_{\mathrm{Fe,nominal}}$. The values acquired from the previous experiments performed in sections 6.2.2 and 6.3.1 using samples diluted in pure water are shown to visualize the differences caused by the changed MNP environment. The limit of detection of MPI increased by a factor of 3 to $47.5\,\mu\mathrm{mol/L}$. Comparing $c_{\mathrm{Fe,MPI}}$ and $c_{\mathrm{Fe,nominal}}$ to determine the quantification accuracy of MPI resulted in a value of 56.9 %, which is significantly worse compared to the values obtained for pure water. In addition, deviations from a pure linear relationship between $c_{\mathrm{Fe,MPI}}$ and $c_{\mathrm{Fe,nominal}}$ are observed. These changes could be caused by MNP agglomeration induced by the additional ions of the $CuSO_4$-solution, changing the dynamic magnetic behavior [62, 150]. This results in a mismatch of the acquired MPI raw signals and the signals of the SF used for reconstruction, acquired with a MNP sample diluted in pure water. A possible way for correcting these deviations is to acquire a new SF using a sample with matching environmental conditions, which is demonstrated in chapter 7.

The MRI results show an about 80-fold higher limit of detection of $0.25\,\mathrm{mmol/L}$ compared to pure water. This is mainly caused by a lower transverse relaxation time of $CuSO_4$ (60 ms) compared to pure water (2400 ms). Only one data point was acquired for MRI above the limit of detection. For this

reason, the NMR measurement data were used for the further analysis. The quantification accuracy of MRI was determined to be 44.8 %, which is also much higher compared to pure water. The observed effects could also be explained by MNP agglomeration. Detailed studies about the effect of particle agglomeration on the NMR/MRI signal are given in [151, 152]. A possibility for correcting these signal changes would be to use a corrected value of the relaxivity.

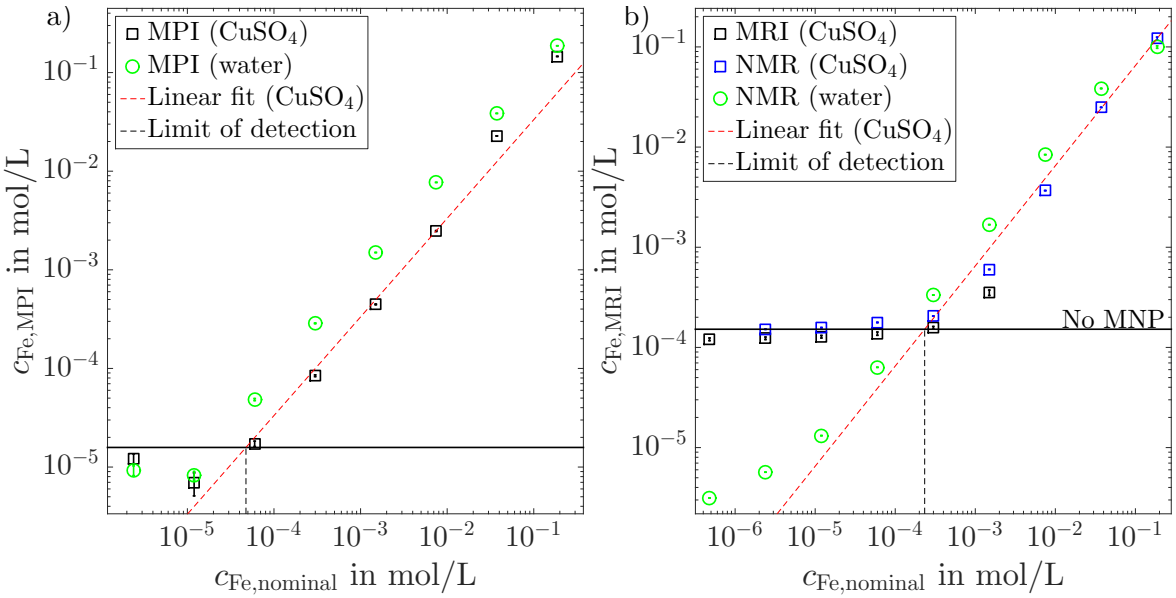

FIGURE 6.16: a) $c_{Fe,MPI}$ displayed as a function of $c_{Fe,nominal}$ acquired from samples diluted in pure water and $CuSO_4$-solution. Shown are mean values with the standard deviation presented as error bars. For the $CuSO_4$-samples, the limit of detection of 47.5 µmol/L was determined based on empty scanner measurements (black horizontal line). The accuracy of MPI quantification in $CuSO_4$-solution was determined to be 56.9 %. b) $c_{Fe,MRI}$ of the same samples determined by MRI and NMR. The black horizontal line visualize the lower limit of detection of 0.25 mmol/L caused by the R_2 of the surrounding $CuSO_4$-solution without the influence of MNPs. Above 1.5 mmol/L, no MRI data could be acquired due to the fast signal decay. The MRI quantification accuracy for MNP samples in $CuSO_4$-solution was determined to be 44.8 %.

6.4 Quantitative Imaging: Summary and discussion

This chapter focused on extracting quantitative information about the MNP amount from reconstructed MPI images. In the first step, the influence of the image reconstruction was investigated. The variation of each reconstruction parameters showed big qualitative and quantitative influence. Since the currently most common method for choosing these parameters is based on a visual inspection of the reconstruction results, this strongly affects the quantification accuracy. To overcome this problem, a method was presented, which corrects these quantitative deviations by rescaling the image intensities with an additional reference measurement. This method was used to obtain the results of the phantom studies presented in this chapter. An additional method focused around multi-color MPI was presented, which is utilized in chapter 7.

Phantom studies were performed to test the MPI imaging and quantification performance. The localization of MNPs was demonstrated for dot-phantoms with varying iron masses down to 20 ng. The linearity of the MPI signal intensities is a key requirement for quantification and was verified by a response index of $r_{\mathrm{MPI}} = 1.02 \pm 0.02$ for samples above the limit of detection of 16 ng. The combined standard uncertainty of $u_{\mathrm{c,MPI}} = 8.8\,\%$ was determined as a measure for the quantification accuracy. Similar accuracies were determined by analyzing the MPI raw signals (see section 5.2). The strongest influence for the limit of detection and the quantification accuracy was noise and background signals, discussed in section 4.2. Further improvements in terms of sensitivity and accuracy could be made by minimizing the remaining influence of background signals on the MPI raw signal after background correction, discussed in section 4.3.

Based on the insights gained from the MPI raw signal characterization (see chapter 4), only the data acquired by the Rx-coil was used for image reconstruction. The same analysis was performed using the x-TxRx-coil instead, resulting in a higher limit of detection of 133 ng and a combined standard uncertainty of 23.6 %, demonstrating the improvements gained by the gradiometric design of the Rx-coil (see HP2 for more details). The limit of detection determined in this work agrees with values found in published literature. Graeser et al. presented results with a limit of detection of 5 ng, using also a gradiometric coil [38]. The about 3-fold lower limit of detection was mainly caused by a smaller coil diameter and the use of an optimized MPI particle system (LS-008) [37].

Comparisons of the MPI quantification accuracy are complicated by incoherent definitions of accuracy in the published literature (see section 2.4.3). Several studies present a linear dependency of the MPI signal intensity with the MNP amount and state the coefficient of determination obtained from a linear fit (R^2) [21, 114, 153, 154]. But this linear dependency is not sufficient to make statements about the accuracy. Zheng et al. reported an uncertainty of 8.2 % for MPI quantification in comparison to iron quantification performed with inductively coupled plasma (ICP) measurements, which is in close agreement to the accuracy determined in this work [24].

The presented quantification results were obtained using dot-like phantoms. In reality, the spatial distributions of MNPs inside a patient are more complex, which complicates the image reconstruction and the quantitative analysis. Thus, the reported limit of detections and accuracies represent lower limits and might be worse for more complex spatial distributions of MNPs.

The effect of MNP dilution was studied, showing no major effect on the signal linearity and quantification accuracy. The limit of detection in terms of iron concentration of 15.8 µmol/L was determined. The same samples were measured using MRI, investigating the differences and advantages/disadvantages of MRI and MPI focusing on MNP quantification. MRI provides larger FOVs, higher spatial resolution compared to MPI and simultaneous acquisition of anatomical information in the image. The identification of MNPs in an MRI image is more difficult, as the effects of MNPs on the MRI signal are hard to distinguish from other sources (air, imaging artifacts, inhomogeneous media, etc.). A major disadvantage of MRI quantification based on R_2 is that reference scans before MNP injection are required. This takes additional time and is prone to errors due to temporal varying parameters, which influence R_2. In addition, the linear dynamic range is highly dependent on the

initial R_2 of the medium. Using pure water, quantification was possible in the concentration range $3.1\,\mu\text{mol/L} < c_{\text{Fe}} < 1.5\,\text{mmol/L}$ based on a linear relationship between R_2 and c_{Fe} verified by a response index of $r_{\text{MRI}} = 1.01 \pm 0.01$. Performing the same measurements in a $CuSO_4$-solution, resulted in a lower limit of detection of $0.25\,\text{mmol/L}$. The upper limit of detection is mainly determined by measurement parameters and system sensitivity and could be increased using specially designed sequences in exchange for a lower spatial/temporal resolution. The accuracy of MRI quantification was determined by the combined standard uncertainty of 16.8 %.

During the last decade, other techniques for MNP quantification based on MRI have been reported. These techniques are based on susceptibility measurements and might provide a way to overcome the weaknesses of MRI quantification as no reference scans are needed [88, 155]. In conclusion, the main advantages of MPI are high specificity and high contrast for imaging of MNPs, while MRI provides higher spatial resolution and anatomical background information. These features make them especially interesting for complementary measurements using both techniques [114].

Finally, the influence of the MNP environment on MPI and MRI quantification was investigated for one representative example in a phantom study using a $CuSO_4$-solution. The additional ions in the solution changed the dynamic magnetic behavior of the MNP samples with measurable effects in both MRI and MPI. These effects were likely caused by particle agglomeration and resulted in deteriorated quantification accuracies of 56.9 % and 44.8 % for MPI and MRI [62, 150–152]. Methods for correcting these deviations are presented in more detail in the following chapter 7.

Chapter 7

MPI quantification in a biological environment

This chapter presents my investigations focusing on objective three, the influence of the MNP environment on quantitative MPI and additionally demonstrates a possible biomedical application of quantitative MPI. Section 6.3.2 already demonstrated, that the MNP environment has strong influence on the MPI signals, which leads to quantification errors. For biomedical applications, changing environmental conditions are inevitable and thus need to be considered for accurate quantification. Environmental factors that need to be considered include macroscopic parameters (temperature, viscosity, etc.) and microscopic parameters (MNP immobilization, agglomeration, etc.). In the following, in particular MNPs interacting with living cells are investigated.

Cellular MPI is of high interest for several biomedical applications such as cell tracking or diagnosis of inflammatory diseases and cancer [25, 31, 154, 156]. Previous studies characterized magnetic signal changes of MNPs interacting with living cells [58, 62, 64, 157–160]. These effects are caused by several factors including MNP aggregation, "size-filtering" during the cellular uptake and increasing dipole-dipole interactions due to a smaller distance and decreased mobility of the MNPs. In most cases, these signal changes result in a deterioration of the MPI image quality and quantification errors. Section 7.1 focuses on the possibility to incorporate these signal changes in the MPI image reconstruction by using multi-color MPI (see section 2.2.3). The incorporation not only prevents image quality degradations but also allows the extraction of information about the MNP environment. This feature is utilized in combination with the high temporal resolution of MPI to demonstrate the potential for imaging and quantification of MNPs interacting with living cells in section 7.2. Although the experiments are focused on MNPs interacting with cells, the fundamental principle can easily be adapted to include the influence of other environmental factors.

7.1 Cellular MPI

The incorporation of the influence of the MNP environment in the MPI image reconstruction is achieved by adapting the SF. In general, the SF is determined experimentally and the local environmental conditions of the MNPs are fixed to the conditions present during the acquisition. Inclusion of different

environmental conditions in the MPI image reconstruction is achieved by acquiring additional SFs with adapted conditions (e.g. MNP immobilization, aggregation, temperature, etc.) and combining them for reconstruction as presented in section 2.2.3. This so called multi-color MPI not only reduces the occurrence of imaging artifacts and quantification errors but also allows to gain information about the MNP environment. Previous studies utilized multi-color MPI to distinguish between different MNP types in a mixed sample, and for quantification of temperature and viscosity based on MPI images [79–81]. Here, the technique is adapted with the focus on cellular MPI. The performance of multi-color MPI for cell imaging is compared to "conventional" MPI using only a single SF based on a phantom experiment.

Sample preparation

Two kind of samples were prepared; Samples containing MNPs diluted in water and samples containing MNPs uptaken by human acute monocytic leukemia (THP-1) cells. This cell line is commonly used to study macrophage-associated diseases [157, 161]. Since the MNPs diluted with water are free to move and rotate, they will be referred to as "free" samples. By definition the term "cell-bound" MNPs includes each MNPs that is internalized or adsorbed by the outer cell membrane of THP-1 cells. The MNP type Synomag (see section 3.5.2) was chosen because of the high MPI signal generation and good uptake performance by THP-1 cells.

The cell cultivation and preparation of the samples was performed in cooperation with Charité Berlin. Human acute monocytic leukemia cells (THP-1 cells, ATCC Wesel, Germany) were cultured in suspension in a humidified incubator at 37°C with a 5% CO_2 concentration in RPMI medium 1640 (Invitrogen, Karlsruhe, Germany). The culture medium was supplemented with 10% fetal calf serum (Biochrom, Berlin, Germany), 100 U/mL penicillin, 100 mg/L streptomycin (Invitrogen, Karlsruhe, Germany) and 2 mmol/L L-glutamine (Invitrogen, Karlsruhe, Germany). A hemocytometer was used to determine the number of cells. Samples including MNPs were prepared in the following way: THP-1 cells suspended in RPMI (cell concentration: 10^6/mL) containing 1% fetal calf serum were incubated with Synomag at an iron concentration of 0.5 mmol/L. Afterwards, the samples were centrifuged for 3 min at 200 g, leading to sedimentation of cells and the supernatant were removed. The remaining cell pellet was washed three times with PBS and centrifuged for 3 min at 200 g, to remove unbound MNPs. After MPI measurements, the iron mass of each sample was determined using colorimetric measurements based on the 1,10-phenanthroline-based iron assay method as described in [161].

MPI measurement setup

Two SFs were measured using a free (SF_{free}, 8 µL in a cubic 2 mm^3 container, $c_{Fe} = 107$ mmol/L diluted in water) and cell sample (SF_{cell}, $2 \cdot 10^6$ THP-1 cells loaded with Synomag in a cubic 2 mm^3 container), respectively. The influence of different SFs on MPI quantification was analyzed by performing three phantom measurements (A, B and C). In measurement A and B, two individual phantoms containing 10 µL ($c_{Fe} = 21.5$ mmol/L, $m_{Fe,free} = 12$ µg) and 10^6 THP-1 cells loaded with Synomag

($m_{\mathrm{Fe,cell}} = 13.1\,\mu\mathrm{g}$) were used. In measurement C, both samples were positioned at a distance of 2 cm next to each other. Each measurement was reconstructed using "conventional" MPI-reconstruction using the SFs $\mathrm{SF_{free}}$ and $\mathrm{SF_{cell}}$ respectively. Additionally, both SFs were combined and used for a multi-color MPI reconstruction, which results in two particle distributions representing the free and cell-bound MNPs. The reconstruction parameters for the multi-color approach were chosen as described by method 2 in section 6.1.4. The same parameters were used for the reconstructions using only a single SF. A list of the measurement, SF and reconstruction parameters is given in A.4.

Qualitative results

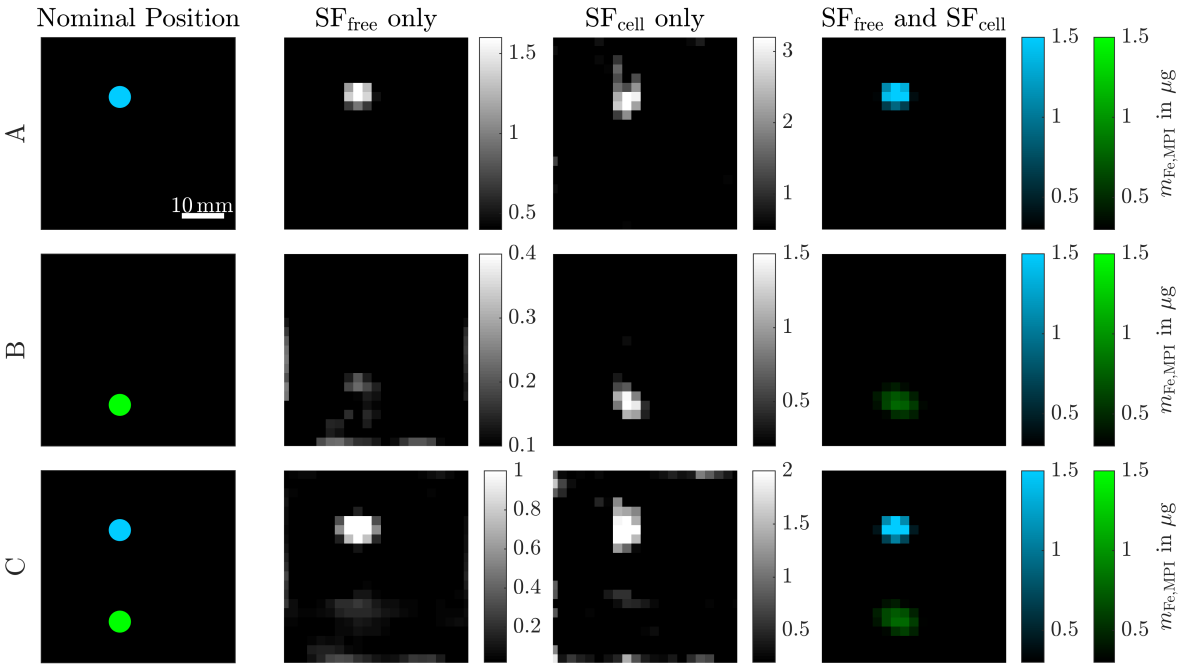

FIGURE 7.1: MPI images for three different phantom measurements. The first column displays the nominal distributions of free (blue) and cell-bound (green) MNPs. In measurement A and B, a single sample containing MNPs diluted in water (free) or MNPs internalized by THP-1 cells (cell) was measured, respectively. In measurement C both samples were positioned at a distance of 2 cm inside the FOV. Each measurement was reconstructed using a SF acquired by a free and cell sample respectively. Additionally, both SFs were combined to perform a third reconstruction using the multi-color approach, which yields two MNP distributions. These two were combined in one image and represent the free- (visualized by a blue color bar) and cell-associated (green color bar) MNP distributions.

Figure 7.1 displays the nominal phantom positions and the MPI results for measurement A, B and C using different SFs. The reconstructed images determined using a single SF ("conventional" MPI) show good qualitative agreement with the nominal MNP distributions only if the MNP conditions match to the conditions of the SF (measurement A for $\mathrm{SF_{free}}$ and measurement B for $\mathrm{SF_{cell}}$). For phantoms containing MNPs with non-matching conditions, image distortions in the form of blurring or artifacts are observed. These effects are caused by magnetic signal patterns, that are not included in

the SF and thus are not reconstructed accurately, as already described in section 6.3.2. Overall, the reconstructed signal intensities of the cell samples are lower compared to the free sample, although the MNP content of both samples is similar (9 % difference). This is likely related to lower signals generated by MNPs internalized by cells [64].

The two MNP distributions calculated by the multi-color reconstruction are displayed in a single image using individual color bars to represent the distribution of free MNPs (blue) and cell-bound MNPs (green). The results show good qualitative agreement between the nominal distribution and the reconstruction results for measurement A, B and C. No imaging artifacts or distortions are observed, since the required magnetic signal patterns are included in the combined SF. The results demonstrate that multi-color reconstruction not only yields the spatial distribution of MNPs but also allows the differentiation between free and cell-bound MNPs, based on the different magnetic signal patterns generated by these MNPs.

Quantitative results

Figure 7.2 displays the deviation of $m_{\mathrm{Fe,MPI}}$, extracted in ROIs centered around the sample positions, from the nominal iron mass $m_{\mathrm{Fe,ref}}$ determined by the colorimetric measurements.

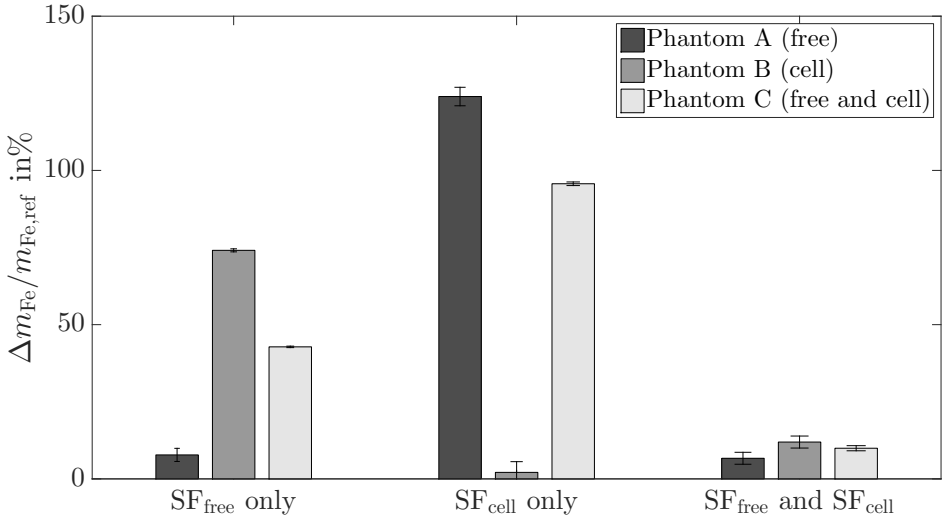

FIGURE 7.2: Relative deviation of the MPI determined iron mass ($m_{\mathrm{Fe,MPI}}$), extracted in ROIs for each measurement presented in figure 7.1, compared to the nominal iron mass determined colorimetrically using the 1,10-phenanthroline-based iron assay ($m_{\mathrm{Fe,ref}}$). Presented are mean values of 10 measurement repetitions with the standard deviation visualized as error bars. Big deviations are observed for "conventional" MPI using a single SF if the environmental conditions during the measurement and the SF acquisition are not similar. Multi-color MPI yields much smaller deviations of below 12 % in each case.

The results obtained by "conventional" MPI yields small deviations below 10 % only, if the environmental conditions of the MNPs in the phantom match with the environmental conditions of the SF, agreeing with the results presented in section 6.2. If only or additional MNPs at different

conditions were measured, high deviations between $42-124\,\%$ were determined, as already described for the results of the $CuSO_4$-measurements in section 6.3.2. These big deviations are caused mainly by magnetic signal patterns, that are not included in the SF and thus are not recognized correctly in the image reconstruction. The multi-color approach includes the signal patterns of both, free and cell-bound MNPs. Therefore, much smaller deviations of $12\,\%$ or lower were determined for phantom A, B and C.

7.2 In-vitro quantification of cellular uptake

The results of the previous section 7.1 showed that the multi-color reconstruction improves the image quality, allows accurate quantification and additionally provides information about the MNP environment. Especially the ability to distinguish between free and cell-bound MNPs combined with the possibility for quantification and the high temporal resolution of MPI offers interesting opportunities for biomedical applications and is analyzed in more detail in this section.

In diseased tissue, MNPs accumulate preferentially in macrophages as a result of leaky vasculature [161–166]. These phagocytic cells are a hallmark of tissue inflammation and their quantity is considered a marker of the severity of the disease [167–169]. Thus, a quantification of the MNPs uptaken by these kind of cells provides diagnostically relevant information. The cellular uptake mechanism is complex and a complete understanding of the processes involved is highly interesting since it is assumed that the uptake dynamics correlate with pathological changes of diseased tissue. This section investigates, if MPI is capable of imaging and quantification of the internalization of MNPs in living THP-1 cells. Information gained by analyzing the uptake kinetics of MNPs is not only beneficial to support fundamental biological research, but might also offer opportunities for future diagnostic purposes.

The results of multiple measurements are presented to test the hypothesis that MPI is able to image and quantify the cellular uptake of MNPs into cells. First, light microscopy measurements of THP-1 cells treated with Synomag were acquired to verify the rapid internalization of MNPs. Second, colorimetric measurements of samples with varying incubation times were performed to determine the dynamic uptake behavior. Third, MPS measurements were used to identify changes of the dynamic magnetic behavior of the MNPs during the cellular uptake, which is the prerequisite to distinguish these states using MPI. Finally, in-vitro MPI measurements were performed, in which MNPs and living cells were brought into initial contact during an MPI measurement. A summary and a detailed discussion of the results are given in section 7.3. Partial results of this section have been published in HP4.

7.2.1 Light microscopy

Images of THP-1 cells incubated with Synomag were obtained to localize the MNPs after short incubation times within the THP-1 cells.

Experimental setup

THP-1 cells were cultivated for 15 min with Synomag, using the same procedure as described in the previous section 7.1. After treatment, the samples were washed and prepared on glass slides. Iron contents of the samples were visualized by Prussian blue staining (2 % potassium ferrofyanida in 1 % HCL) followed by counterstain with Nuclear Fast Red. Light microscopy images were acquired for two samples, treated with and without MNPs.

Results

Figure 7.3 displays representative light microscopy images of THP-1 cells without (a) and with (b) treatment with MNPs. No visual iron was determine in samples treated without MNPs. For samples incubated with Synomag for 15 min, blue stained iron is visible attached to the outer cell membrane and inside the cytoplasm of the THP-1 cells verifying the internalization of MNPs after about 15 min.

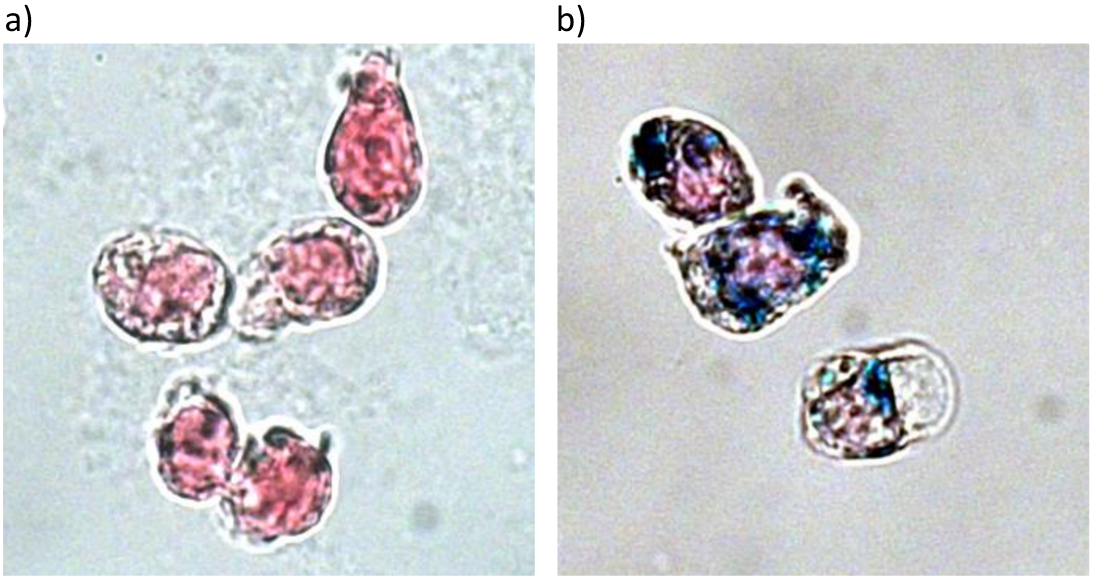

FIGURE 7.3: Light microscopy images of THP-1 cells treated without (a) and with Synomag for 15 min (b). Internalized MNPs were visualized by Prussian blue staining followed by counterstain with Nuclear Fast Red, indicating a rapid uptake of Synomag.

7.2.2 Colorimetric iron determination

The dynamic uptake behavior of Synomag into THP-1 cells was analyzed by performing colorimetric measurements of the iron content of samples with varying incubation time. Colorimetric measurements are commonly used to acquire quantitative data about the cell-associated MNP content and are here used as reference values, which are compared to the MPI results presented in section 7.2.4.

Experimental setup

A varying number of THP-1 cells, ranging from 0 to 10^6, were suspended in 100 µL PBS at room temperature. 40 µL Synomag at an iron concentration of $c_{\mathrm{Fe}} = 50\,\mathrm{mmol/L}$ was added to the solution. After $0/5/10/20/30\,\mathrm{min}$, free and cell-bound MNPs were separated. This was achieved by washing the samples twice with PBS and centrifugation for three minutes at 200 g. The supernatants were collected and evaporated to dryness using a Speedvac (Savant Instrumenty, NY, USA). The iron contents of the supernatant and the remaining cell pellet, representing the free ($m_{\mathrm{Fe,ref,free}}$) and cell-bound ($m_{\mathrm{Fe,ref,cell}}$) MNP fractions respectively, were determined using the 1,10-phenanthroline-based iron assay as described in [161]. This procedure was repeated to collect a total of three independent measurement data sets used for averaging. Due to possible losses of some MNPs during the required washing steps, the deviation of the total iron mass was investigated, which was calculated as $\Delta m_{\mathrm{Fe,ref}} = \frac{(m_{\mathrm{Fe,ref,free}} + m_{\mathrm{Fe,ref,cell}}) - m_{\mathrm{Fe,0}}}{m_{\mathrm{Fe,0}}}$.

Results

Figure 7.4 shows $m_{\mathrm{Fe,ref,free}}$ (a) and $m_{\mathrm{Fe,ref,cell}}$ (b) over time, acquired from the colorimetric measurements. Each data point represents the averaged value acquired from three independent samples with the standard deviation presented as error bars.

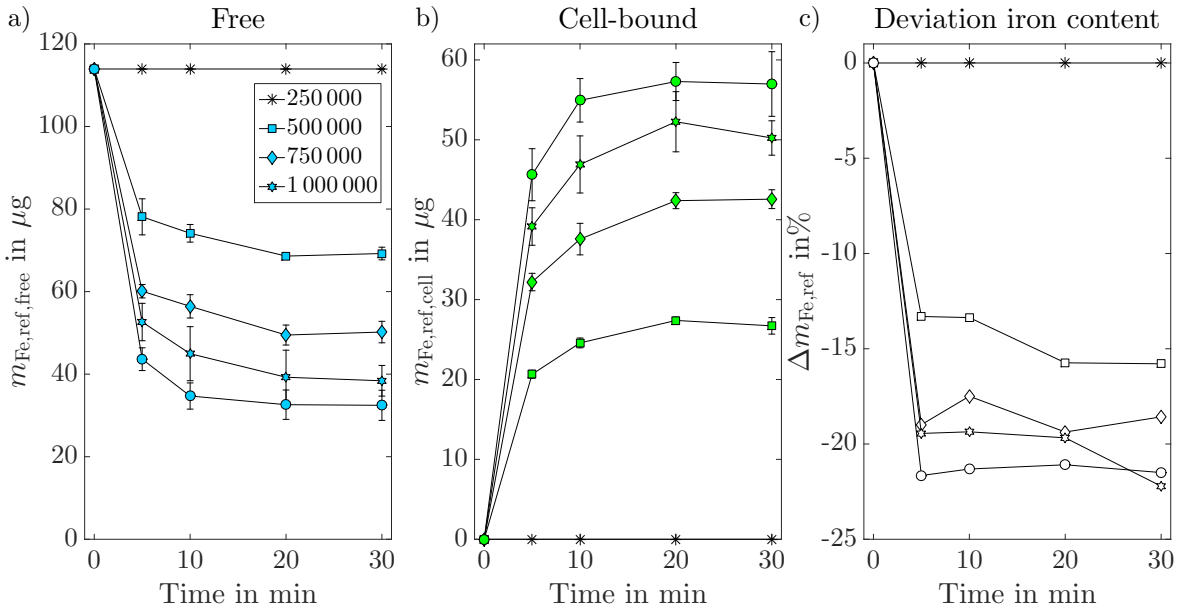

FIGURE 7.4: Quantified iron mass of free (a) and cell-bound (b) MNPs determined by the phenanthroline-based iron assay for varying incubation times. Shown are mean values of three independent measurements with the standard deviation visualized as error bars. Decreasing amounts of free and increasing amounts of cell-bound MNPs verify the fast internalization of MNPs into THP-1 cells. c) displays the relative deviation of the total iron mass, which was likely caused by losses during required washing steps needed for the phenanthroline based iron assay. The lines connecting the dots are only shown for improved visibility and do not represent measurement data.

$m_{\text{Fe,ref,free}}$ decreased and $m_{\text{Fe,ref,cell}}$ increased over time until saturation was reached for fully loaded cells after about $10-15\,\text{min}$, agreeing with the assumption that MNPs are accumulating inside the cells and with the results acquired by light microscopy presented in section 7.2.1.

Figure 7.4 c) displays the relative deviation of the total iron amount $\Delta m_{\text{Fe,ref}}$. The total iron amount, determined by the colorimetric measurements, was underestimated with deviations from the nominal iron mass of up to $-22\,\%$. These deviations were likely caused by losses of the supernatant (contributing to the free MNPs) during the washing steps required in the phenanthroline-based iron assay. No deviations were determined for the sample without cells, since no washing steps were required to separate free and cell-bound MNPs.

7.2.3 In-vitro MPS

In-vitro measurements were performed using MPS to analyze if magnetic signal changes are detected during cellular uptake. These changes of the dynamic magnetic behavior form the basis for the ability to differentiate states of the uptake process in the MPI image reconstruction.

Experimental setup

A sample was prepared containing $40\,\mu\text{L}$ Synomag diluted in phosphate-buffered saline (PBS) at an iron concentration of $c_{\text{Fe}} = 50\,\text{mmol/L}$. A varying number of THP-1 cells in the range $0-10^6$ were suspended in $100\,\mu\text{L}$ PBS respectively, drawn up into a syringe and connected with a tube to the sample. Figure 7.5 displays a schematic diagram of the experiment.

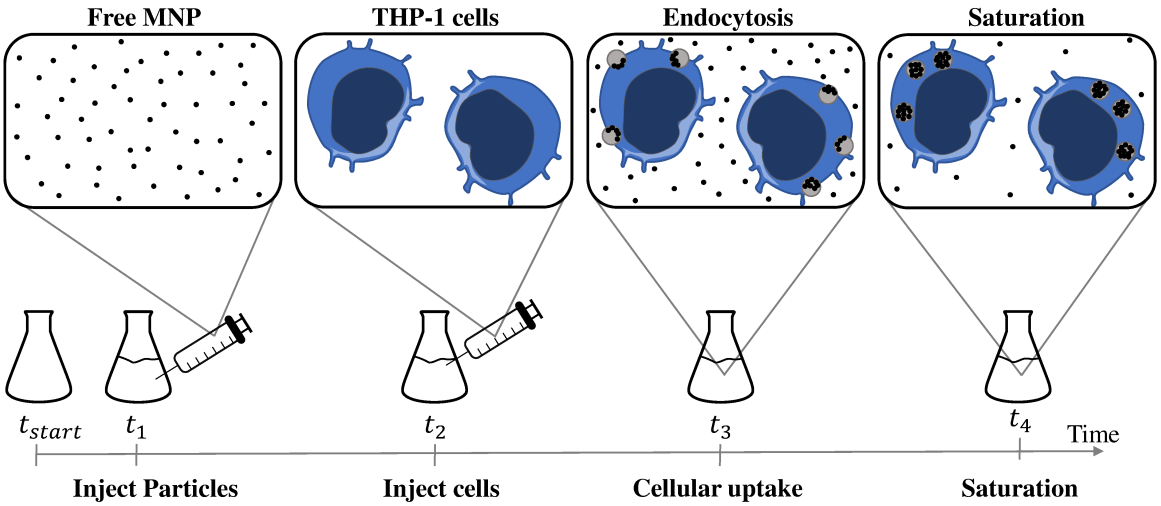

FIGURE 7.5: Schematic diagram of the MPS/MPI in-vitro experiments performed using Synomag and THP-1 cells. The MPS or MPI (see section 7.2.4) measurements of the empty scanner are started at t_{start}, which are used for background correction. Synomag, diluted in PBS, is placed inside the system during the measurement at time t_1. THP-1 cells, diluted in PBS, are injected on top of the MNPs at time t_2, which is defined as $t_2 := 0$. Continuous MPS/MPI measurements are performed, while the MNPs are internalized by the cells until saturation is reached (t_3 to t_4).

Consecutive MPS measurements at an amplitude of 12 mT were performed with a temporal resolution of 4 s starting from time point t_{start}, measuring the empty scanner. These data were used for background correction as described in section 4.2.3. After 30 s, the sample containing MNPs diluted in PBS was moved inside the measurement chamber (t_1). After additional 60 s, the cells diluted in PBS were added to the MNPs (t_2 defined to be $t_2 := 0$). The cellular uptake (endocytosis) starts directly from MNP-cell contact until the cells are fully saturated by MNPs (t_3 to t_4) [166].

Results

Figure 7.6 displays the ratio between the fifth and third harmonic $|\hat{u}_5|/|\hat{u}_3|$, which is used to determine changes of the magnetic characteristics of the MNP ensemble, as a function of time. Before injection of cells, MNPs diluted in PBS were measured and a constant $|\hat{u}_5|/|\hat{u}_3| = 20.1\,\%$ was determined for each sample, representing free MNPs, which are visualized by a blue marker color in figure 7.6. The control experiment, performed by injecting PBS, shows no significant influence on $|\hat{u}_5|/|\hat{u}_3|$, except a small decrease of about 0.6 %. This decrease might be caused by the larger volume of the measured sample in combination with the inhomogeneous sensitivity profile of the MPS receive coil.

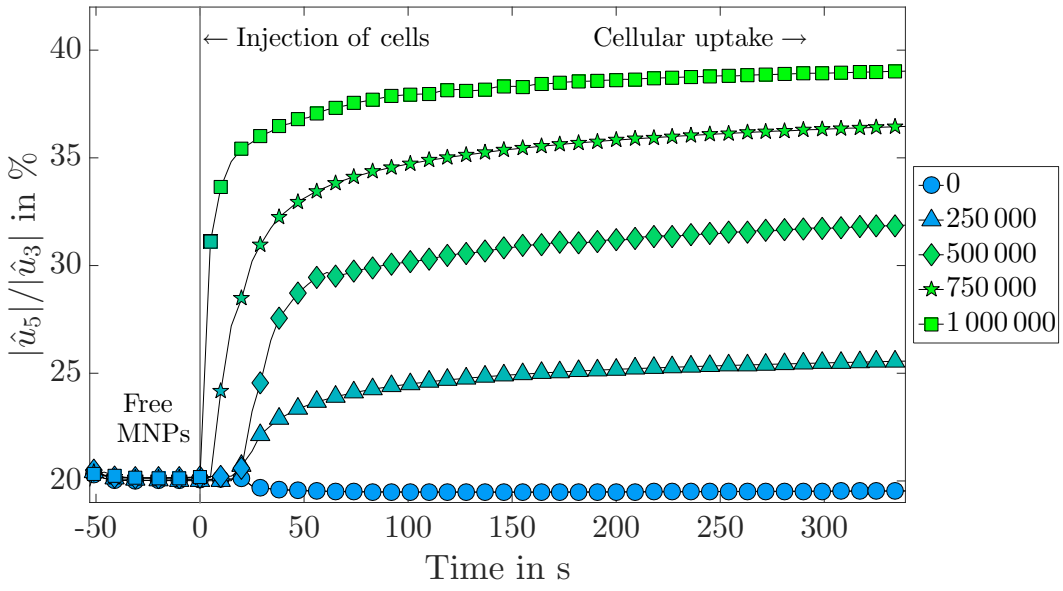

FIGURE 7.6: $|\hat{u}_5|/|\hat{u}_3|$ measured over time by MPS during initial contact between Synomag and THP-1 cells. Before the injection of cells, only free MNPs diluted in PBS were measured represented by an $|\hat{u}_5|/|\hat{u}_3| = 20.1\,\%$. At time $t = 0$, the cells were injected and the cellular uptake process starts. Due to the changing dynamic magnetic behavior of the samples, $|\hat{u}_5|/|\hat{u}_3|$ increases over time until saturation is reached after about 3 min. The colors of the marker symbols in the figure visualize the dominating state of the MNPs: blue representing free MNPs and green representing cell-bound MNPs.

After injecting cells, $|\hat{u}_5|/|\hat{u}_3|$ increased over time. This increase was caused by a changing dynamic magnetic behavior of the MNP ensemble induced by interactions between MNPs and THP-1 cells. The results indicate that the strongest magnetic changes happen during the first 180 s of MNP-cell

contact, which is in agreement with previous studies performed with different MNP types [157]. These signal changes are likely a consequence of MNP immobilization and agglomeration. The more cells were injected, the stronger the increase of $|\hat{u}_5|/|\hat{u}_3|$ with values up to 39.0 %. The magnetic signal characteristic associated with the cell-bound MNPs are visualized by a green color in figure 7.6.

7.2.4 In-vitro MPI

The previous sections verified a rapid uptake of Synomag in THP-1 cells and showed that this process is associated with characteristic changes of the dynamic magnetic behavior. In the following section, it is demonstrated that this uptake can be imaged and quantified using multi-color MPI.

Experimental setup

In-vitro MPI measurements were performed using a similar setup as described for the MPS measurements in section 7.2.3. MPI measurements were acquired over 29 min and a new averaged data set for reconstruction was obtained every 2.1 s. Each acquisition started with measurements of the empty scanner, used for background correction as described in section 4.2.3 (t_{start}). Two minutes after the start of the measurement, the sample holder containing 40 µL Synomag diluted in PBS ($c_{\text{Fe}} = 50\,\text{mmol/L}$) was moved to the FOV center (t_1). After one additional minute, a varying number of $0/0.25/0.5/0.75/1 \cdot 10^6$ THP-1 cells diluted in 100 µL PBS were injected to the MNPs (t_2). The time of injecting the cells is defined as $t_2 = 0$.

For each data set, a multi-color reconstruction was performed using previously acquired SFs of MNPs diluted in PBS and MNPs internalized by THP-1 cells. The reconstruction parameters were chosen as described by method 2, presented in section 6.1.4. A detailed list of the SF, measurement and reconstruction parameters is given in A.5. The reconstructed MPI intensities of the MNP distributions obtained by the multi-color reconstruction were integrated in an ROI centered around the nominal sample positions and were converted into the total iron masses of free $m_{\text{Fe,MPI,free}}$ and cell-bound $m_{\text{Fe,MPI,cell}}$ MNPs, respectively. The relative deviation of the total iron amount compared to the determined iron mass before injection ($m_{\text{Fe,0}}$) was calculated as $\Delta m_{\text{Fe,MPI}} = \frac{(m_{\text{Fe,MPI,free}} + m_{\text{Fe,MPI,cell}}) - m_{\text{Fe,0}}}{m_{\text{Fe,0}}}$.

Qualitative results

Figure 7.7 displays MPI images of free (a) and cell-bound (b) MNP distributions at different times after the injection for a varying number of injected cells. The first column presents the MPI images acquired before injection, in which only MNPs diluted in PBS were measured. This agrees with the reconstruction results, showing only signal intensities for the free MNP distributions and no signal for cell-bound MNPs. The first row represents the control measurement, performed by injecting only PBS without any cells, in which no significant signal changes over time for free and cell-bound MNP distributions were detected. This agrees with the MPS results in which no changes of the dynamic magnetic behavior were observed (see section 7.2.3).

For other measurements, in which cells were injected, an increasing signal intensity around the nominal sample position as a function of time was determined. Larger numbers of injected cells resulted in stronger signal intensities of the cell MNP distribution. No significant influence on the free MNP distributions were observed for most of the measurements. For the injection of $0.75 \cdot 10^6$ and $1 \cdot 10^6$ cells, artifacts at the edges of the FOV started to appear 10 min after the injection. After 15 min, no further visible changes for the free and cell-bound MNP distributions were observed as a function of time.

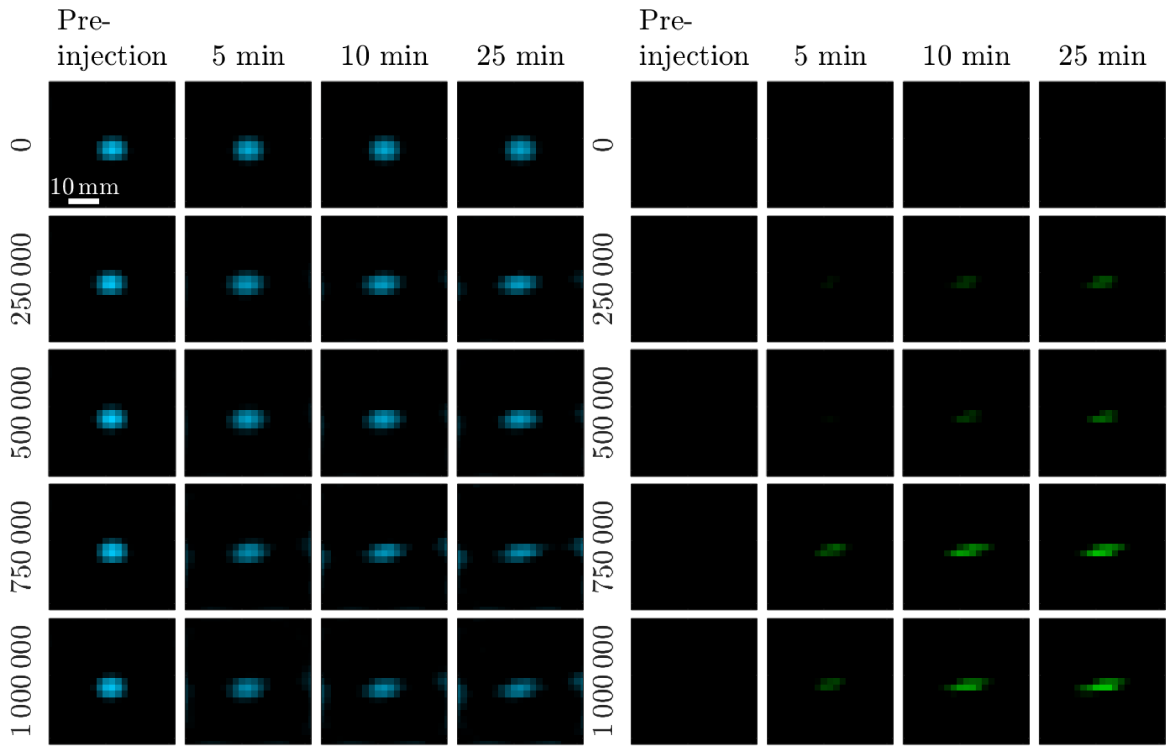

FIGURE 7.7: MPI images of free (a) and cell-bound (b) MNPs at different times before and after initial contact with THP-1 cells determined by multi-color reconstructions. Each row displays the results of a new measurement with a varying number of injected cells, stated on the left. The cell-bound MNPs show an increasing intensity over time, also scaling by the number of injected cells. No visual changes are observed for the reconstructions of free MNPs, except small artifacts appearing after about 10 min for high numbers of injected cells.

Quantitative results

Figure 7.8 displays $m_{\text{Fe,MPI,free}}$ (a) and $m_{\text{Fe,MPI,cell}}$ (b) over time for varying numbers of injected cells. The control experiment (injection of PBS only), shows no signal contribution of cell-bound MNPs over the whole acquisition time. The iron mass of free MNPs shows a decrease of 5 % over 27 min, which is likely caused by drifts of the background signals as described in section 4.2.3. After the injection of cells, $m_{\text{Fe,MPI,free}}$ decreased over time until saturation was reached after about 15 min. The more cells were injected, the stronger the decrease of free MNPs. At the same time, $m_{\text{Fe,MPI,cell}}$ increased over time until saturation, also depending on the number of injected cells. Ideally, the total iron mass

should be constant over the whole acquisition time. The deviation of the MPI-determined total iron mass $\Delta m_{\mathrm{Fe,MPI}}$ is shown in figure 7.8 c) and increases over time. Additionally, the deviation scales with the number of injected cells, reaching a maximum of 25.4 % for the injection of 10^6 cells after about 20 min.

Overall, the MPI results agree with the behavior observed in the reference experiments performed using colorimetric measurements (see section 7.2.2). A quantitative comparison between both methods of the cell-bound MNP contributions yields a mean relative difference of 23.8 %. For the iron mass representing free MNPs much higher deviations of up to 100 % were determined, mainly caused by the underestimations of the reference measurement technique due to losses in the sample preparation.

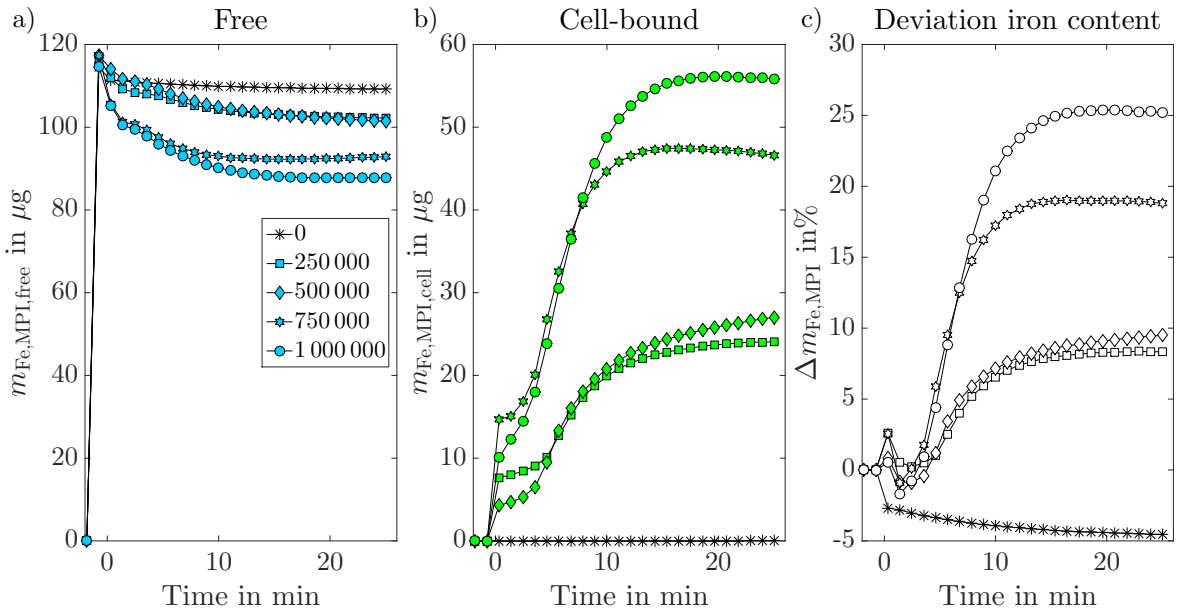

FIGURE 7.8: Quantified iron mass of free (a) and cell-bound (b) MNPs determined by MPI after initial contact with THP-1 cells. Decreasing iron amounts of free MNPs and increasing amounts of cell-bound MNPs are observed. c) displays the relative deviation of the total iron mass compared to the initially quantified amount of free MNPs before injection. Overall, the total iron mass detected by MPI is overestimated, scaling with time and the number of injected cells. The lines connecting the data points do not represent measurement data and are only shown for improved visibility.

7.3 Multi-color MPI: Summary and discussion

The focus of this chapter was the influence of the MNP environment on the qualitative and quantitative performance of MPI. These topics were mainly investigated in the context of cellular MPI, as one of the most promising future biomedical applications of MPI, but can be adapted for different environmental factors as well. A phantom study was performed using MNPs diluted in water and internalized in THP-1 cells. MPI images acquired by "conventional" MPI, using a single SF, exhibit imaging artifacts and quantification errors up to 124 % if the MNP environment does not match to the environmental conditions present during the SF acquisition. A method for including multiple environmental factors

was presented using additional SFs and combining them for multi-color reconstruction. Using this technique, the MPI images showed no imaging artifacts and quantification was possible with an accuracy of 12 % or lower, which is only slightly worse than the accuracy determined for conventional MPI in section 6.2. The remaining differences of the quantification accuracy compared to conventional MPI are likely caused by a higher mathematical uncertainty of the multi-color reconstruction (see section 2.2.3). A further advantage of the multi-color approach is that information about the MNP environment can be extracted from MPI images. This allowed a clear differentiation between free and cell-bound MNPs based on their different magnetic signal patterns. These results demonstrate the first example, in which multi-color MPI is used to gain information about the MNP environment while still maintaining the possibility to quantify the iron content.

The ability to differentiate between free and cell-bound MNPs was used to demonstrate that MPI is able to image and quantify the cellular uptake of Synomag in THP-1 cells. For this purpose, first the uptake of the MNPs into cells were verified using light microscopy measurements. Next, the uptake dynamics were analyzed based on colorimetric measurements, showing a rapid uptake with saturation after about 15 min. In-vitro MPS measurements of MNPs in contact with THP-1 cells were performed and indicate changes of the dynamic magnetic behavior caused by MNPs interacting with THP-1 cells. The strongest signal changes happened during the first 180 s, which is in good agreement with previous studies [157]. Compared to the colorimetric measurements of the cellular uptake, the MPS results showed faster signal changes. This might be attributed to the higher temperature of 37 °C inside the MPS, which could affect the dynamic uptake behavior.

Finally, the observed magnetic signal changes were utilized in combination with the high temporal resolution of MPI to image and quantify the cellular uptake of MNPs in an in-vitro experiment. For this purpose, MNPs and THP-1 cells were brought into initial contact while acquiring MPI data. An increase of cell-bound MNPs and a decrease of free MNPs over time was determined, which is in good qualitative agreement with the colorimetric reference measurements. A quantitative comparison between MPI and the colorimetric measurements yielded a deviation of 23.8 % for cell-bound MNPs. The amounts of free MNPs showed larger deviations up to 100 % between both methods, which were likely caused by MNP losses during the washing steps required for the colorimetric measurements.

The total iron mass, determined by MPI, increased over time and correlated with the number of injected cells. These deviations were partly caused by drifts of the background signals as described in section 4.2.3. An additional reason for the deviations was likely caused by MNPs at different environmental conditions compared to the two SFs used for reconstruction. It was assumed, that the whole MNP internalization process is described using only two MNP states ("free" or "cell-bound"). Previous studies demonstrated, that MNP undergo multiple states generating different magnetic signal patterns during cellular uptake [157, 158]. These signal patterns could theoretically be considered by additional SFs. This complicates the image reconstruction from a mathematical point of view, as more variables (reconstructed voxels) are added for the same amount of information (number of frequency components). In general, little research has been performed focusing around multi-color MPI, and many open questions remain. So far no criteria is defined, how well different magnetic signals can

be separated and what the most important parameters for this separation are. Additional factors, e.g. weighting of certain frequency components, the use of multiple receive coils or different algorithms to solve the image reconstruction need to be considered and might improve multi-color MPI [81].

The chosen experimental setup represents a simplified setup to be able to comprehend the observed effects. Further investigations are required to evaluate how the presented technique performs in more realistic scenarios. For instance the presence of biological media leads to the formation of a protein corona around the MNPs, which affects the internalization process, their dynamic magnetic behavior and hence their MPI performance [170, 171].

Previous studies demonstrated that MRI also enables the differentiation between free and cell-bound MNPs by analyzing differences in the relaxation rates [172, 173]. Although these techniques offer advantages compared to MPI, such as the simultaneous acquisition of anatomical information (see section 6.3), the temporal resolution is not sufficient to image the cellular uptake process.

In conclusion, the results demonstrate the strength of MPI to image and quantify the cellular uptake of MNPs. Since inflammatory diseases are directly linked to the uptake of MNPs, the quantified cell-bound iron represents a highly interesting biomarker. This method might lead to a novel diagnostics platform build around quantitative multi-color MPI. The methodology can easily be adapted for different MNP types or cell types and provides interesting opportunities for a better understanding of processes related to cellular uptake, which are of high interest for fundamental biomedical research [174, 175].

Chapter 8

Summary and Conclusions

This thesis demonstrated to what extent quantitative information about the MNP amount can be extracted from MPI measurement data. Imaging of MNP samples was achieved with a limit of detection of $m_{\mathrm{Fe}} = 16\,\mathrm{ng}$ and the iron amounts of MNPs were successfully quantified with an accuracy of 8.8 %. These values are influenced by multiple factors, which were studied separately in three objectives, namely the MPI hardware components, the data processing and the MNP environment. The dominant factors with the strongest impact on quantitative MPI for each of these objectives have been identified and will be shortly presented and the importance of considering these factors in the further development of MPI technology will be highlighted in the following.

Considering the hardware components, the factor with great impact on the limit of detection is the detection of systematic background components in the MPI raw signals. This factor hampers the identification of signals generated by MNPs and results in an about 30-fold higher limit of detection if uncorrected. The partial detection of the excitation fields in the measurement signal was identified as the main cause for these background signals. The removal of these components was partly realized by a receive-only (Rx) coil designed as a gradiometer. This coil yields a higher sensitivity (mean increase by a factor of 4) and strong attenuation of background signals (mean attenuation by a factor of 65) compared to the standard transmit-receive (TxRx)-coils. Additional removal was realized in the signal processing by subtracting empty scanner measurements. A complete removal was not achieved due to temporal variations and drifts of the background signal contributions. Thus it can be concluded, that background signals are the major limiting factor for the MPI sensitivity. For a clinical use of MPI, where a high sensitivity is mandatory, this has to be addressed especially when thinking of hardware components geometrically upscaled to human sizes. The presented methods of combining advanced hardware components and software solutions to minimize the effects of background signals and to improve the MPI sensitivity form a valuable base for further developments.

In the data processing it turned out that the image reconstruction has major impact especially on the MPI quantification accuracy. The algorithms and reconstruction parameters used in the image reconstruction are commonly chosen manually based on visual inspection of the qualitative image results without well-defined criteria. Modifying each reconstruction parameter showed strong influence on the quantitative results with deviations from the nominal iron mass of more than 1000 %. This could be circumvented by rescaling the intensities utilizing a reference measurement with

known MNP amount. This technique was successfully tested and verified in phantom experiments. However, a more concise investigation should be carried out to analyze the influence of the different reconstruction algorithms employed for MPI applications, especially since these algorithms are still under development. This might lead to further improvements of the MPI quantification accuracy.

Analyzing the influence of the MNP environment showed quantification errors of more than 100 % if the environmental conditions of the reference measurement needed for the MPI image reconstruction and the actual measurement are not taken into account properly. Different MNP environments lead to changes in the dynamic magnetic behavior, which could be identified as the main reason for the deviation. In realistic biomedical applications, changes of the MNP environment are inevitable. Depending on the biomedical application, multiple environmental factors need to be considered to achieve accurate MPI quantification. A technique, called multi-color MPI, is a powerful approach to include several environmental factors in the image reconstruction and was successfully used to improve the accuracy to 12 % for cell measurements. However, the physical and mathematical limitations of multi-color MPI are currently not completely understood. For this purpose, a better understanding of the impact of biological factors on the dynamic magnetic behavior of MNPs is required and would dramatically propel the MPI performance.

The second aim of this theses was to demonstrate and assess the potential of quantitative MPI for biomedical applications. This thesis proved that MPI provides accurate quantitative information about the MNP amount. This information is highly valuable and directly affects the success of applications such as hyperthermia treatments, drug delivery applications and cell tracking studies. Compared to MRI, as an established and commonly used imaging modality for MNPs, several advantages were identified. MPI detects MNPs specifically, simplifying the image analysis, since no additional reference scans without MNPs are required and no signal is generated by surrounding tissue. The limit of detection of MPI in terms of iron concentration is worse compared to MRI in pure water ($c_{\mathrm{Fe,MPI}} = 15.8\,\mu\mathrm{mol/L}$, $c_{\mathrm{Fe,MRI}} = 2.4\,\mu\mathrm{mol/L}$) but is superior in media with more realistic biological relaxation times (e.g. in $CuSO_4$-solution mimicking relaxation times of human liver tissue: $c_{\mathrm{Fe,MPI}} = 47.5\,\mu\mathrm{mol/L}$, $c_{\mathrm{Fe,MRI}} = 0.25\,\mathrm{mmol/L}$). Additionally MPI showed an about 2-fold improved accuracy ($u_{\mathrm{c,MPI}} = 8.8\,\%$, $u_{\mathrm{c,MRI}} = 16.8\,\%$). In conclusion, MPI provides an overall improved quantification performance compared to MRI. However, some disadvantages, such as the small size of the field of view and the lack of anatomical reference information in the imaging data, need to be addressed for a clinical success of MPI. It is the combination of both techniques in one system, from which biomedical imaging could benefit. Such a system could exploit the advantages of both techniques, anatomical information provided by MRI and MNP localization and quantification by MPI.

MNPs interacting with living cells are expected to become one of the most important future applications of quantitative MPI and were investigated in this study. The results of the cell-measurements showed that MPI provides, in addition to the quantitative spatial distribution of MNPs, the ability to distinguish MNPs in different environmental states (e.g. cell-bound or unbound). The technique was

combined with the high temporal resolution of MPI (here 2.15 s) to image and quantify the cellular uptake of MNPs into living cells. This information is of high interest for an early diagnostics and better understanding of fundamental processes involved in inflammatory diseases and might pave the way for a new diagnostics platform build around quantitative MPI.

Outlook

This final section addresses some of the upcoming challenges and also promising new opportunities for quantitative MPI in the near future.

The measurements presented in this study were performed on a preclinical MPI system. MPI aims for a clinical use in humans. The upscaling of MPI applications to human sizes is a technically demanding task and might bring new challenges also concerning quantitative MPI. For instance, larger field of views are needed and could be achieved using additional magnetic fields. But this also results in more sophisticated hardware requirements and possibly stronger background signals, which have to be considered in the quantitative analysis. The recent years showed a growing interest of moving the focus from a full-body MPI scanner towards smaller scanners dedicated to certain body parts (e.g. head or breast scanners). This lowers the required technical efforts and might bring MPI into clinical use on shorter time scales.

An additional area with a lot of development is the theoretical modeling of the nanoparticle physics. Currently, the simulations are not sufficient to accurately predict the measurement results. However, the advantages gained by improved theoretical models would be immense and would highly benefit MPI technology. For instance, this would lead to a drastic reduction of the time needed to acquire the reference measurements, which are currently used for image reconstruction. Additionally, the consideration of multiple environmental factors, like temperature and viscosity, could be included more easily in the reconstruction, leading to improved imaging results.

Some of the biggest potential lies in the further development of quantitative multi-color MPI. The imaging and quantification of the cellular uptake of MNPs demonstrated already one promising example of this technique. The methodology can easily be adapted and used for other factors influencing the MPI signal generation. This offers plenty of opportunities for implementing MPI to image and quantify processes, which involve interactions of MNPs with nanoscale objects.

Appendix A

MPI parameter

This section provides an overview of the MPI measurement, SF and reconstruction parameters used for each experiment of this study.

Parameter	Value
Drive field *x*/*y*/*z* in mT	12/12/12
Gradient *x*/*y*/*z* in T/m	1.25/1.25/2.5
Averages	100
Repetitions	1

Parameter	Value
SF FOV	25x25x13 mm^2
SF Grid	25x25x13
BG increment	25
BG repetitions	5
SF volume	1 µL
c_{Fe}	0.935 mol/L

Parameter	Value
N_{FC}	$25 - 10000$
$\hat{\lambda}$	$10^{-12} - 10^{5}$
N_{it}	$1 - 10000$

TABLE A.1: MPI measurement, SF and reconstruction parameters used in section 6.1

Parameter	Value
Drive field *x*/*y*/*z* in mT	12/12/12
Gradient *x*/*y*/*z* in T/m	1.25/1.25/2.5
Averages	100
Repetitions	27

Parameter	Value
SF FOV	22x22x11 mm^2
SF Grid	32x32x16
BG increment	32
BG repetitions	5
SF volume	1 µL
c_{Fe}	0.935 mol/L

Parameter	Value
N_{FC}	139
$\hat{\lambda}$	200
N_{it}	1

TABLE A.2: MPI measurement, SF and reconstruction parameters used in section 6.2.1

Parameter	Value
Drive field *x*/*y*/*z* in mT	12/12/12
Gradient *x*/*y*/*z* in T/m	1.25/1.25/2.5
Averages	100
Repetitions	10

Parameter	Value
SF FOV	22x22x11 mm^2
SF Grid	32x32x16
BG increment	32
BG repetitions	5
SF volume	1 µL
c_{Fe}	0.935 mol/L

Parameter	Value
N_{FC}	58
$\hat{\lambda}$	0.1
N_{it}	1

TABLE A.3: MPI measurement, SF and reconstruction parameters used in section 6.2.2

Parameter	**Value**
Drive field *x*/*y*/*z* in mT	12/12/12
Gradient *x*/*y*/*z* in T/m	0.6/0.6/1.2
Averages	100
Repetitions	10

Parameter	**Value**
SF FOV	42x42x24 mm^2
SF Grid	21x21x12
BG increment	21
BG repetitions	5
SF1 volume (free)	8 µL
SF1 c_{Fe} (free)	0.107 mol/L
SF2 volume (cell)	≈ 8 µL
SF2 c_{Fe} (cell)	n.a.

Parameter	**Value**
N_{FC}	600
$\hat{\lambda}$	0.005
N_{it}	10000

TABLE A.4: MPI measurement, SF and reconstruction parameters used in section 7.1

Parameter	**Value**
Drive field *x*/*y*/*z* in mT	12/12/12
Gradient *x*/*y*/*z* in T/m	0.6/0.6/1.2
Averages	100
Repetitions	800

Parameter	**Value**
SF FOV	42x42x24 mm^2
SF Grid	21x21x12
BG increment	21
BG repetitions	5
SF1 volume (free)	8 µL
SF1 c_{Fe} (free)	0.049 mol/L
SF2 volume (cell)	≈ 8 µL
SF2 c_{Fe} (cell)	n.a.

Parameter	**Value**
N_{FC}	500
$\hat{\lambda}$	0.04
N_{it}	1000

TABLE A.5: MPI measurement, SF and reconstruction parameters used in section 7.2

Peer-reviewed first-authored paper

HP1 Hendrik Paysen, James Wells, Olaf Kosch, Uwe Steinhoff, Lutz Trahms, Tobias Schaeffter, and Frank Wiekhorst. “Towards quantitative magnetic particle imaging: A comparison with magnetic particle spectroscopy”. In: *AIP Advances* 8.5 (May 2018). ISSN: 21583226. DOI: 10.1063/1.5006391

HP2 Hendrik Paysen, James Wells, Olaf Kosch, Uwe Steinhoff, Jochen Franke, Lutz Trahms, Tobias Schaeffter, and Frank Wiekhorst. “Improved sensitivity and limit-of-detection using a receive-only coil in magnetic particle imaging”. In: *Physics in Medicine & Biology* 63.13 (July 2018). ISSN: 1361-6560. DOI: 10.1088/1361-6560/aacb87

HP3 Hendrik Paysen, Norbert Loewa, Karol Weber, Olaf Kosch, James Wells, Tobias Schaeffter, and Frank Wiekhorst. “Imaging and quantification of magnetic nanoparticles: Comparison of magnetic resonance imaging and magnetic particle imaging”. In: *Journal of Magnetism and Magnetic Materials* 475 (Apr. 2019), pp. 382–388. ISSN: 03048853. DOI: 10.1016/j.jmmm.2018.10.082

HP4 Hendrik Paysen, Norbert Loewa, Anke Stach, James Wells, Olaf Kosch, Shailey Twamley, Marcus R. Makowski, Tobias Schaeffter, Antje Ludwig, and Frank Wiekhorst. “Cellular uptake of magnetic nanoparticles imaged and quantified by magnetic particle imaging”. In: *Scientific Reports* 10.1 (Dec. 2020). ISSN: 2045-2322. DOI: 10.1038/s41598-020-58853-3

Peer-reviewed co-authored paper

HP5 James Wells, Hendrik Paysen, Olaf Kosch, Norbert Löwa, Florian Schmitzberger, Marcus Makowksi, Jochen Franke, Lutz Trahms, and Frank Wiekhorst. "Characterizing a Preclinical Magnetic Particle Imaging System With Separate Pickup Coil". In: *IEEE Transactions on Magnetics* 53.11 (Nov. 2017), pp. 1–5. ISSN: 00189464. DOI: 10.1109/TMAG.2017.2708419

HP6 James Wells, Hendrik Paysen, Olaf Kosch, Lutz Trahms, and Frank Wiekhorst. "Temperature dependence in magnetic particle imaging". In: *AIP Advances* 8.5 (May 2018). ISSN: 2158-3226. DOI: 10.1063/1.5004506

HP7 Norbert Löwa, Josephine Marie Fabert, Dirk Gutkelch, Hendrik Paysen, Olaf Kosch, and Frank Wiekhorst. "3D-printing of novel magnetic composites based on magnetic nanoparticles and photopolymers". In: *Journal of Magnetism and Magnetic Materials* 469 (Jan. 2019), pp. 456–460. ISSN: 03048853. DOI: 10.1016/j.jmmm.2018.08.073

HP8 Olaf Kosch, Hendrik Paysen, James Wells, Felix Ptach, Jochen Franke, Lucas Wöckel, Silvio Dutz, and Frank Wiekhorst. "Evaluation of a separate-receive coil by magnetic particle imaging of a solid phantom". In: *Journal of Magnetism and Magnetic Materials* 471 (Feb. 2019), pp. 444–449. ISSN: 03048853. DOI: 10.1016/j.jmmm.2018.09.114

HP9 James Wells, Norbert Löwa, Hendrik Paysen, Uwe Steinhoff, and Frank Wiekhorst. "Probing particle-matrix interactions during magnetic particle spectroscopy". In: *Journal of Magnetism and Magnetic Materials* 475 (Apr. 2019), pp. 421–428. ISSN: 03048853. DOI: 10.1016/j.jmmm.2018.11.109

Bibliography

[1] Elizabeth A. Krupinski. "The importance of perception research in medical imaging." In: *Radiation medicine* 18.6 (2000), pp. 329–34. ISSN: 0288-2043.

[2] Harold L. Kundel. "History of Research in Medical Image Perception". In: *Journal of the American College of Radiology* 3.6 (June 2006), pp. 402–408. ISSN: 15461440. DOI: 10.1016/j.jacr.2006.02.023.

[3] Elizabeth A. Krupinski. "Current perspectives in medical image perception". In: *Attention, Perception & Psychophysics* 72.5 (July 2010), pp. 1205–1217. ISSN: 1943-3921. DOI: 10.3758/APP.72.5.1205.

[4] Andrew B Rosenkrantz et al. "Clinical Utility of Quantitative Imaging". In: *Academic Radiology* 22.1 (Jan. 2015), pp. 33–49. ISSN: 18784046. DOI: 10.1016/j.acra.2014.08.011.

[5] Yi-Xiang J Wang et al. "The impact of quantitative imaging in medicine and surgery: Charting our course for the future." In: *Quantitative imaging in medicine and surgery* 1.1 (2011), pp. 1–3. ISSN: 2223-4292. DOI: 10.3978/j.issn.2223-4292.2011.09.01.

[6] Robert J. Gillies et al. "Radiomics: Images are more than pictures, they are data". In: *Radiology* 278.2 (Feb. 2016), pp. 563–577. ISSN: 15271315. DOI: 10.1148/radiol.2015151169.

[7] Kevin J. Glaser et al. "Review of MR elastography applications and recent developments". In: *Journal of Magnetic Resonance Imaging* 36.4 (Oct. 2012), pp. 757–774. ISSN: 10531807. DOI: 10.1002/jmri.23597.

[8] Dan Ma et al. "Magnetic resonance fingerprinting". In: *Nature* 495.7440 (Mar. 2013), pp. 187–192. ISSN: 0028-0836. DOI: 10.1038/nature11971.

[9] J. Wenz et al. "Quantitative X-ray phase-contrast microtomography from a compact laser-driven betatron source". In: *Nature Communications* 6.1 (Nov. 2015), p. 7568. ISSN: 2041-1723. DOI: 10.1038/ncomms8568.

[10] C E Cann. "Quantitative CT for determination of bone mineral density: a review." In: *Radiology* 166.2 (Feb. 1988), pp. 509–522. ISSN: 0033-8419. DOI: 10.1148/radiology.166.2.3275985.

[11] Prins et al. "The role of quantitative ultrasound in the assessment of bone: a review". In: *Clinical Physiology* 18.1 (Jan. 1998), pp. 3–17. ISSN: 01445979. DOI: 10.1046/j.1365-2281.1998.00067.x.

[12] Ronald Boellaard. “Standards for PET Image Acquisition and Quantitative Data Analysis”. In: *Journal of Nuclear Medicine* 50 (May 2009), pp. 11–20. ISSN: 0161-5505. DOI: 10.2967/jnumed.108.057182.

[13] Dale L Bailey et al. “An Evidence-Based Review of Quantitative SPECT Imaging and Potential Clinical Applications”. In: *Journal of Nuclear Medicine* 54.1 (Jan. 2013), pp. 83–89. ISSN: 0161-5505. DOI: 10.2967/jnumed.112.111476.

[14] B Gleich et al. “Tomographic imaging using the nonlinear response of magnetic particles”. In: *Nature* 435.7046 (2005), pp. 1214–1217. ISSN: 1476-4687. DOI: 10.1038/nature03808.

[15] J Weizenecker et al. “Three-dimensional real-time in vivo magnetic particle imaging”. In: *Physics in Medicine and Biology* 54.5 (Mar. 2009), pp. 1–10. ISSN: 0031-9155. DOI: 10.1088/0031-9155/54/5/L01.

[16] Jan Sedlacik et al. “Magnetic Particle Imaging for High Temporal Resolution Assessment of Aneurysm Hemodynamics”. In: *PLOS ONE* 11.8 (Aug. 2016). Ed. by Josué Sznitman. ISSN: 1932-6203. DOI: 10.1371/journal.pone.0160097.

[17] Rudolf Hergt et al. “Magnetic particle hyperthermia: nanoparticle magnetism and materials development for cancer therapy”. In: *Journal of Physics: Condensed Matter* 18.38 (Sept. 2006), pp. 2919–2934. ISSN: 0953-8984. DOI: 10.1088/0953-8984/18/38/S26.

[18] Silvio Dutz et al. “Magnetic particle hyperthermia—a promising tumour therapy?” In: *Nanotechnology* 25.45 (Nov. 2014). ISSN: 0957-4484. DOI: 10.1088/0957-4484/25/45/452001.

[19] Manuel Arruebo et al. “Magnetic nanoparticles for drug delivery”. In: *Nano Today* 2.3 (June 2007), pp. 22–32. ISSN: 17480132. DOI: 10.1016/S1748-0132(07)70084-1.

[20] Maïté Lewin et al. “Tat peptide-derivatized magnetic nanoparticles allow in vivo tracking and recovery of progenitor cells”. In: *Nature Biotechnology* 18.4 (Apr. 2000), pp. 410–414. ISSN: 1087-0156. DOI: 10.1038/74464.

[21] Kenya Murase et al. “Usefulness of Magnetic Particle Imaging for Predicting the Therapeutic Effect of Magnetic Hyperthermia”. In: *Open Journal of Medical Imaging* 05.02 (2015), pp. 85–99. ISSN: 2164-2788. DOI: 10.4236/ojmi.2015.52013.

[22] Xingming Zhang et al. “Development of a real time imaging-based guidance system of magnetic nanoparticles for targeted drug delivery”. In: *Journal of Magnetism and Magnetic Materials* 427 (Apr. 2017), pp. 345–351. ISSN: 03048853. DOI: 10.1016/j.jmmm.2016.10.056.

[23] Maruyama Shuki et al. “Development of Magnetic Nanocarriers based on Thermosensitive Liposomes and their Visualization using Magnetic Particle Imaging”. In: *International Journal of Nanomedicine and Nanosurgery* 2.2 (2016). ISSN: 24703206. DOI: 10.16966/2470-3206.111.

[24] Bo Zheng et al. “Magnetic Particle Imaging tracks the long-term fate of in vivo neural cell implants with high image contrast”. In: *Scientific Reports* 5.1 (Nov. 2015), p. 14055. ISSN: 2045-2322. DOI: 10.1038/srep14055.

[25] Bo Zheng et al. “Quantitative magnetic particle imaging monitors the transplantation, biodistribution, and clearance of stem cells in vivo”. In: *Theranostics* 6.3 (2016), pp. 291–301. ISSN: 18387640. DOI: 10.7150/thno.13728.

[26] J Dieckhoff et al. “In vivo liver visualizations with magnetic particle imaging based on the calibration measurement approach”. In: *Physics in Medicine and Biology* 62.9 (2017), pp. 3470–3482. ISSN: 13616560. DOI: 10.1088/1361-6560/aa562d.

[27] Sarah Vaalma et al. “Magnetic Particle Imaging (MPI): Experimental quantification of vascular stenosis using stationary stenosis phantoms”. In: *PLoS ONE* 12.1 (2017). ISSN: 19326203. DOI: 10.1371/journal.pone.0168902.

[28] Zhi Wei Tay et al. “In vivo tracking and quantification of inhaled aerosol using magnetic particle imaging towards inhaled therapeutic monitoring”. In: *Theranostics* 8.13 (2018), pp. 3676–3687. ISSN: 1838-7640. DOI: 10.7150/thno.26608.

[29] Elaine Y. Yu et al. “Magnetic Particle Imaging for Highly Sensitive, Quantitative, and Safe in Vivo Gut Bleed Detection in a Murine Model”. In: *ACS Nano* 11.12 (Dec. 2017), pp. 12067–12076. ISSN: 1936086X. DOI: 10.1021/acsnano.7b04844.

[30] Daniel Hensley et al. “Combining magnetic particle imaging and magnetic fluid hyperthermia in a theranostic platform”. In: *Physics in Medicine and Biology* 62.9 (May 2017), pp. 3483–3500. ISSN: 0031-9155. DOI: 10.1088/1361-6560/aa5601.

[31] Hamed Arami et al. “Tomographic Magnetic Particle Imaging of Cancer Targeted Nanoparticles”. In: *Nanoscale* (2017). ISSN: 2040-3364. DOI: 10.1039/C7NR05502A.

[32] M. Gräser et al. “Human-sized Magnetic Particle Imaging for Brain Applications”. In: *Nature Communications* 2019 (2018). ISSN: 2041-1723. DOI: 10.1038/s41467-019-09704-x. arXiv: 1810.07987.

[33] Erica E Mason et al. “Magnet Assembly Design for a Human-Scale Functional Magnetic Particle Imager (fMPI)”. In: *IWMPI* (Mar. 2019).

[34] Jörn Borgert et al. “Perspectives on clinical magnetic particle imaging.” In: *Biomedizinische Technik. Biomedical engineering* 58.6 (Dec. 2013). ISSN: 1862-278X. DOI: 10.1515/bmt-2012-0064.

[35] Patrick Vogel et al. “μ MPI—Initial Experiments With an Ultrahigh Resolution MPI”. In: *IEEE Transactions on Magnetics* 51.2 (Feb. 2015), pp. 1–4. ISSN: 0018-9464. DOI: 10.1109/TMAG.2014.2329135.

[36] Florian Griese et al. “Submillimeter-Accurate Marker Localization within Low Gradient Magnetic Particle Imaging Tomograms”. In: *International Journal on Magnetic Particle Imaging* 3.1 (2017), p. 1703011.

[37] R. Matthew Ferguson et al. “Magnetic particle imaging with tailored iron oxide nanoparticle tracers”. In: *IEEE Transactions on Medical Imaging* 34.5 (May 2015), pp. 1077–1084. ISSN: 1558254X. DOI: 10.1109/TMI.2014.2375065.

[38] Matthias Graeser et al. “Towards Picogram Detection of Superparamagnetic Iron-Oxide Particles Using a Gradiometric Receive Coil”. In: *Scientific Reports* 7.1 (2017), pp. 1–13. ISSN: 20452322. DOI: 10.1038/s41598-017-06992-5. arXiv: 1704.01789.

[39] Harald Kratz et al. “Novel magnetic multicore nanoparticles designed for MPI and other biomedical applications: From synthesis to first in vivo studies”. In: *PLoS ONE* 13.1 (Jan. 2018). Ed. by Raphael Levy. ISSN: 19326203. DOI: 10.1371/journal.pone.0190214.

[40] Emine U. Saritas et al. “Magnetic particle imaging (MPI) for NMR and MRI researchers”. In: *Journal of Magnetic Resonance* 229 (2013), pp. 116–126. ISSN: 10907807. DOI: 10.1016/j.jmr.2012.11.029.

[41] Matthias Graeser et al. “Analog receive signal processing for magnetic particle imaging”. In: *Medical Physics* 40.4 (Apr. 2013). ISSN: 00942405. DOI: 10.1118/1.4794482.

[42] Volkmar Schulz et al. “A Field Cancellation Signal Extraction Method for Magnetic Particle Imaging”. In: *IEEE Transactions on Magnetics* 51.2 (Feb. 2015), pp. 1–4. ISSN: 0018-9464. DOI: 10.1109/TMAG.2014.2325852.

[43] Tuan-Anh Le et al. “Band-Stop Filter Analysis and Design for 1D Magnetic Particle Imaging Hybrid System”. In: *Journal of Nanoscience and Nanotechnology* 16.8 (Aug. 2016), pp. 8492–8495. ISSN: 1533-4880. DOI: 10.1166/jnn.2016.12520.

[44] Kazuki Shimada et al. “Effect of Signal Filtering on Image Quality of Projection-Based Magnetic Particle Imaging”. In: *Open Journal of Medical Imaging* 07.02 (2017), pp. 43–55. ISSN: 2164-2788. DOI: 10.4236/ojmi.2017.72005.

[45] Jürgen Rahmer et al. “Signal encoding in magnetic particle imaging: properties of the system function.” In: *BMC medical imaging* 9 (2009), p. 4. ISSN: 1471-2342. DOI: 10.1186/1471-2342-9-4.

[46] Jürgen Rahmer et al. “Analysis of a 3-D system function measured for magnetic particle imaging”. In: *IEEE Trans. Med. Imaging* 31.6 (2012), pp. 1289–1299. ISSN: 1558-254X. DOI: 10.1109/TMI.2012.2188639.

[47] Tobias Knopp et al. “Weighted iterative reconstruction for magnetic particle imaging”. In: *Physics in Medicine and Biology* 55.6 (2010), pp. 1577–1589. ISSN: 0031-9155. DOI: 10.1088/0031-9155/55/6/003.

[48] Tobias Knopp. "Effiziente Rekonstruktion und alternative Spulentopologien für Magnetic-Particle-Imaging". In: (2011), p. 192. ISSN: 3834881295. DOI: 10.1007/978-3-8348-8129-8.

[49] J Lampe et al. "Fast reconstruction in magnetic particle imaging". In: *Physics in Medicine and Biology* 57.4 (Feb. 2012), pp. 1113–1134. ISSN: 0031-9155. DOI: 10.1088/0031-9155/57/4/1113.

[50] T. Knopp et al. "Local System Matrix Compression for Efficient Reconstruction in Magnetic Particle Imaging". In: *Advances in Mathematical Physics* 2015 (Jan. 2015), pp. 1–7. ISSN: 1687-9120. DOI: 10.1155/2015/472818.

[51] Hiroki Tsuchiya et al. "Experimental Evaluation of an Iterative Reconstruction Method for Time-Correlation Magnetic Particle Imaging". In: *IWMPI* (2014), pp. 90–91.

[52] Martin Storath et al. "Edge preserving and noise reducing reconstruction for magnetic particle imaging." In: *IEEE transactions on medical imaging* 36.1 (2016), pp. 74–85. ISSN: 1558-254X. DOI: 10.1109/TMI.2016.2593954.

[53] Leonard Schmiester et al. "Direct Image Reconstruction of Lissajous-Type Magnetic Particle Imaging Data Using Chebyshev-Based Matrix Compression". In: *IEEE Transactions on Computational Imaging* 3.4 (Dec. 2017), pp. 671–681. ISSN: 2333-9403. DOI: 10.1109/TCI.2017.2706058.

[54] Tobias Kluth et al. "Model uncertainty in magnetic particle imaging: Nonlinear problem formulation and model-based sparse reconstruction". In: *International Journal on Magnetic Particle Imaging* 3.2 (July 2017). ISSN: 2365-9033.

[55] Sören Dittmer et al. "Regularization by Architecture: A Deep Prior Approach for Inverse Problems". In: *Journal of Mathematical Imaging and Vision* (Oct. 2019). ISSN: 0924-9907. DOI: 10.1007/s10851-019-00923-x.

[56] Christina Brandt et al. "Recovery from Errors Due to Domain Truncation in Magnetic Particle Imaging: Approximation Error Modeling Approach". In: *Journal of Mathematical Imaging and Vision* 60.8 (Oct. 2018), pp. 1196–1208. ISSN: 0924-9907. DOI: 10.1007/s10851-018-0807-z.

[57] Tobias Kluth et al. "Enhanced reconstruction in magnetic particle imaging by whitening and randomized SVD approximation". In: *Physics in medicine and biology* 64.12 (Jan. 2019). ISSN: 13616560. DOI: 10.1088/1361-6560/ab1a4f. arXiv: 1902.01199.

[58] Norbert Loewa et al. "Cellular uptake of magnetic nanoparticles quantified by magnetic particle spectroscopy". In: *IEEE Transactions on Magnetics* 49.1 (Jan. 2013), pp. 275–278. ISSN: 00189464. DOI: 10.1109/TMAG.2012.2218223.

[59] T. Wawrzik et al. “Estimating particle mobility in MPI”. In: *2013 International Workshop on Magnetic Particle Imaging, IWMPI 2013*. IEEE, Mar. 2013, pp. 1–1. ISBN: 9781467355223. DOI: 10.1109/IWMPI.2013.6528372.

[60] Daniel B. Reeves et al. “Measuring the microenvironmental temperature around magnetic nanoparticles”. In: *Animal* 1625.1 (2014). ISSN: 1751732X. DOI: 10.1557/opl.2014.217.

[61] I M Perreard et al. “Temperature of the magnetic nanoparticle microenvironment: estimation from relaxation times”. In: *Physics in Medicine and Biology* 59.5 (Mar. 2014), pp. 1109–1119. ISSN: 0031-9155. DOI: 10.1088/0031-9155/59/5/1109.

[62] Norbert Löwa et al. “Magnetic nanoparticles in different biological environments analyzed by magnetic particle spectroscopy”. In: *Journal of Magnetism and Magnetic Materials* 427 (Apr. 2017), pp. 133–138. ISSN: 03048853. DOI: 10.1016/j.jmmm.2016.10.096.

[63] James Wells et al. “Probing particle-matrix interactions during magnetic particle spectroscopy”. In: *Journal of Magnetism and Magnetic Materials* 475 (Apr. 2019), pp. 421–428. ISSN: 03048853. DOI: 10.1016/j.jmmm.2018.11.109.

[64] Eric Teeman et al. “Intracellular dynamics of superparamagnetic iron oxide nanoparticles for magnetic particle imaging”. In: *Nanoscale* (2019). ISSN: 2040-3364. DOI: 10.1039/C9NR01395D.

[65] Kenya Murase et al. “Magnetic particle imaging of blood coagulation”. In: *Applied Physics Letters* 104.25 (June 2014). ISSN: 0003-6951. DOI: 10.1063/1.4885146.

[66] Sergey P. Gubin, ed. *Magnetic Nanoparticles*. Wiley, Apr. 2009. ISBN: 9783527407903. DOI: 10.1002/9783527627561.

[67] P Langevin. “Sur la theorie du mouvement brownien”. In: *C.R. Acad. Sci., (Paris)* 146 (1908), pp. 530–533.

[68] Louis Néel. “Thermoremanent Magnetization of Fine Powders”. In: *Reviews of Modern Physics* 25.1 (Jan. 1953), pp. 293–295. ISSN: 0034-6861. DOI: 10.1103/RevModPhys.25.293.

[69] William Fuller Brown. “Thermal Fluctuations of a Single-Domain Particle”. In: *Physical Review* 130.5 (June 1963), pp. 1677–1686. ISSN: 0031-899X. DOI: 10.1103/PhysRev.130.1677.

[70] E. C. Stoner et al. “A Mechanism of Magnetic Hysteresis in Heterogeneous Alloys”. In: *Philosophical Transactions of the Royal Society A: Mathematical, Physical and Engineering Sciences* 240.826 (May 1948), pp. 599–642. ISSN: 1364-503X. DOI: 10.1098/rsta.1948.0007.

[71] J. M. Vargas et al. “Effect of dipolar interaction observed in iron-based nanoparticles”. In: *Physical Review B - Condensed Matter and Materials Physics* 72.18 (Nov. 2005). ISSN: 10980121. DOI: 10.1103/PhysRevB.72.184428.

[72] Tobias Knopp et al. *Magnetic particle imaging: An introduction to imaging principles and scanner instrumentation*. 2012, pp. 1–204. ISBN: 9783642041990. DOI: 10.1007/978-3-642-04199-0.

[73] Patrick W. Goodwill et al. "Narrowband magnetic particle imaging". In: *IEEE Transactions on Medical Imaging* 28.8 (Aug. 2009), pp. 1231–1237. ISSN: 02780062. DOI: 10.1109/TMI.2009.2013849.

[74] Patrick William Goodwill et al. "The x-space formulation of the magnetic particle imaging process: three-dimensional signal, gridding, pulse sequences, and reconstruction". In: *IEEE Transactions on Medical Imaging* 64.5-6 (2010), pp. 267–273. ISSN: 1558-0062. DOI: 10.1159/000197810.

[75] Patrick Vogel et al. "Superspeed Traveling Wave Magnetic Particle Imaging". In: *IEEE Transactions on Magnetics* 51.2 (Feb. 2015). ISSN: 00189464. DOI: 10.1109/TMAG.2014.2322897.

[76] Mandy Grüttner et al. "On the formulation of the image reconstruction problem in magnetic particle imaging". In: *Biomedizinische Technik/Biomedical Engineering* 58.6 (Jan. 2013), pp. 583–591. ISSN: 1862-278X. DOI: 10.1515/bmt-2012-0063.

[77] Hadamard J. "Sur les problèmes aux dérivées partielles et leur signification physique". In: *Princeton University Bulletin* 13 (1902), pp. 49–52.

[78] S Kaczmarz. "Approximate solution of systems of linear equations". In: *Bull. Acad. Polon. Sci. Lett. A 35 (1937) 355* 357 (1937).

[79] J. Rahmer et al. "First experimental evidence of the feasibility of multi-color magnetic particle imaging". In: *Physics in Medicine and Biology* 60.5 (2015), pp. 1775–1791. ISSN: 13616560. DOI: 10.1088/0031-9155/60/5/1775.

[80] Christian Stehning et al. "Simultaneous magnetic particle imaging (MPI) and temperature mapping using multi-color MPI". In: *IJMPI* 2.2 (2016), pp. 1–6. DOI: 10.18416/ijmpi.2016.1612001.

[81] Martin Möddel et al. "Viscosity quantification using multi-contrast magnetic particle imaging". In: *New Journal of Physics* 20.8 (2018). ISSN: 1367-2630. DOI: 10.1088/1367-2630/aad44b.

[82] Lars G. Hanson. "Is quantum mechanics necessary for understanding magnetic resonance?" In: *Concepts in Magnetic Resonance Part A* 32A.5 (Sept. 2008), pp. 329–340. ISSN: 15466086. DOI: 10.1002/cmr.a.20123.

[83] Malcolm H. Levitt. *Spin dynamics : basics of nuclear magnetic resonance*. John Wiley & Sons, 2001, pp. 1–686. ISBN: 9780471489214.

[84] Robert W. Brown et al. *Magnetic Resonance Imaging: Physical Principles and Sequence Design: Second Edition*. Ed. by Robert W. Brown et al. Vol. 9780471720. Chichester, UK: John Wiley & Sons Ltd, Apr. 2014, pp. 1–944. ISBN: 9781118633953. DOI: 10.1002/9781118633953.

[85] Randall B. Lauffer. "Paramagnetic Metal Complexes as Water Proton Relaxation Agents for NMR Imaging: Theory and Design". In: *Chemical Reviews* 87.5 (Oct. 1987), pp. 901–927. ISSN: 15206890. DOI: 10.1021/cr00081a003.

[86] Seymour H. Koenig et al. "Theory of 1/T1 and 1/T2 NMRD profiles of solutions of magnetic nanoparticles". In: *Magnetic Resonance in Medicine* 34.2 (Aug. 1995), pp. 227–233. ISSN: 15222594. DOI: 10.1002/mrm.1910340214.

[87] Pierre Gillis et al. "On T2-shortening by strongly magnetized spheres: A partial refocusing model". In: *Magnetic Resonance in Medicine* 47.2 (Feb. 2002), pp. 257–263. ISSN: 0740-3194. DOI: 10.1002/mrm.10059.

[88] O. M. Girard et al. "Optimization of iron oxide nanoparticle detection using ultrashort echo time pulse sequences: Comparison of T1, T2*, and synergistic T1 - T2* contrast mechanisms". In: *Magnetic Resonance in Medicine* 65.6 (June 2011), pp. 1649–1660. ISSN: 07403194. DOI: 10.1002/mrm.22755.

[89] Liya Wang et al. "Ultrashort echo time (UTE) imaging of receptor targeted magnetic iron oxide nanoparticles in mouse tumor models." In: *Journal of magnetic resonance imaging : JMRI* 40.5 (2014), pp. 1071–81. ISSN: 1522-2586. DOI: 10.1002/jmri.24453.

[90] Stavros. Kromidas. *Handbuch Validierung in der Analytik*. Wiley-VCH, 2000. ISBN: 9783527329380. DOI: 10.1002/9783527624911.

[91] Raymond P. W. Scott. "Chromatographic Detectors: Design, function, and operation". In: *Journal of Chromatography A* 761.1-2 (Feb. 1997), pp. 343–344. ISSN: 00219673. DOI: 10.1016/s0021-9673(97)90303-4.

[92] "International Conference on Harmonization (ICH), Validation of Analytical Procedures: Text and Methodology, Q2(R1), IFPMA, Geneva". In: (2005).

[93] ISO 5725-1. "Accuracy (trueness and precision) of measurement methods and results - Part 1: General principles and definitions". In: (1994).

[94] P. Karp et al. "Unidirectional magnetic gradiometers". In: *Journal of Applied Physics* 51.3 (1980), pp. 1267–1272. ISSN: 00218979. DOI: 10.1063/1.327819.

[95] P. B. Roemer et al. "The NMR phased array". In: *Magnetic Resonance in Medicine* 16.2 (Nov. 1990), pp. 192–225. ISSN: 15222594. DOI: 10.1002/mrm.1910160203.

[96] James E. Zimmerman. "SQUID instruments and shielding for low-level magnetic measurements". In: *Journal of Applied Physics* 48.2 (1977), pp. 702–710. ISSN: 00218979. DOI: 10.1063/1.323659.

[97] Volkmar Schulz et al. “A Field Cancellation Signal Extraction Method for Magnetic Particle Imaging”. In: *IEEE Transactions on Magnetics* 51.2 (Feb. 2015), pp. 1–4. ISSN: 0018-9464. DOI: 10.1109/TMAG.2014.2325852.

[98] S Biederer et al. “Magnetization response spectroscopy of superparamagnetic nanoparticles for magnetic particle imaging”. In: *Journal of Physics D: Applied Physics* 42.20 (2009). ISSN: 0022-3727. DOI: 10.1088/0022-3727/42/20/205007.

[99] Norbert Löwa et al. “Magnetic nanoparticles in different biological environments analyzed by magnetic particle spectroscopy”. In: *Journal of Magnetism and Magnetic Materials* 427.4 Pt 1 (Apr. 2017), pp. 133–138. ISSN: 03048853. DOI: 10.1016/j.jmmm.2016.10.096.

[100] S. Meiboom et al. “Modified spin-echo method for measuring nuclear relaxation times”. In: *Review of Scientific Instruments* 29.8 (1958), pp. 688–691. ISSN: 00346748. DOI: 10.1063/1.1716296. arXiv: arXiv:1011.1669v3.

[101] Peter Reimer et al. “Ferucarbotran (Resovist): a new clinically approved RES-specific contrast agent for contrast-enhanced MRI of the liver: properties, clinical development, and applications”. In: *European Radiology* 13.6 (June 2003), pp. 1266–1276. ISSN: 0938-7994. DOI: 10.1007/s00330-002-1721-7.

[102] James Wells et al. “Standardisation of magnetic nanoparticles in liquid suspension”. In: *Journal of Physics D: Applied Physics* 50.38 (Sept. 2017). ISSN: 0022-3727. DOI: 10.1088/1361-6463/aa7fa5.

[103] Ping Wang et al. “Magnetic particle imaging of islet transplantation in the liver and under the kidney capsule in mouse models”. In: *Quantitative Imaging in Medicine and Surgery* 8.2 (2018), pp. 114–122. ISSN: 22234292. DOI: 10.21037/qims.2018.02.06.

[104] Norbert Löwa et al. “Concentration Dependent MPI Tracer Performance”. In: *International Journal on Magnetic Particle Imaging* 2.1 (2016), p. 5. ISSN: 2365-9033. DOI: 10.18416/ijmpi.2016.1601001.

[105] Martin Rohrer et al. “Comparison of magnetic properties of MRI contrast media solutions at different magnetic field strengths”. In: *Investigative Radiology* 40.11 (2005), pp. 715–724. ISSN: 00209996. DOI: 10.1097/01.rli.0000184756.66360.d3. arXiv: arXiv:1011.1669v3.

[106] Sushanta Kumar Mishra et al. “Increased transverse relaxivity in ultrasmall superparamagnetic iron oxide nanoparticles used as MRI contrast agent for biomedical imaging”. In: *Contrast Media and Molecular Imaging* 11.5 (2016), pp. 350–361. ISSN: 15554317. DOI: 10.1002/cmmi.1698.

[107] Andrea Lassenberger et al. “Individually stabilized, superparamagnetic nanoparticles with controlled shell and size leading to exceptional stealth properties and high relaxivities”. In: *ACS Applied Materials and Interfaces* 9.4 (2017), pp. 3343–3353. ISSN: 19448252. DOI: 10.1021/acsami.6b12932.

[108] Kai-Felix Braun et al. “Quantitative measurement of the magnetic moment of an individual magnetic nanoparticle by magnetic force microscopy”. In: *Applied Physics Letters* 98.18 (Feb. 2010). ISSN: 0003-6951. DOI: 10.1063/1.3586776. arXiv: 1002.3739.

[109] Rüdiger Lawaczeck et al. “Magnetic Iron Oxide Particles Coated with Carboxydextran for Parenteral Administration and Liver Contrasting”. In: *Acta Radiologica* 38.4 (July 1997), pp. 584–597. ISSN: 0284-1851. DOI: 10.1080/02841859709174391.

[110] Helena Gavilán et al. “Colloidal Flower-Shaped Iron Oxide Nanoparticles: Synthesis Strategies and Coatings”. In: *Particle and Particle Systems Characterization* 34.7 (2017), pp. 1–12. ISSN: 15214117. DOI: 10.1002/ppsc.201700094.

[111] D.I Hoult et al. “The signal-to-noise ratio of the nuclear magnetic resonance experiment”. In: *Journal of Magnetic Resonance (1969)* 24.1 (1976), pp. 71–85. ISSN: 00222364. DOI: 10.1016/0022-2364(76)90233-X.

[112] Patrick W Goodwill et al. *An x-space magnetic particle imaging scanner*. Mar. 2012. DOI: 10.1063/1.3694534.

[113] Kolja Them et al. “Sensitivity Enhancement in Magnetic Particle Imaging by Background Subtraction”. In: *IEEE Transactions on Medical Imaging* 35.3 (Mar. 2016), pp. 893–900. ISSN: 0278-0062. DOI: 10.1109/TMI.2015.2501462.

[114] Jochen Franke et al. “System Characterization of a Highly Integrated Preclinical Hybrid MPI-MRI Scanner”. In: *IEEE Transactions on Medical Imaging* 35.9 (2016), pp. 1993–2004. ISSN: 1558254X. DOI: 10.1109/TMI.2016.2542041.

[115] Anselm von Gladiss et al. “Hybrid system calibration for multidimensional magnetic particle imaging”. In: *Physics in Medicine and Biology* 62.9 (2017), pp. 3392–3406. ISSN: 0031-9155. DOI: 10.1088/1361-6560/aa5340.

[116] Marcel Straub et al. “Joint reconstruction of tracer distribution and background in magnetic particle imaging”. In: *IEEE Transactions on Medical Imaging* 37.5 (2018), pp. 1192–1203. ISSN: 1558254X. DOI: 10.1109/TMI.2017.2777878.

[117] Tobias Knopp et al. “Correction of linear system drifts in magnetic particle imaging”. In: *Physics in Medicine and Biology* (May 2019). ISSN: 0031-9155. DOI: 10.1088/1361-6560/ab2480.

[118] S Biederer. “Magnet-Partikel-Spektrometer”. PhD thesis. Universität zu Lübeck, 2012. ISBN: 9783834824066.

[119] Norbert Löwa. “Entwicklung neuer Kopplungsverfahren zur Charakterisierung von magnetischen Nanopartikeln basierend auf der Messung der nichtlinearen magnetischen Wechselfeld-Suszeptibilität”. PhD thesis. Technische Universität Berlin, 2017.

[120] Christophe Leys et al. “Detecting outliers: Do not use standard deviation around the mean, use absolute deviation around the median”. In: *Journal of Experimental Social Psychology* 49.4 (July 2013), pp. 764–766. ISSN: 00221031. DOI: 10.1016/j.jesp.2013.03.013.

[121] Tobias Kluth et al. “Enhanced reconstruction in magnetic particle imaging by whitening and randomized SVD approximation”. In: *Physics in Medicine & Biology* 64.12 (June 2019). ISSN: 1361-6560. DOI: 10.1088/1361-6560/ab1a4f. arXiv: 1902.01199.

[122] Patryk Szwargulski et al. “Influence of the Receive Channel Number on the Spatial Resolution in Magnetic Particle Imaging”. In: *International Journal on Magnetic Particle Imaging* 3.1 (2017). ISSN: 2365-9033.

[123] T Knopp et al. “Magnetic particle imaging: from proof of principle to preclinical applications”. In: *Physics in Medicine & Biology* (2017). ISSN: 0031-9155. DOI: 10.1088/1361-6560/aa6c99.

[124] J Weizenecker et al. “A simulation study on the resolution and sensitivity of magnetic particle imaging.” In: *Physics in medicine and biology* 52.21 (2007), pp. 6363–6374. ISSN: 0031-9155. DOI: 10.1088/0031-9155/52/21/001.

[125] Tobias Knopp et al. *Magnetic Particle Imaging*. Berlin, Heidelberg: Springer Berlin Heidelberg, 2012. ISBN: 978-3-642-04198-3. DOI: 10.1007/978-3-642-04199-0.

[126] A Weber et al. “Artifact free reconstruction with the system matrix approach by overscanning the field-free-point trajectory in magnetic particle imaging”. In: *Physics in Medicine and Biology* 61.2 (2016), pp. 475–487. ISSN: 0031-9155. DOI: 10.1088/0031-9155/61/2/475.

[127] James Wells et al. “Characterizing a Preclinical Magnetic Particle Imaging System With Separate Pickup Coil”. In: *IEEE Transactions on Magnetics* 53.11 (Nov. 2017), pp. 1–5. ISSN: 00189464. DOI: 10.1109/TMAG.2017.2708419.

[128] Lucas Wöckel et al. “Long-term stable measurement phantoms for magnetic particle imaging”. In: *Journal of Magnetism and Magnetic Materials* 471 (Feb. 2019), pp. 1–7. ISSN: 03048853. DOI: 10.1016/j.jmmm.2018.09.012.

[129] Olaf Kosch et al. “Evaluation of a separate-receive coil by magnetic particle imaging of a solid phantom”. In: *Journal of Magnetism and Magnetic Materials* 471 (Feb. 2019), pp. 444–449. ISSN: 03048853. DOI: 10.1016/j.jmmm.2018.09.114.

[130] Linda Kaufman. “Maximum likelihood, least squares, and penalized least squares for PET”. In: *IEEE Transactions on Medical Imaging* 12.2 (June 1993), pp. 200–214. ISSN: 02780062. DOI: 10.1109/42.232249.

[131] Per Christian Hansen. “REGULARIZATION TOOLS: A Matlab package for analysis and solution of discrete ill-posed problems”. In: *Numerical Algorithms* 6.1 (Mar. 1994), pp. 1–35. ISSN: 10171398. DOI: 10.1007/BF02149761.

[132] Richard C. Aster et al. *Parameter Estimation and Inverse Problems*. Vol. 90. International Geophysics. Elsevier, 2013. ISBN: 9780123850485. DOI: 10.1016/C2009-0-61134-X.

[133] A N Tikhonov. "Solution of Incorrectly Formulated Problems and the Regularisation Method". In: *Soviet Mathematics Doklady* 4.4 (Jan. 1963), pp. 1035–1038.

[134] Per Christian Hansen et al. "The Use of the L-Curve in the Regularization of Discrete Ill-Posed Problems". In: *SIAM Journal on Scientific Computing* 14.6 (Nov. 1993), pp. 1487–1503. ISSN: 1064-8275. DOI: 10.1137/0914086.

[135] Dorota Krawczyk-Stańdo et al. "Regularization parameter selection in discrete ill-posed problems - The use of the U-curve". In: *International Journal of Applied Mathematics and Computer Science* 17.2 (June 2007), pp. 157–164. ISSN: 1641876X. DOI: 10.2478/v10006-007-0014-3.

[136] Per Christian Hansen. *Rank-Deficient and Discrete Ill-Posed Problems*. Society for Industrial and Applied Mathematics, Jan. 1998. ISBN: 978-0-89871-403-6. DOI: 10.1137/1.9780898719697.

[137] J. S. Arora et al. "Methods for optimization of nonlinear problems with discrete variables: A review". In: *Structural Optimization* 8.2-3 (Oct. 1994), pp. 69–85. ISSN: 0934-4373. DOI: 10.1007/BF01743302.

[138] M. Liebl et al. "Quantitative imaging of magnetic nanoparticles by magnetorelaxometry with multiple excitation coils". In: *Physics in Medicine and Biology* 59.21 (2014), pp. 6607–6620. ISSN: 13616560. DOI: 10.1088/0031-9155/59/21/6607.

[139] Simone Colombo et al. "Imaging Magnetic Nanoparticle Distributions by Atomic Magnetometry-based Susceptometry". In: *IEEE Transactions on Medical Imaging* (2019), pp. 1–1. ISSN: 0278-0062. DOI: 10.1109/TMI.2019.2937670.

[140] Zachary R Stephen et al. "Magnetite Nanoparticles for Medical MR Imaging Mater". In: *Materials Today* 14.11 (2012), pp. 330–338. DOI: 10.1016/S1369-7021(11)70163-8.Magnetite.

[141] Ali M. Rad et al. "Quantification of superparamagnetic iron oxide (SPIO)-labeled cells using MRI". In: *Journal of Magnetic Resonance Imaging* 26.2 (Aug. 2007), pp. 366–374. ISSN: 10531807. DOI: 10.1002/jmri.20978.

[142] Paul A. Bottomley et al. "A review of normal tissue hydrogen NMR relaxation times and relaxation mechanisms from 1-100 MHz: Dependence on tissue type, NMR frequency, temperature, species, excision, and age". In: *Medical Physics* 11.4 (July 1984), pp. 425–448. ISSN: 00942405. DOI: 10.1118/1.595535.

[143] Jason M. Zhao et al. "Oxygenation and hematocrit dependence of transverse relaxation rates of blood at 3T". In: *Magnetic Resonance in Medicine* 58.3 (2007), pp. 592–597. ISSN: 07403194. DOI: 10.1002/mrm.21342.

[144] Wendy Oakden et al. "Effects of diffusion on high-resolution quantitative T2 MRI". In: *NMR in Biomedicine* 27.6 (June 2014), pp. 672–680. ISSN: 10991492. DOI: 10.1002/nbm.3104.

[145] Susanne Siemonsen et al. "Age-Dependent Normal Values of T2* and T2' in Brain Parenchyma". In: *American Journal of Neuroradiology* 29.5 (May 2008), pp. 950–955. ISSN: 0195-6108. DOI: 10.3174/ajnr.A0951.

[146] Timothy M. Shepherd et al. "New rapid, accurate T 2 quantification detects pathology in normal-appearing brain regions of relapsing-remitting MS patients". In: *NeuroImage: Clinical* 14 (Jan. 2017), pp. 363–370. ISSN: 22131582. DOI: 10.1016/j.nicl.2017.01.029.

[147] Wen Hong et al. "Imaging and quantification of iron-oxide nanoparticles (IONP) using MP-RAGE and UTE based sequences". In: *Magnetic Resonance in Medicine* 78.1 (July 2017), pp. 226–232. ISSN: 07403194. DOI: 10.1002/mrm.26371.

[148] James Wells et al. "Temperature dependence in magnetic particle imaging". In: *AIP Advances* 8.5 (May 2018). ISSN: 2158-3226. DOI: 10.1063/1.5004506.

[149] Yong Eun Chung et al. "Quantification of superparamagnetic iron oxide-mediated signal intensity change in patients with liver cirrhosis using T2 and T2* mapping: A preliminary report". In: *Journal of Magnetic Resonance Imaging* 31.6 (2010), pp. 1379–1386. ISSN: 15222586. DOI: 10.1002/jmri.22184.

[150] Eldin Wee Chuan Lim et al. "Agglomeration of magnetic nanoparticles." In: *The Journal of chemical physics* 136.12 (Mar. 2012). ISSN: 1089-7690. DOI: 10.1063/1.3697865.

[151] Alain Roch et al. "Superparamagnetic colloid suspensions: Water magnetic relaxation and clustering". In: *Journal of Magnetism and Magnetic Materials* 293.1 (May 2005), pp. 532–539. ISSN: 03048853. DOI: 10.1016/j.jmmm.2005.01.070.

[152] Quoc Lam Vuong et al. "Monte Carlo simulation and theory of proton NMR transverse relaxation induced by aggregation of magnetic particles used as MRI contrast agents". In: *Journal of Magnetic Resonance* 212.1 (Sept. 2011), pp. 139–148. ISSN: 10907807. DOI: 10.1016/j.jmr.2011.06.024.

[153] P. Keselman et al. "Tracking short-term biodistribution and long-term clearance of SPIO tracers in magnetic particle imaging". In: *Phys. Med. Biol.* (2017). ISSN: 13616560. DOI: 10.1088/1361-6560/aa5f48.

[154] Elaine Y. Yu et al. "Magnetic Particle Imaging: A Novel in Vivo Imaging Platform for Cancer Detection". In: *Nano Letters* 17.3 (2017), pp. 1648–1654. ISSN: 15306992. DOI: 10.1021/acs.nanolett.6b04865.

[155] Hannes Dahnke et al. "Susceptibility gradient mapping (SGM): A new postprocessing method for positive contrast generation applied to superparamagnetic iron oxide particle (SPIO)-labeled cells". In: *Magnetic Resonance in Medicine* 60.3 (2008), pp. 595–603. ISSN: 07403194. DOI: 10.1002/mrm.21478.

[156] Dominique Finas et al. “Sentinel lymphnode detection in breast cancer by magnetic particle imaging using superparamagnetic nanoparticles”. In: *Magnetic Nanoparticles*. WORLD SCIENTIFIC, Aug. 2010, pp. 205–210. ISBN: 978-981-4324-67-0. DOI: 10.1142/9789814324687_0029.

[157] Wolfram C. Poller et al. “Magnetic particle spectroscopy reveals dynamic changes in the magnetic behavior of very small superparamagnetic iron oxide nanoparticles during cellular uptake and enables determination of cell-labeling efficacy”. In: *Journal of Biomedical Nanotechnology* 12.2 (2016), pp. 337–346. ISSN: 15507041. DOI: 10.1166/jbn.2016.2204.

[158] Wolfram C. Poller et al. “Very small superparamagnetic iron oxide nanoparticles: Long-term fate and metabolic processing in atherosclerotic mice”. In: *Nanomedicine: Nanotechnology, Biology, and Medicine* 14.8 (Nov. 2018), pp. 2575–2586. ISSN: 15499642. DOI: 10.1016/j.nano.2018.07.013.

[159] D. E. Markov et al. “Human erythrocytes as nanoparticle carriers for magnetic particle imaging”. In: *Physics in Medicine and Biology* 55.21 (Nov. 2010), pp. 6461–6473. ISSN: 0031-9155. DOI: 10.1088/0031-9155/55/21/008.

[160] Hamed Arami et al. “Intracellular performance of tailored nanoparticle tracers in magnetic particle imaging”. In: *Journal of Applied Physics* 115.17 (2014), pp. 3–5. ISSN: 10897550. DOI: 10.1063/1.4867756.

[161] Antje Ludwig et al. “Rapid binding of electrostatically stabilized iron oxide nanoparticles to THP-1 monocytic cells via interaction with glycosaminoglycans”. In: *Basic Research in Cardiology* 108.2 (Mar. 2013), p. 328. ISSN: 0300-8428. DOI: 10.1007/s00395-013-0328-2.

[162] Stefan G. Ruehm et al. “Magnetic Resonance Imaging of Atherosclerotic Plaque With Ultrasmall Superparamagnetic Particles of Iron Oxide in Hyperlipidemic Rabbits”. In: *Circulation* 103.3 (Jan. 2001), pp. 415–422. ISSN: 0009-7322. DOI: 10.1161/01.CIR.103.3.415.

[163] M.E. Kooi et al. “Accumulation of Ultrasmall Superparamagnetic Particles of Iron Oxide in Human Atherosclerotic Plaques Can Be Detected by In Vivo Magnetic Resonance Imaging”. In: *Circulation* 107.19 (May 2003), pp. 2453–2458. ISSN: 0009-7322. DOI: 10.1161/01.CIR.0000068315.98705.CC.

[164] Marcus R. Makowski et al. “Noninvasive assessment of atherosclerotic plaque progression in ApoE -/- mice using susceptibility gradient mapping”. In: *Circulation: Cardiovascular Imaging* 4.3 (May 2011), pp. 295–303. ISSN: 19419651. DOI: 10.1161/CIRCIMAGING.110.957209.

[165] Constantin Scharlach et al. “Synthesis of acid-stabilized iron oxide nanoparticles and comparison for targeting atherosclerotic plaques: Evaluation by MRI, quantitative MPS, and TEM alternative to ambiguous Prussian blue iron staining”. In: *Nanomedicine: Nanotechnology, Biology and Medicine* 11.5 (July 2015), pp. 1085–1095. ISSN: 15499634. DOI: 10.1016/j.nano.2015.01.002.

[166] Wolfram C. Poller et al. “Uptake of citrate-coated iron oxide nanoparticles into atherosclerotic lesions in mice occurs via accelerated transcytosis through plaque endothelial cells”. In: *Nano Research* 9.11 (Nov. 2016), pp. 3437–3452. ISSN: 19980000. DOI: 10.1007/s12274-016-1220-9.

[167] C L Lendon et al. “Atherosclerotic plaque caps are locally weakened when macrophages density is increased.” In: *Atherosclerosis* 87.1 (Mar. 1991), pp. 87–90. ISSN: 0021-9150. DOI: 10.1016/0021-9150(91)90235-u.

[168] Peter Libby et al. “Molecular determinants of atherosclerotic plaque vulnerability”. In: *Annals of the New York Academy of Sciences*. Vol. 811. 1 Atheroscleros. John Wiley & Sons, Ltd (10.1111), Apr. 1997, pp. 134–145. DOI: 10.1111/j.1749-6632.1997.tb51996.x.

[169] Wim Martinet et al. “Molecular and cellular mechanisms of macrophage survival in atherosclerosis”. In: *Basic Research in Cardiology* 107.6 (Nov. 2012), p. 297. ISSN: 0300-8428. DOI: 10.1007/s00395-012-0297-x.

[170] Anna Lesniak et al. “Effects of the presence or absence of a protein corona on silica nanoparticle uptake and impact on cells”. In: *ACS Nano* 6.7 (July 2012), pp. 5845–5857. ISSN: 19360851. DOI: 10.1021/nn300223w.

[171] Christine Gräfe et al. “Intentional formation of a protein corona on nanoparticles: Serum concentration affects protein corona mass, surface charge, and nanoparticle-cell interaction”. In: *International Journal of Biochemistry and Cell Biology* 75 (2016), pp. 196–202. ISSN: 18785875. DOI: 10.1016/j.biocel.2015.11.005.

[172] Rebecca Kuhlpeter et al. “R2 and R2* Mapping for Sensing Cell-bound Superparamagnetic Nanoparticles: In Vitro and Murine in Vivo Testing”. In: *Radiology* 245.2 (Nov. 2007), pp. 449–457. ISSN: 0033-8419. DOI: 10.1148/radiol.2451061345.

[173] O. M. Girard et al. “Toward absolute quantification of iron oxide nanoparticles as well as cell internalized fraction using multiparametric MRI”. In: *Contrast Media and Molecular Imaging* 7.4 (July 2012), pp. 411–417. ISSN: 15554309. DOI: 10.1002/cmmi.1467.

[174] Heather Herd Gustafson et al. “Nanoparticle uptake: The phagocyte problem”. In: *Nano Today* 10.4 (Aug. 2015), pp. 487–510. ISSN: 17480132. DOI: 10.1016/j.nantod.2015.06.006.

[175] Swetha Inturi et al. “Modulatory Role of Surface Coating of Superparamagnetic Iron Oxide Nanoworms in Complement Opsonization and Leukocyte Uptake”. In: *ACS Nano* 9.11 (Nov. 2015), pp. 10758–10768. ISSN: 1936-0851. DOI: 10.1021/acsnano.5b05061.

[176] Hendrik Paysen et al. “Towards quantitative magnetic particle imaging: A comparison with magnetic particle spectroscopy”. In: *AIP Advances* 8.5 (May 2018). ISSN: 21583226. DOI: 10.1063/1.5006391.

[177] Hendrik Paysen et al. “Improved sensitivity and limit-of-detection using a receive-only coil in magnetic particle imaging”. In: *Physics in Medicine & Biology* 63.13 (July 2018). ISSN: 1361-6560. DOI: 10.1088/1361-6560/aacb87.

[178] Hendrik Paysen et al. “Imaging and quantification of magnetic nanoparticles: Comparison of magnetic resonance imaging and magnetic particle imaging”. In: *Journal of Magnetism and Magnetic Materials* 475 (Apr. 2019), pp. 382–388. ISSN: 03048853. DOI: 10.1016/j.jmmm.2018.10.082.

[179] Hendrik Paysen et al. “Cellular uptake of magnetic nanoparticles imaged and quantified by magnetic particle imaging”. In: *Scientific Reports* 10.1 (Dec. 2020). ISSN: 2045-2322. DOI: 10.1038/s41598-020-58853-3.

[180] Norbert Löwa et al. “3D-printing of novel magnetic composites based on magnetic nanoparticles and photopolymers”. In: *Journal of Magnetism and Magnetic Materials* 469 (Jan. 2019), pp. 456–460. ISSN: 03048853. DOI: 10.1016/j.jmmm.2018.08.073.